P 2mit

NASA TECHNICAL NOTE

NASA TN D-7342

NASA TN D-7342

APERTURE EXCITED DIELECTRIC ANTENNAS

by

W. F. Croswell and J. S. Chatterjee
Langley Research Center
Hampton, Va. 23665

and

V. B. Mason and C-T. Tai
Radiation Laboratory
The University of Michigan
Ann Arbor, Mich.

NATIONAL AERONAUTICS AND SPACE ADMINISTRATION • WASHINGTON, D. C. • MAY 1974

1. Report No. NASA TN D-7342	2. Government Accession No.	3. Recipient's Catalog No.
4. Title and Subtitle APERTURE EXCITED DIELECTRIC ANTENNAS		5. Report Date May 1974 6. Performing Organization Code
7. Author(s) W. F. Croswell and J. S. Chatterjee (Langley Research Center); V. B. Mason and C-T. Tai (Radiation Laboratory, The University of Michigan)		8. Performing Organization Report No. L-8920
9. Performing Organization Name and Address NASA Langley Research Center Hampton, Va. 23665		10. Work Unit No. 636-18-71-02 11. Contract or Grant No.
12. Sponsoring Agency Name and Address National Aeronautics and Space Administration Washington, D.C. 20546		13. Type of Report and Period Covered Technical Note 14. Sponsoring Agency Code

15. Supplementary Notes

J. S. Chatterjee is an NRC-NASA resident research associate on leave from Jadavpur University, Calcutta, India.

16. Abstract

The results of a comprehensive experimental and theoretical study of the effect of placing dielectric objects over the aperture of waveguide antennas are presented. Experimental measurements of the radiation patterns, gain, impedance, near-field amplitude, and pattern and impedance coupling between pairs of antennas are given for various Plexiglas shapes, including the sphere and the cube, excited by rectangular, circular, and square waveguide feed apertures. The waveguide excitation of a dielectric sphere is modeled using the Huygens' source, and expressions for the resulting electric fields, directivity, and efficiency are derived. Calculations using this model show good overall agreement with experimental patterns and directivity measurements. The waveguide under an infinite dielectric slab is used as an impedance model. Calculations using this model agree qualitatively with the measured impedance data.

It is concluded that dielectric loaded antennas such as the waveguide excited sphere, cube, or sphere-cylinder can produce directivities in excess of that obtained by a uniformly illuminated aperture of the same cross section, particularly for dielectric objects with dimensions of 2 wavelengths or less. It is also shown that for certain configurations coupling between two antennas of this type is less than that for the same antennas without dielectric loading.

17. Key Words (Suggested by Author(s))	18. Distribution Statement		
Antennas Dielectric loaded antennas Feeds for multiple beam antennas	Unclassified – Unlimited STAR Category 07		
19. Security Classif. (of this report) Unclassified	20. Security Classif. (of this page) Unclassified	21. No. of Pages 126	22. Price* $4.75

*For sale by the National Technical Information Service, Springfield, Virginia 22151

CONTENTS

	Page
SUMMARY	1
INTRODUCTION	1
SYMBOLS	2
ABBREVIATIONS	5
EXPERIMENTAL MEASUREMENTS	6
Radiation Patterns for Plexiglas Spheres and Cubes	6
Circular waveguide feed	6
Slot feed	6
Rectangular and square waveguide feeds	7
Influence of Feed Displacement	7
Effects of Object Dimensions on Radiation Patterns	7
Beamwidth and Gain	8
Impedance	8
Comparison with available theory	9
Matching devices	10
Near-Field Measurements	10
Coupling	11
Pattern coupling	11
Impedance coupling	12
ELECTROMAGNETIC THEORY OF A DIELECTRIC SPHERE EXCITED BY A HUYGENS' SOURCE	12
Huygens' Source Model	12
Dyadic Green's Functions Pertaining to the Dielectric Sphere	13
Electric source in region I, observation point in region I	19
Electric source in region I, observation point in region II	20
Electric source in region II, observation point in region I	22
Electric source in region II, observation point in region II	22
Magnetic source in region I, observation point in region I	24
Magnetic source in region I, observation point in region II	24
Magnetic source in region II, observation point in region I	24
Magnetic source in region II, observation point in region II	25

Page

Electric Fields Due to a Huygens' Source in the Presence of a Dielectric Sphere 25
Source in region I, observation point in region I 26
Source in region I, observation point in region II 26
Source in region II, observation point in region I 27
Source in region II, observation point in region II 27
Properties of a Huygens' Source in the Presence of a Dielectric Sphere 31
Radiated power 31
Radiation resistance 32
Directivity 33
Efficiency 35

NUMERICAL RESULTS 38

DISCUSSION 39

CONCLUDING REMARKS 40

APPENDIX – COMPUTER PROGRAM 42

REFERENCES 49

TABLES 50

FIGURES 52

APERTURE EXCITED DIELECTRIC ANTENNAS

By W. F. Croswell, J. S. Chatterjee,* V. B. Mason,** and C-T. Tai**
Langley Research Center

SUMMARY

The results of a comprehensive experimental and theoretical study of the effect of placing dielectric objects over the aperture of waveguide antennas are presented. Experimental measurements of the radiation patterns, gain, impedance, near-field amplitude, and pattern and impedance coupling between pairs of antennas are given for various Plexiglas shapes, including the sphere and the cube, excited by rectangular, circular, and square waveguide feed apertures. The waveguide excitation of a dielectric sphere is modeled using the Huygens' source, and expressions for the resulting electric fields, directivity, and efficiency are derived. Calculations using this model show good overall agreement with experimental patterns and directivity measurements. The waveguide under an infinite dielectric slab is used as an impedance model. Calculations using this model agree qualitatively with the measured impedance data.

It is concluded that dielectric loaded antennas such as the waveguide excited sphere, cube, or sphere-cylinder can produce directivities in excess of that obtained by a uniformly illuminated aperture of the same cross section, particularly for dielectric objects with dimensions of 2 wavelengths or less. It is also shown that for certain configurations coupling between two antennas of this type is less than that for the same antennas without dielectric loading.

INTRODUCTION

Many of the future communications or navigation satellite systems will require multiple or adaptive beam antennas with shaped or controlled beam coverages, depending upon the application. Common approaches to solving this problem include the placement of multiple feeds in the focal plane of a direct-fed parabolic reflector, or to assemble the same feeds to illuminate an offset parabolic reflector. In the case of the direct-fed parabolic reflector the size of the multiple beam cluster will cause blockage, and for both the direct-fed and offset-fed parabolic reflectors the spillover and side lobe level of each

---

*NRC-NASA Resident Research Associate, on leave from Jadavpur University, Calcutta, India.
**Radiation Laboratory, The University of Michigan.

beam is dependent upon the amount of interelement coupling and how closely packed the feed elements can be placed. Also important for this type of design are minimum spillover consistent with achieving high aperture efficiency, which is again related to the size and packing capability of the multiple beam feed elements. As a result, there is a requirement for a feed element that exhibits low blockage, low mutual coupling between adjacent elements, and that also produces the maximum directivity for a given aperture size. The work described in this report was motivated by this requirement.

It has been found experimentally that an antenna constructed by placing small dielectric objects such as the sphere or cube over a waveguide aperture exhibit radiation and coupling properties desirable for feed antennas. In this report many of these measurements are presented. Subsequently the waveguide aperture excitation is modeled using a single Huygens' source, and a rigorous electromagnetic analysis is presented for the dielectric sphere. These theoretical results are found to agree closely with the measurements. Finally, the results of the complete study are discussed and concluding remarks about the aperture excited dielectric (AED) antenna and its properties are presented.

SYMBOLS

a	sphere radius
a_w	radius of circular waveguide
b	normalized susceptance
b_1	distance of Huygens' source to center of coordinates
C_e	electric current moment
C_m	magnetic current moment
D	sphere diameter, $2a$
d	thickness of dielectric slab
D_0	directivity
E-plane	pattern measurement plane which contains electric-field vector
$\bar{E}(\bar{R})$	electric field at position vector $\bar{R}$

$\bar{E}$	electric field
f	frequency
g	normalized conductance
$\bar{\bar{G}}_0(\bar{R}\,\vert\,\bar{R}')$	free-space dyadic Green's function
$\bar{\bar{G}}_3^{(nm)}(\bar{R}\,\vert\,\bar{R}')$	dyadic Green's function of third kind
$\bar{\bar{G}}_4^{(nm)}(\bar{R}\,\vert\,\bar{R}')$	dyadic Green's function of fourth kind
H-plane	pattern measurement plane which contains magnetic-field vector
$\bar{H}(\bar{R})$	magnetic field at position vector $\bar{R}$
$\bar{H}$	magnetic field
$h_n(kR)$	spherical Hankel function of first kind
$\bar{\bar{I}}$	unit dyad
I_0	constant current magnitude
$\bar{J}(\bar{R}')$	electric current density
$J_1(x)$	cylindrical Bessel function of first kind
$\bar{J}_m(\bar{R}')$	magnetic current density
$j_n(kR)$	spherical Bessel function of order n
k_0	free-space wave number, $2\pi/\lambda$
k_n	wave number of medium n, $\omega\sqrt{\mu_n \epsilon_n}$
ℓ	length of electric current segment
$\bar{M}$	spherical vector wave functions

$\bar{N}$	spherical vector wave function
N	index of refraction, $\sqrt{\epsilon_n}$
$\hat{n}$	unit normal directed away from body surface
P_D	dissipated power
$P_n^m(\cos\theta)$	associated Legendre function of degree m and order n
$\bar{R}$	vector from coordinate origin to observation point
$\bar{R}'$	vector from coordinate origin to source point
R_r	radiation resistance
$\tan\delta$	loss tangent
TE_{01}	E mode in a rectangular or square waveguide
TE_{11}	E mode in a circular waveguide
W	total radiated power
x'_{11}	first root of $\frac{d}{dx}\left[J_1(x'_{11})\right]$
x, y, z	coordinate directions
X, Y, Z	near-field-measurement coordinate directions
$Y_{in} = Y_{TE} + Y_{TM}$	
Y_{TE}	normalized aperture admittance, TE vector potential
Y_{TM}	normalized aperture admittance, TM vector potential
β	normalized radial wave number
Γ	reflection coefficient

$$\delta_0 = \begin{cases} 1 & (m = 0) \\ 0 & (m \neq 0) \end{cases}$$

$\delta(R-R')$ three-dimensional delta function

$$\delta_{n\ell} = \begin{cases} 1 & (n = \ell) \\ 0 & (n \neq \ell) \end{cases}$$

ϵ' real part of dielectric constant

ϵ'' imaginary part of dielectric constant

ϵ_n dielectric constant of medium n

ϵ_r relative dielectric constant

η_n wave impedance of medium n

η_0 free-space wave impedance, $\sqrt{\mu_0/\epsilon_0}$

θ polar angle

λ free-space wavelength

μ_r relative permeability constant

σ conductivity

ϕ azimuthal angle

$\omega = 2\pi f$

ABBREVIATIONS

AED aperture excited dielectric

VSWR voltage standing wave ratio

VTVM vacuum tube volt meter

EXPERIMENTAL MEASUREMENTS

Radiation Patterns for Plexiglas Spheres and Cubes

The aperture excited dielectric (AED) antennas are essentially three-dimensional sources formed by a complex field distribution over the surface of the feed waveguide and the dielectric surface. The radiation patterns therefore are sensitive to the type of feed waveguide; size, shape, and dielectric constant of the dielectric object loading the aperture; operating frequency; and the relative spacing between the feed waveguide and the object. Due to its availability and low cost, all dielectric antennas used in the experimental measurement reported in this paper were constructed from Plexiglas ($\epsilon_r = 2.57$; $\tan \delta = 0.0065$). As shown in later sections using the Huygens' source near a sphere as a model, other dielectrics should also produce directive antenna patterns.

The results of pattern measurements of a variety of waveguide types exciting different dielectric objects are described in this section. The following feeds, detailed dimensions of which are given in figure 1, were used:

(a) Circular waveguide, C-band, excited in the TE_{11} mode
(b) Slot at the end of a rectangular waveguide, X-band, excited in the TE_{01} mode
(c) Rectangular waveguide, X-band, excited in the TE_{01} mode
(d) Square waveguide, X-band, excited from a TE_{01} mode rectangular waveguide with an E-plane taper

A photograph of the circular waveguide feed with Plexiglas objects is shown in figure 2. The radiation patterns were measured using these feeds with Plexiglas cubes and spheres of various dimensions over wide frequency ranges. Only typical patterns illustrating the important features of AED antennas are given in succeeding paragraphs.

Circular waveguide feed.- The open-end circular waveguide shown in figure 1(a) was used to excite a 5.08-cm Plexiglas cube and 5.08-, 7.62-, 10.16-, 12.70-, and 15.24-cm Plexiglas spheres over a frequency range from 5.0 to 6.0 GHz. In each instance the dielectric obstacle was placed tightly against the waveguide aperture, which in the case of dielectric spheres resulted in part of the sphere protruding inside the feed waveguide. Patterns measured at 5.0 GHz for selected dielectric objects are given in figures 3 and 4 for E- and H-plane cuts, respectively; open-end waveguide patterns are given for comparison. It was noted that the cross-polarized pattern was about the same level as that for the open-end waveguide and was therefore not included in the AED radiation pattern plots.

Slot feed.- A thin slot excited by a rectangular waveguide (fig. 1(b)) was used to excite a 5.08-cm Plexiglas cube and Plexiglas spheres 5.08, 7.62, 10.16, 12.70, and 15.24 cm in diameter. A special-shaped Plexiglas object designed to produce a uniform phase front as determined from ray optics was also used. Resulting patterns measured at 10.0 GHz

are given for selected cases in figures 5 and 6. Also included in figure 5 are the patterns of the open slot without a dielectric obstacle. It is noted that the E-plane patterns for the slot AED antenna are poor for the smaller dielectric objects, while the H-plane patterns for dielectric objects of identical size display improved directivity.

Rectangular and square waveguide feeds.- Radiation patterns were measured at 10.0 GHz for the 5.08-cm Plexiglas cube and the 5.08-, 7.62-, 10.16-, and 12.7-cm spheres using the rectangular waveguide and square-horn antenna shown in figures 1(c) and 1(d). Patterns for selected cases are given in figures 7 to 10. As expected, the H-plane patterns for the two feeds were very similar. The E-plane patterns were also similar over the main lobe down to about 10 dB, with the horn patterns exhibiting generally lower side or back lobe levels. Overall, the horn patterns are cleaner; for example, they show little evidence of phase error.

Influence of Feed Displacement

The effect of axial feed displacement on the radiation pattern was studied using the circular waveguide antenna operating at 5.0 GHz with a 12.70-cm Plexiglas sphere. The sphere was displaced a distance 0.635 cm (0.106λ) and 1.27 cm (0.212λ) from the plane of the circular waveguide feed. The resulting radiation patterns are given in figure 11. The primary effect of the displacement was to lower the directivity by broadening the E-plane radiation patterns and by increasing the side lobe energy along the aperture plane. Measurements of the effects of displacement were made using other Plexiglas obstacles, with similar results being obtained.

Effects of Object Dimensions on Radiation Patterns

In general, it was noted that the radiation patterns for spheres and cubes became more directive with increased object size. The effects of the dimensions of the Plexiglas AED antennas on the radiation patterns for other shapes were investigated using Plexiglas rectangular blocks and cylinders with spherical tips. This study was made using the circular waveguide antenna operating at 5.0 GHz. Photographs of the cylindrical and rectangular blocks are given in figure 12. The radiation patterns made using rectangular blocks with a base dimension of 5.08 cm square and with heights varying from 2.54 to 20.32 cm are given in figure 13. The cylindrical AED antennas were constructed by bonding together 5.08-cm cylinders of various lengths with 5.08-cm-diameter hemispheres. Patterns of this AED antenna with cylinder lengths of 0.0, 1.27, and 2.54 cm are given in figure 14. It is observed from figure 13 that there appears to be a single rectangular block configuration (i.e., the cube) that gives good directive radiation patterns with low side lobes. From figure 14 it can be observed that the hemispherically tipped cylinder produces symmetrical radiation patterns with the directivity increasing as a function of length; also, the E-plane and H-plane patterns are nearly identical.

The top surface of a 12.7-cm-diameter sphere was shaped in a manner to produce a uniform path length as explained in figure 15(a); a photograph of the spherical and shaped object is given in figure 15(b). The circle APMONQA represents the surface of the sphere. The dotted line PMONQ represents the portion of the sphere which has been removed to form the surface represented by line PLORQ. The shaping is such that any typical ray path ABC from the source A reaches the front surface SOS' in the same interval of time, that is, in phase. The patterns of the circular waveguide antenna exciting this object in the direct and inverted positions in the waveguide aperture are given in figure 16. Upon comparing the patterns given in this figure with earlier ones using spheres, it is concluded that for these electrically small dielectric obstacles the shape of the outer surface away from the aperture has little effect upon the main lobe structure of the radiation pattern.

For the AED antennas with the dielectric object placed directly upon the aperture of the feed waveguide, all of the shapes produced directive patterns which in most cases had low side lobes. Particularly for the objects where the dielectric dimensions were a free-space wavelength or less (such as the cube, hemispherically tipped cylinder, or small spheres) the E- and H-plane patterns were nearly identical over the main lobe.

Beamwidth and Gain

In order to indicate how the patterns of the AED antennas vary as a function of dielectric dimension, the 3-dB beamwidth is plotted against normalized sphere diameter for the spheres excited by various waveguide feeds, as shown in figure 17. Also shown in this figure is a straight line corresponding to the beamwidth of a uniform circular aperture. It is noted that all spheres exhibit beamwidths narrower than the uniformly excited aperture of the same diameter.

The gain of the circular waveguide antenna of figure 1(a), exciting various Plexiglas objects, was measured at 5.4, 5.5, and 5.6 GHz; the measured values are given in table 1. Any input VSWR for each dielectric object at each frequency was accounted for in the measurements. In figure 18, the gain of several spherical AED antennas is compared with that of an optimum horn having the same cross section. It should be noted that the gain of the AED antenna is at least 3 to 4 dB higher than the corresponding horn.

Impedance

The impedance of the AED antennas in general depends upon the same parameters as the patterns, for example, the type of waveguide feed, size and shape of dielectric object loading the aperture, frequency, etc. However, in previous work (ref. 1), it was determined experimentally that the impedance of a 1 to 2 wavelength slab covering waveguide fed aperture antennas with flanges about the same size as those used in this study was about the

same as that calculated for the waveguide opening onto an infinite slab-covered ground plane. Since there is no available theory to treat the geometry of the AED antenna, and at the present time little hope of attaining one, this model will be used as a first approximation.

Comparison with available theory.- The admittance of a circular waveguide opening onto an infinite ground-plane covered by a semi-infinite dielectric slab has been derived by Bailey and Swift (ref. 1). Consider the geometry given in figure 19. The expressions for the input admittance of the circular waveguide excited by the TE_{11} mode, in this case, are

$$Y_{in} = Y_{TE} + Y_{TM} \tag{1}$$

$$Y_{TE} = \frac{2(x'_{11})^2 \left(\frac{x'_{11}}{k_0 a_w}\right)^2}{\left[(x'_{11})^2 - 1\right]\sqrt{1 - \left(\frac{x'_{11}}{k_0 a_w}\right)^2}} \cdot \int_0^\infty d\beta \, \frac{\beta\sqrt{N^2 - \beta^2}\left[J'_1(k_0 a_w \beta)\right]^2 \left(\frac{\sqrt{1 - \beta^2}}{\sqrt{N^2 - \beta^2}} - j \tan k_0 d \sqrt{N^2 - \beta^2}\right)}{\left[\left(\frac{x'_{11}}{k_0 a_w}\right)^2 - \beta^2\right]^2 \left(1 - j\frac{\sqrt{1 - \beta^2}}{\sqrt{N^2 - \beta^2}} \tan k_0 d \sqrt{N^2 - \beta^2}\right)} \tag{2}$$

$$Y_{TM} = \frac{2N^2}{\left[(x'_{11})^2 - 1\right]\sqrt{1 - \left(\frac{x'_{11}}{k_0 a_w}\right)^2}} \cdot \int_0^\infty d\beta \, \frac{\left[J_1(k_0 a_w \beta)\right]^2 \left(1 - j\frac{N^2\sqrt{1 - \beta^2}}{\sqrt{N^2 - \beta^2}} \tan k_0 d \sqrt{N^2 - \beta^2}\right)}{\beta\sqrt{N^2 - \beta^2}\left(\frac{N^2\sqrt{1 - \beta^2}}{\sqrt{N^2 - \beta^2}} - j \tan k_0 d \sqrt{N^2 - \beta^2}\right)} \tag{3}$$

where a_w is the radius of the circular waveguide, β is the normalized radial wave number, N is the square root of the complex dielectric constant, x'_{11} is the first root of $\frac{d}{dx}\left[J_1(x'_{11})\right]$, d is the thickness of the dielectric slab, and k_0 is the wave number in free space, $2\pi/\lambda$. These impedance expressions were programed, and calculations were performed for the waveguide dimensions given in figure 1(a) with dielectric slabs having the same thickness as the diameter of the sphere or side dimensions of the cube. These calculations were made over a frequency range of 5.0 to 6.0 GHz and compared with admittance measurements for the cube (see fig. 20). It should be noted that the aperture admittance was measured at spot frequencies for the spheres and the data showed a general admittance which was approximately real and lower than the admittance of the cube. Measurements were also made of the input VSWR of the same aperture loaded with spheres; the measurements are compared with the calculations in figure 21. The agreement for all measurements is quite good considering the crudeness of the model. Therefore, the slab model should, for practical purposes, be quite useful for predicting the input admittance of AED antennas, regardless of the shape.

Matching devices.- Because of the smooth behavior of the impedance and VSWR curve measured for AED antennas as a function of frequency, it was believed that plugs made of similar material about a wavelength or so long would be good impedance matching devices. Three plugs with various straight and tapered sections were designed with the dimensions and shapes described in figure 22. The VSWR measured using the plugs inserted in the waveguide are summarized in table 2. Similar results were obtained with larger spheres.

It should be noted that these measurements were made with a coaxial slotted transmission line and hence required a coax to waveguide junction. This junction was optimized for 5.4 to 5.6 GHz. As a result of this matching study, it is believed that AED antennas of other sizes and shapes may also be matched if tapered plugs are used.

Near-Field Measurements

In order to gain some insight into why the AED antennas gave the improved directivity indicated by the pattern and gain measurements, it was decided to measure the near-field properties of several antennas. The simplest method, which measures amplitude only, was devised by Rudge (ref. 2) to measure leakage through small cracks in microwave oven doors. The measurement probe consists of a microwave diode whose pigtail leads are used as a probe dipole. Attached to the dipole is a detection circuit as shown in figure 23. The wings of the dipole are trimmed until, as Rudge demonstrates, the coupling between the antenna to be measured and the dipole is small. In the case of AED antennas the length of the dipole wings was trimmed until the dipole could be inserted into the aperture (and

partially into the waveguide itself) without any change in the VSWR observed at the input terminals of the waveguide. The dipole probe was mounted in a thin glass tube attached to a three-axis precision lathe head, placed some distance below the antenna probe plane. The antenna and probe were then placed inside a box lined with microwave absorber to minimize reflections.

The probe measurements were made in a plane 0.508 cm in front of each antenna being measured. Although complete probe measurements were made in fine increments over the entire aperture of all antennas measured, only principal plane cuts and one measurement down the side of each antenna are presented. The geometry of the measurements is given in figure 24. The near-field amplitude measurements for the different Plexiglas dielectric objects fed by a circular waveguide antenna operating at 6.0 GHz are given in figures 25 to 31. It is readily apparent that near field of significant amplitude extends considerably beyond the physical limits of the dielectric object. The fields in general are tapered and therefore may, in part, account for the low side lobes in the far radiation patterns of the same AED antennas. In the case of the spheres, the measured near fields along the sides of the dielectric objects (denoted as the Y-direction in fig. 24) diminish rapidly as the distance equal to the lower hemisphere is reached. This indicates that for many shapes the field is concentrated primarily in the forward part of the dielectric object, away from the feed aperture. This field concentration indicates there should be reduced coupling between adjacent antennas of this type, as compared with open-end waveguides. This decoupling is confirmed by the results presented in the next section.

Coupling

Pattern coupling.- In order to determine how the patterns of an AED antenna are modified by the presence of other elements, radiation patterns were made using a pair of circular waveguide antennas of the type shown in figure 1(a) where one antenna was excited and the other antenna was terminated in a matched load. The antennas were located side by side with the excitation probes parallel so that either E-plane or H-plane excitation could be obtained by rotating the feed waveguide by 90°.

Pattern measurements were made for pairs of AED antennas, including the 5.08-, 7.62-, 10.16-, and 15.24-cm spheres, as a function of the spacing between elements. Spacings were chosen so that at the minimum distance the waveguide aperture or Plexiglas sphere touched. Measured results are given in figures 32 and 33 for the open-end waveguide and 5.08-cm sphere, respectively. For the open-end waveguide, the E-plane patterns are modified more than the H-plane patterns by the presence of the parasitic element. For the sphere-loaded apertures, however, the H-plane appears to have more pattern coupling than the E-plane. Similar results were obtained for the other dielectric objects.

Impedance coupling.- Impedance coupling measurements were made with two waveguide configurations. First, coupling was measured as a function of spacing with the circular waveguide configuration given in figure 1(a). Similar measurements were made using the same size waveguides mounted in a continuous ground plane 30.48 by 60.96 cm. A photograph of the ground plane and antennas is given in figure 34. Measurements taken of the circular waveguides with flanges are given in figure 35 for the open-end waveguide, the 5.08-cm cube, and the 5.08-cm and 7.62-cm spheres at an operating frequency of 5.8 GHz. It is noted that the E-plane coupling is much lower than the H-plane coupling, which is not the usual case. The coupling measurements of the circular waveguides opening onto a continuous ground plane are given in table 3. These measurements include both E- and H-plane coupling of the two waveguides arranged as shown in figure 35.

From the data in table 3, it is noted that for the continuous ground plane measurements the E-plane coupling is higher than the H-plane coupling for the unloaded case. This is consistent with other ground plane mounted waveguide calculations and measurements. However, with the addition of the dielectric objects, the coupling in the E-plane drops markedly to about the same as the coupling in the H-plane.

ELECTROMAGNETIC THEORY OF A DIELECTRIC SPHERE EXCITED BY A HUYGENS' SOURCE

Huygens' Source Model

In order to understand and optimize the AED antenna, it is desirable to obtain a good theoretical model for the impedance and radiation pattern of the waveguide radiating in the presence of a dielectric obstacle. The solution of this problem for the detailed feed and dielectric geometry is exceedingly difficult. It is well known that the Huygens' source, the superposition of an electric and magnetic current source, can produce a cardioid pattern when radiating into free space. This cardioid pattern closely resembles the radiation pattern of waveguide antennas having small ground planes. Also, the simplest three-dimensional dielectric obstacle for which Green's functions are available is the sphere. Therefore, the Huygens' source model composed of the superposition of electric and magnetic dipole currents near or in a dielectric sphere was chosen as a good theoretical model. A more detailed discussion is contained in reference 3.

Figure 6 shows the geometry under consideration. The source consists of an $\hat{x}$-directed electric dipole, together with a $-\hat{y}$-directed magnetic dipole. The electric and magnetic current moments are denoted by C_e and C_m, respectively. The regions exterior and interior to the sphere are characterized by different constitutive parameters and, therefore, different propagation constants k_1 and k_2, where

$$k_1 = \omega\sqrt{\mu_1 \epsilon_1} \qquad \text{(Region I; } R > a\text{)} \qquad (4)$$

$$k_2 = \omega\sqrt{\mu_2 \epsilon_2} \qquad \text{(Region II; } R < a\text{)} \qquad (5)$$

Here, μ_2 and ϵ_2 are the permeability and permittivity of the sphere, which may be complex. For this application, region I will be free space, and hence $\mu_1 = \mu_0$ and $\epsilon_1 = \epsilon_0$.

With $C_m = \eta_0 C_e$ (where η_0 is the free-space wave impedance) the currents oriented as shown in figure 36, in the absence of the sphere, form a Huygens' source. It radiates a linearly polarized, cardioid pattern with a field maximum in the $-\hat{z}$-direction and a null in the $+\hat{z}$-direction. It is because of this directional characteristic, which is not unlike that of an open-end waveguide in free space, that the Huygens' source was chosen to model the waveguide excitation of the dielectric sphere. The source can only be approximated in the presence of the dielectric sphere because the complex wave impedance η is not known.

Although, in general, η would be a function of sphere diameter and constitution as well as source location, the following current relations are used to construct the source

$$C_m = \eta_1 C_e \qquad (b_1 > a) \qquad (6)$$

$$C_m = \eta_2 C_e \qquad (b_1 \leq a) \qquad (7)$$

where $\eta_1 = \sqrt{\mu_1/\epsilon_1}$ and $\eta_2 = \sqrt{\mu_2/\epsilon_2}$. Equation (6) was chosen because it would be valid if $b_1 >> a$, since for this case the sphere would have little effect upon the source. Alternately, equation (7) would be appropriate for the source located within or on the surface of a large lossy dielectric sphere. Also, it has been found that equation (7) yields a good approximation to the Huygens' source on the surface of small spheres.

Dyadic Green's Functions Pertaining to the Dielectric Sphere

Under the assumption that the current distribution is a known function of position, the radiation from a dielectric sphere may be investigated as a boundary-value problem and the solution may be obtained by the technique of dyadic Green's functions.

Figure 37 shows the geometry of a dielectric sphere with an electric current source located at $\bar{R}'$. With the source located outside the sphere in region I, the electric fields in regions I and II may be expressed by

$$\bar{E}(\bar{R}) = i\omega\mu_1 \iiint \bar{\bar{G}}_3^{(11)}(\bar{R}|\bar{R}') \cdot \bar{J}(\bar{R}')\, dV' \qquad \text{(Region I)} \qquad (8)$$

$$\bar{E}(\bar{R}) = i\omega\mu_1 \iiint \bar{\bar{G}}_3^{(21)}(\bar{R}|\bar{R}') \cdot \bar{J}(\bar{R}')\, dV' \qquad \text{(Region II)} \qquad (9)$$

Similarly, with the source located inside the sphere

$$\bar{E}(\bar{R}) = i\omega\mu_2 \iiint \bar{\bar{G}}_3^{(12)}(\bar{R}|\bar{R}') \cdot \bar{J}(\bar{R}')\, dV' \qquad \text{(Region I)} \qquad (10)$$

$$\bar{E}(\bar{R}) = i\omega\mu_2 \iiint \bar{\bar{G}}_3^{(22)}(\bar{R}|\bar{R}') \cdot \bar{J}(\bar{R}')\, dV' \qquad \text{(Region II)} \qquad (11)$$

where $\bar{\bar{G}}_3(\bar{R}|\bar{R}')$ is the dyadic Green's function of the third kind and the harmonic time factor $e^{-i\omega t}$ has been suppressed. The superscripts m and n of the Green's functions in equations (8) to (11) denote the regions of the observation and source points, respectively Those functions are solutions to the vector wave equations

$$\left.\begin{aligned} \nabla \times \nabla \times \bar{\bar{G}}_3 - k_1^2 \bar{\bar{G}}_3 &= \bar{\bar{I}}\,\delta(\bar{R} - \bar{R}') \qquad (R \geq a) \\ \nabla \times \nabla \times \bar{\bar{G}}_3 - k_2^2 \bar{\bar{G}}_3 &= 0 \qquad (R \leq a) \end{aligned}\right\} \qquad (12)$$

Besides satisfying the radiation condition at infinity,

$$\lim_{R\to\infty} R\left[\nabla \times \bar{\bar{G}}_3(\bar{R}|\bar{R}') - ik\hat{R} \times \bar{\bar{G}}_3(\bar{R}|\bar{R}')\right] = 0$$

$\bar{\bar{G}}_3$ also satisfies the boundary conditions at the surface of the sphere; that is,

$$\left.\begin{aligned} \hat{n} \times \bar{\bar{G}}_3(\bar{R}|\bar{R}')\big|_{\bar{R}=a_-} &= \hat{n} \times \bar{\bar{G}}_3(\bar{R}|\bar{R}')\big|_{R=a_+} \\ \frac{1}{\mu_1}\hat{n} \times \nabla \times \bar{\bar{G}}_3(\bar{R}|\bar{R}')\Big|_{R=a_-} &= \frac{1}{\mu_2}\, n \times \nabla \times \bar{\bar{G}}_3(\bar{R}|\bar{R}')\Big|_{R=a_+} \end{aligned}\right\} \qquad (13)$$

The simplest way to find $\bar{\bar{G}}_3(\bar{R}|\bar{R}')$ is to use the method of scattering superposition in which the fields are assumed to consist of a sum of incident and scattered waves. With this method the form of the scattered waves are first constructed using eigenfunctions which will satisfy the boundary conditions at the sphere surface, as well as having the proper form at $R = 0$ and $R = \infty$. The coefficients of the scattered waves are then determined by matching the boundary conditions on the surface of the sphere.

Thus $\bar{\bar{G}}_3(\bar{R}|\bar{R}')$ is treated as consisting of two parts:

$$\bar{\bar{G}}_3^{(11)}(\bar{R}|\bar{R}') = \bar{\bar{G}}_0(\bar{R}|\bar{R}') + \bar{\bar{G}}_{3s}(\bar{R}|\bar{R}') \qquad (R \geq a) \tag{14}$$

$$\bar{\bar{G}}_3^{(21)}(\bar{R}|\bar{R}') = \bar{\bar{G}}_{3s}^{(21)}(\bar{R}|\bar{R}') \qquad (R \leq a) \tag{15}$$

Here, $\bar{\bar{G}}_0(\bar{R}|\bar{R}')$ denotes the free-space dyadic Green's function pertaining to an infinite region with the same constitutive parameters as region I, $\bar{\bar{G}}_{3s}(\bar{R}|\bar{R}')$ represents the part of the wave scattered from the sphere, and $\bar{\bar{G}}_{3s}^{(21)}(\bar{R}|\bar{R}')$ is used to denote the Green's function internal to the sphere since only a scattered field will be present in this region.

The free-space Green's function for this problem is given by Tai (ref. 4) as follows:

$$\left.\begin{aligned}
\bar{\bar{G}}_0(\bar{R}|\bar{R}') = \frac{ik_1}{4\pi} \sum_{n=1}^{\infty} \sum_{m=0}^{n} (2 - \delta_0) \frac{2n+1}{n(n+1)} \frac{(n-m)!}{(n+m)!} \Big[& \bar{M}_{e_{0mn}}^{(1)}(k_1)\, \bar{M}'_{e_{0mn}}(k_1) \\
& + \bar{N}_{e_{0mn}}^{(1)}(k_1)\, \bar{N}'_{e_{0mn}}(k_1) \Big] \qquad (R > R') \\
\bar{\bar{G}}_0(\bar{R}|\bar{R}') = \frac{ik_1}{4\pi} \sum_{n=1}^{\infty} \sum_{m=0}^{n} (2 - \delta_0) \frac{2n+1}{n(n+1)} \frac{(n-m)!}{(n+m)!} \Big[& \bar{M}_{e_{0mn}}(k_1)\, \bar{M}'^{(1)}_{e_{0mn}}(k_1) \\
& + \bar{N}_{e_{0mn}}(k_1)\, \bar{N}'^{(1)}_{e_{0mn}}(k_1) \Big] \qquad (R < R')
\end{aligned}\right\} \tag{16}$$

where

$$\delta_0 = \begin{cases} 1 & (m = 0) \\ 0 & (m \neq 0) \end{cases}$$

and

$$\bar{M}_{\substack{e \\ 0}mn}(k) = j_n(kR) \left[\mp \frac{m}{\sin\theta} P_n^m(\cos\theta) \begin{matrix}\sin \\ \cos\end{matrix} m\phi\hat{\theta} - \frac{\partial P_n^m(\cos\theta)}{\partial\theta} \begin{matrix}\cos \\ \sin\end{matrix} m\phi\hat{\phi} \right] \quad (17)$$

$$\bar{N}_{\substack{e \\ 0}mn}(k) = \frac{n(n+1)}{kR} j_n(kR) P_n^m(\cos\theta) \begin{matrix}\cos \\ \sin\end{matrix} m\phi\hat{R}$$

$$+ \frac{1}{kR} \frac{\partial}{\partial R} \left[Rj_n(kR) \right] \cdot \left[\frac{\partial P_n^m(\cos\theta)}{\partial\theta} \begin{matrix}\cos \\ \sin\end{matrix} m\phi\hat{\theta} \mp \frac{P_n^m(\cos\theta)}{\sin\theta} m\phi\hat{\phi} \right] \quad (18)$$

The two sets of spherical vector wave functions represented by $\bar{M}$ and $\bar{N}$ are solutions to the homogeneous vector wave equation

$$\nabla \times \nabla \times \bar{F} - k^2 F = 0$$

as shown by Stratton (ref. 5), and also satisfy the symmetrical equations

$$\bar{N}_{\substack{e \\ 0}mn}(k) = \frac{1}{k} \nabla \times \bar{M}_{\substack{e \\ 0}mn}(k) \quad (19)$$

$$\bar{M}_{\substack{e \\ 0}mn}(k) = \frac{1}{k} \nabla \times \bar{N}_{\substack{e \\ 0}mn}(k) \quad (20)$$

In equations (17) and (18), $j_n(kR)$ denotes the spherical Bessel function of order n and $P_n^m(\cos\theta)$ represents the associated Legendre function of degree n and order m. The expressions in equation (16) with superscript (1) are obtained from equations (17) and (18) by replacing the spherical Bessel functions with spherical Hankel functions of the first kind, that is, $h_n^{(1)}(kR)$. A prime used on a function denotes that it is defined with respect to the primed coordinate variables (R', θ', ϕ') pertaining to the vector $\bar{R}'$.

In constructing $\bar{\bar{G}}_3(\bar{R}|\bar{R}')$ from the wave functions, the following observations are made:

(1) For the source located exterior to the sphere, the posterior parts of $\bar{\bar{G}}_{3s}^{(11)}(\bar{R}|\bar{R}')$ and $\bar{\bar{G}}_{3s}^{(21)}(\bar{R}|\bar{R}')$ must be the same as $\bar{\bar{G}}_0(\bar{R}|\bar{R}')$ evaluated at $R < R'$. This is necessary to match the boundary conditions at the sphere surface.

(2) The propagation constants k_1 and k_2 must be used in the anterior parts of $\bar{\bar{G}}_{3s}^{(11)}(\bar{R}|\bar{R}')$ and $\bar{\bar{G}}_{3s}^{(21)}(\bar{R}|\bar{R}')$, respectively, because of the regions in which the observation points are located.

(3) The spherical Hankel functions must be used in the anterior parts of $\bar{\bar{G}}_{3s}^{(11)}(\bar{R}|\bar{R}')$ because these functions represent outward traveling waves.

(4) Finally, since the fields are finite at the origin, the anterior parts of $\bar{\bar{G}}_{3s}^{(21)}(\bar{R}|\bar{R}')$ must be constructed using the spherical Bessel functions.

In keeping with these requirements, let

$$\bar{\bar{G}}_{3s}^{(11)}(\bar{R}|\bar{R}') = \frac{ik_1}{4\pi} \sum_{n=1}^{\infty} \sum_{m=0}^{n} (2 - \delta_0) \frac{2n+1}{n(n+1)} \frac{(n-m)!}{(n+m)!} \left[a_{\substack{e \\ 0}mn}^{(1)} \bar{M}_{\substack{e \\ 0}mn}^{(1)}(k_1) \bar{M}'^{(1)}_{\substack{e \\ 0}mn}(k_1) + b_{\substack{e \\ 0}mn}^{(1)} \bar{N}_{\substack{e \\ 0}mn}^{(1)}(k_1) \bar{N}'^{(1)}_{\substack{e \\ 0}mn}(k_1) \right] \tag{21}$$

and

$$\bar{\bar{G}}_{3s}^{(21)}(\bar{R}|\bar{R}') = \frac{ik_1}{4\pi} \sum_{n=1}^{\infty} \sum_{m=0}^{n} (2 - \delta_0) \frac{2n+1}{n(n+1)} \frac{(n-m)!}{(n+m)!} \left[c_{\substack{e \\ 0}mn}^{(1)} \bar{M}_{\substack{e \\ 0}mn}(k_2) \bar{M}'^{(1)}_{\substack{e \\ 0}mn}(k_1) + d_{\substack{e \\ 0}mn}^{(1)} \bar{N}_{\substack{e \\ 0}mn}(k_2) \bar{N}'^{(1)}_{\substack{e \\ 0}mn}(k_1) \right] \tag{22}$$

The scattering coefficients a, b, c, and d in equations (21) and (22) are complex quantities and represent the magnitude and phase of the sphere's contribution to the total fields. The superscripts (1) on these coefficients denote that they are defined for the source located in region I (fig. 37) and should not be confused with the meaning of a superscript on a spherical wave function.

Since the tangential components of the resulting fields $\bar{E}$ and $\bar{H}$ must be continuous across the sphere surface, the boundary conditions from equation (13) are applied and become, for $R = a$

$$\left.\begin{aligned} \hat{R} \times \bar{\bar{G}}_3^{(11)}(\bar{R}|\bar{R}') &= \hat{R} \times \bar{\bar{G}}_3^{(21)}(\bar{R}|\bar{R}') \\ \frac{1}{\mu_1} \hat{R} \times \nabla \times \bar{\bar{G}}_3^{(11)}(\bar{R}|\bar{R}') &= \frac{1}{\mu_2} \hat{R} \times \bar{\bar{G}}_3^{(21)}(\bar{R}|\bar{R}') \end{aligned}\right\} \tag{23}$$

Solving equations (23) for the coefficients results in $a_{e_{0mn}}^{(1)} = a_n^{(1)}$, $b_{e_{0mn}}^{(1)} = b_n^{(1)}$, $c_{e_{0mn}}^{(1)} = c_n^{(1)}$, and $d_{e_{0mn}}^{(1)} = d_n^{(1)}$ where

$$a_n^{(1)} = \frac{\left[\rho_2 j_n(\rho_2)\right]' j_n(\rho_1) - \left[\rho_1 j_n(\rho_1)\right]' j_n(\rho_2)}{\left[\rho_1 h_n(\rho_1)\right]' j_n(\rho_2) - \left[\rho_2 j_n(\rho_2)\right]' h_n(\rho_1)} \tag{24}$$

$$b_n^{(1)} = \frac{\left[\rho_2 j_n(\rho_2)\right]' j_n(\rho_1) - \epsilon_r \left[\rho_1 j_n(\rho_1)\right]' j_n(\rho_2)}{\epsilon_r \left[\rho_1 h_n(\rho_1)\right]' j_n(\rho_2) - \left[\rho_2 j_n(\rho_2)\right]' h_n(\rho_1)} \tag{25}$$

$$c_n^{(1)} = \frac{\left[\rho_1 h_n(\rho_1)\right]' j_n(\rho_1) - \left[\rho_1 j_n(\rho_1)\right]' h_n(\rho_1)}{\left[\rho_1 h_n(\rho_1)\right]' j_n(\rho_2) - \left[\rho_2 j_n(\rho_2)\right]' h_n(\rho_1)} \tag{26}$$

$$d_n^{(1)} = \frac{\sqrt{\epsilon_r}\left[\rho_1 h_n^{(1)}(\rho_1)\right]' j_n(\rho_1) - \sqrt{\epsilon_r}\left[\rho_1 j_n(\rho_1)\right]' h_n(\rho_1)}{\epsilon_r \left[\rho_1 h_n^{(1)}(\rho_1)\right]' j_n(\rho_2) - \left[\rho_2 j_n(\rho_2)\right]' h_n(\rho_1)} \tag{27}$$

Here,

$$\rho_1 = k_1 a$$

$$\rho_2 = k_2 a$$

$$\left[\rho z_n(\rho)\right]' = \frac{\partial}{\partial\rho}\left[\rho z_n(\rho)\right]$$

$$\mu_1 = \mu_2 = \mu_0$$

$$\epsilon_1 = \epsilon_0$$

$$\frac{\epsilon_2}{\epsilon_0} = \epsilon_r$$

where ϵ_r is the relative dielectric constant and may be complex, and $z_n(\rho)$ is either $j_n(\rho)$ or $h_n(\rho)$; also, $h_n(\rho)$ denotes $h_n^{(1)}(\rho)$ since only the spherical Hankel function of the first kind appears in this work.

Substitution of equations (16), (21), and (17) into equations (14) and (15) yields the Green's functions for the externally located source. They are as follows:

Electric source in region I, observation point in region I:

$$\bar{\bar{G}}_3^{(11)}(\bar{R}|\bar{R}') = \frac{ik_1}{4\pi}\sum_{n=1}^{\infty}\sum_{m=0}^{n}(2-\delta_0)\frac{2n+1}{n(n+1)}\frac{(n-m)!}{(n+m)!}\left\{\bar{M}_{\substack{e\\0}mn}^{(1)}(k_1)\left[\bar{M}'_{\substack{e\\0}mn}(k_1) + a_n^{(1)}\bar{M}'^{(1)}_{\substack{e\\0}mn}(k_1)\right] + \bar{N}_{\substack{e\\0}mn}^{(1)}(k_1)\left[\bar{N}'_{\substack{e\\0}mn}(k_1) + b_n^{(1)}\bar{N}'^{(1)}_{\substack{e\\0}mn}(k_1)\right]\right\} \tag{28}$$

for $R > R'$, and

$$\bar{\bar{G}}_3^{(11)}(\bar{R}|\bar{R}') = \frac{ik_1}{4\pi}\sum_{n=1}^{\infty}\sum_{m=0}^{n}(2-\delta_0)\frac{2n+1}{n(n+1)}\frac{(n-m)!}{(n+m)!}\left\{\left[\bar{M}_{\substack{e\\0}mn}(k_1) + a_n^{(1)}\bar{M}_{\substack{e\\0}mn}^{(1)}(k_1)\right]\bar{M}'^{(1)}_{\substack{e\\0}mn}(k_1) + \left[\bar{N}_{\substack{e\\0}mn}(k_1) + b_n^{(1)}\bar{N}_{\substack{e\\0}mn}^{(1)}(k_1)\right]\bar{N}'^{(1)}_{\substack{e\\0}mn}(k_1)\right\} \tag{29}$$

for $a \leqq R < R'$.

Electric source in region I, observation point in region II:

$$\bar{\bar{G}}_3^{(21)}(\bar{R}|\bar{R}') = \frac{ik_1}{4\pi}\sum_{n=1}^{\infty}\sum_{m=0}^{n}(2-\delta_0)\frac{2n+1}{n(n+1)}\frac{(n-m)!}{(n+m)!}\left[c_n^{(1)}\bar{M}_{e_{0mn}}(k_2)\bar{M}'^{(1)}_{e_{0mn}}(k_1)\right.$$

$$\left.+\, d_n^{(1)}\bar{N}_{e_{0mn}}(k_2)\bar{N}'^{(1)}_{e_{0mn}}(k_1)\right] \tag{30}$$

for $R \leq a$.

For the source located inside the dielectric sphere, again consider the geometry of figure 37, but now with $R' \leq a$. Let $\bar{\bar{G}}_0^{(22)}(\bar{R}|\bar{R}')$ represent the free-space Green's function in an infinite region with the same constitutive parameters as that of region II. From equation (16)

$$\bar{\bar{G}}_0^{(22)}(\bar{R}|\bar{R}') = \frac{ik_2}{4\pi}\sum_{n=1}^{\infty}\sum_{m=0}^{n}(2-\delta_0)\frac{2n+1}{n(n+1)}\frac{(n-m)!}{(n+m)!}\left[\bar{M}^{(1)}_{e_{0mn}}(k_2)\bar{M}'_{e_{0mn}}(k_2)\right.$$

$$\left.+\,\bar{N}^{(1)}_{e_{0mn}}(k_2)\bar{N}'_{e_{0mn}}(k_2)\right] \qquad (R > R') \tag{31a}$$

$$\bar{\bar{G}}_0^{(22)}(\bar{R}|\bar{R}') = \frac{ik_2}{4\pi}\sum_{n=1}^{\infty}\sum_{m=0}^{n}(2-\delta_0)\frac{2n+1}{n(n+1)}\frac{(n-m)!}{(n+m)!}\left[\bar{M}_{e_{0mn}}(k_2)\bar{M}'^{(1)}_{e_{0mn}}(k_2)\right.$$

$$\left.+\,\bar{N}_{e_{0mn}}(k_2)\bar{N}'^{(1)}_{e_{0mn}}(k_2)\right] \qquad (R < R') \tag{31b}$$

Using the method of scattering superposition, $\bar{\bar{G}}_3^{(22)}(\bar{R}|\bar{R}')$ is treated as consisting of two parts, namely,

$$\bar{\bar{G}}_3^{(22)}(\bar{R}|\bar{R}') = \bar{\bar{G}}_0^{(22)}(\bar{R}|\bar{R}') + \bar{\bar{G}}_{3s}^{(22)}(\bar{R}|\bar{R}') \qquad (R \leq a) \tag{32}$$

$$\bar{\bar{G}}_3^{(12)}(\bar{R}|\bar{R}') = \bar{\bar{G}}_{3s}^{(12)}(\bar{R}|\bar{R}') \qquad (R \geq a) \tag{33}$$

where $\bar{\bar{G}}_{3s}^{(22)}$ represents the portion of $\bar{\bar{G}}_3$ which is scattered from the inside surface of the dielectric sphere and $\bar{\bar{G}}_3^{(12)}$ is the transmitted field. It is noted that $\bar{\bar{G}}_{3s}^{(22)}$ must be finite at the origin, that $\bar{\bar{E}}_3^{(12)}$ must satisfy the radiation condition at infinity, and that the boundary conditions must be met at the sphere surface. Thus

$$\bar{\bar{G}}_{3s}^{(12)}(\bar{R}|\bar{R}') = \frac{ik_2}{4\pi}\sum_{n=1}^{\infty}\sum_{m=0}^{n}(2-\delta_0)\frac{2n+1}{n(n+1)}\frac{(n-m)!}{(n+m)!}\left[a_{\substack{e\\0}mn}^{(2)}\bar{M}_{\substack{e\\0}mn}^{(1)}(k_1)\bar{M}'_{\substack{e\\0}mn}(k_2) + b_{\substack{e\\0}mn}^{(2)}\bar{N}_{\substack{e\\0}mn}^{(1)}(k_1)\bar{N}'_{\substack{e\\0}mn}(k_2)\right] \qquad (R > a) \tag{34}$$

and

$$\bar{\bar{G}}_{3s}^{(22)}(\bar{R}|\bar{R}') = \frac{ik_2}{4\pi}\sum_{n=1}^{\infty}\sum_{m=0}^{n}(2-\delta_0)\frac{2n+1}{n(n+1)}\frac{(n-m)!}{(n+m)!}\left[c_{\substack{e\\0}mn}^{(2)}\bar{M}_{\substack{e\\0}mn}(k_2)\bar{M}'_{\substack{e\\0}mn}(k_2) + d_{\substack{e\\0}mn}^{(2)}\bar{N}_{\substack{e\\0}mn}(k_2)\bar{N}'_{\substack{e\\0}mn}(k_2)\right] \qquad (R < a) \tag{35}$$

where the superscript (2) on the scattering coefficients denotes that they pertain to the source located in region II.

The coefficients are now found by applying the boundary conditions at the sphere surface, namely, for R = a

$$\hat{R}\times\bar{\bar{G}}_3^{(12)}(\bar{R}|\bar{R}') = \hat{R}\times\bar{\bar{G}}_3^{(22)}(\bar{R}|\bar{R}')$$

$$\frac{1}{\mu_1}\hat{R}\times\nabla\times\bar{\bar{G}}_3^{(12)}(\bar{R}|\bar{R}') = \frac{1}{\mu_2}\hat{R}\times\nabla\times\bar{\bar{G}}_3^{(22)}(\bar{R}|\bar{R}')$$

Again it is found that $a_{\substack{e\\0}mn}^{(2)} = a_n^{(2)}$, $b_{\substack{e\\0}mn}^{(2)} = b_n^{(2)}$, $c_{\substack{e\\0}mn}^{(2)} = c_n^{(2)}$, and $d_{\substack{e\\0}mn}^{(2)} = d_n^{(2)}$, where for the case $\mu_1 = \mu_2$,

$$a_n^{(2)} = \frac{\left[\rho_2 j_n(\rho_2)\right]' h_n(\rho_2) - \left[\rho_2 h_n(\rho_2)\right]' j_n(\rho_2)}{\left[\rho_2 j_n(\rho_2)\right]' h_n(\rho_1) - \left[\rho_1 h_n(\rho_1)\right]' j_n(\rho_2)} \tag{36}$$

$$b_n^{(2)} = \frac{\left[\rho_2 j_n(\rho_2)\right]' h_n(\rho_2) - \left[\rho_2 h_n(\rho_2)\right]' j_n(\rho_2)}{\frac{1}{\sqrt{\epsilon_r}}\left[\rho_2 j_n(\rho_2)\right]' h_n(\rho_1) - \sqrt{\epsilon_r}\left[\rho_1 h_n(\rho_1)\right]' j_n(\rho_2)} \tag{37}$$

$$c_n^{(2)} = \frac{\left[\rho_1 h_n(\rho_1)\right]' h_n(\rho_2) - \left[\rho_2 h_n(\rho_2)\right]' h_n(\rho_1)}{\left[\rho_2 j_n(\rho_2)\right]' h_n(\rho_1) - \left[\rho_1 h_n(\rho_1)\right]' j_n(\rho_2)} \tag{38}$$

$$d_n^{(2)} = \frac{\epsilon_r \left[\rho_1 h_n(\rho_1)\right]' h_n(\rho_2) - \left[\rho_2 h_n(\rho_2)\right]' h_n(\rho_1)}{\left[\rho_2 j_n(\rho_2)\right]' h_n(\rho_1) - \left[\rho_1 h_n(\rho_1)\right]' j_n(\rho_2)\,\epsilon_r} \tag{39}$$

Substitution of equations (31), (34), and (35) into (33) yields the desired Green's functions for the internally located electric current source as follows:

Electric source in region II, observation point in region I:

$$\bar{\bar{G}}_3^{(12)}(\bar{R}|\bar{R}') = \frac{ik_2}{4\pi} \sum_{n=1}^{\infty} \sum_{m=0}^{n} (2 - \delta_0) \frac{2n+1}{n(n+1)} \frac{(n-m)!}{(n+m)!} \left[a_n^{(2)} \bar{M}_{e\,0mn}^{(1)}(k_1) \bar{M}'_{e\,0mn}(k_2) + b_n^{(2)} \bar{N}_{e\,0mn}^{(1)}(k_1) \bar{N}'_{e\,0mn}(k_2) \right] \qquad (R > a) \tag{40}$$

Electric source in region II, observation point in region II:

$$\bar{\bar{G}}_3^{(22)}(\bar{R}|\bar{R}') = \frac{ik_2}{4\pi} \sum_{n=1}^{\infty} \sum_{m=0}^{n} (2 - \delta_0) \frac{2n+1}{n(n+1)} \frac{(n-m)!}{(n+m)!} \left\{ \left[\bar{M}_{e\,0mn}^{(1)}(k_2) + c_n^{(2)} \bar{M}_{e\,0mn}(k_2) \right] \bar{M}'_{e\,0mn}(k_2) + \left[\bar{N}_{e\,0mn}^{(1)}(k_2) + d_n^{(2)} \bar{N}_{e\,0mn}(k_2) \right] \bar{N}'_{e\,0mn}(k_2) \right\} \tag{41}$$

for $a \geq R > R'$ and

$$\bar{\bar{G}}_3^{(22)}(\bar{R}|\bar{R}') = \frac{ik_2}{4\pi} \sum_{n=1}^{\infty} \sum_{m=0}^{n} (2 - \delta_0) \frac{2n+1}{n(n+1)} \frac{(n-m)!}{(n+m)!} \left\{ \bar{M}_{e_{0mn}}(k_2) \left[\bar{M}'^{(1)}_{e_{0mn}}(k_2) + c_n^{(2)} \bar{M}'_{e_{0mn}}(k_2) \right] + \bar{N}_{e_{0mn}}(k_2) \left[\bar{N}'^{(1)}_{e_{0mn}}(k_2) + d_n^{(2)} \bar{N}'_{e_{0mn}}(k_2) \right] \right\} \quad (42)$$

for $R < R'$.

The dyadic Green's function of the fourth kind may be used to obtain expressions for the fields due to the magnetic current source. The magnetic field is given in terms of these functions for the appropriate regions of source and observation points as follows:

$$\bar{H}(\bar{R}) = i\omega\epsilon_1 \iiint \bar{\bar{G}}_4^{(11)}(\bar{R}|\bar{R}') \cdot \bar{J}_m(\bar{R}')\, dV' \quad (43)$$

$$\bar{H}(\bar{R}) = i\omega\epsilon_1 \iiint \bar{\bar{G}}_4^{(21)}(\bar{R}|\bar{R}') \cdot \bar{J}_m(\bar{R}')\, dV' \quad (44)$$

$$\bar{H}(\bar{R}) = i\omega\epsilon_2 \iiint \bar{\bar{G}}_4^{(12)}(\bar{R}|\bar{R}') \cdot \bar{J}_m(\bar{R}')\, dV' \quad (45)$$

$$\bar{H}(\bar{R}) = i\omega\epsilon_2 \iiint \bar{\bar{G}}_4^{(22)}(\bar{R}|\bar{R}') \cdot \bar{J}_m(\bar{R}')\, dV' \quad (46)$$

where $\bar{J}_m$ is the magnetic current density.

The functions $\bar{\bar{G}}_4$ may be derived from $\bar{\bar{G}}_3$ using the principle of duality and are as follows:

Magnetic source in region I, observation point in region I:

$$\bar{\bar{G}}_4^{(11)}(\bar{R}|\bar{R}') = \frac{ik_1}{4\pi} \sum_{n=1}^{\infty} \sum_{m=0}^{n} (2 - \delta_0) \frac{2n+1}{n(n+1)} \frac{(n-m)!}{(n+m)!} \left\{ \bar{M}_{\substack{e \\ 0}mn}^{(1)}(k_1) \left[\bar{M}'_{\substack{e \\ 0}mn}(k_1) + b_n^{(1)} \bar{M}'^{(1)}_{\substack{e \\ 0}mn}(k_1) \right] + \bar{N}_{\substack{e \\ 0}mn}^{(1)}(k_1) \left[\bar{N}'_{\substack{e \\ 0}mn}(k_1) + a_n^{(1)} \bar{N}'^{(1)}_{\substack{e \\ 0}mn}(k_1) \right] \right\} \tag{47}$$

for $R > R'$ and

$$\bar{\bar{G}}_4^{(11)}(\bar{R}|\bar{R}') = \frac{ik_1}{4\pi} \sum_{n=1}^{\infty} \sum_{m=0}^{n} (2 - \delta_0) \frac{2n+1}{n(n+1)} \frac{(n-m)!}{(n+m)!} \left\{ \left[\bar{M}_{\substack{e \\ 0}mn}(k_1) + b_n^{(1)} \bar{M}_{\substack{e \\ 0}mn}^{(1)}(k_1) \right] \bar{M}'^{(1)}_{\substack{e \\ 0}mn}(k_1) + \left[\bar{N}_{\substack{e \\ 0}mn}(k_1) + a_n^{(1)} \bar{N}_{\substack{e \\ 0}mn}^{(1)}(k_1) \right] \bar{N}'^{(1)}_{\substack{e \\ 0}mn}(k_1) \right\} \tag{48}$$

for $a \leq R < R'$.

Magnetic source in region I, observation point in region II:

$$\bar{\bar{G}}_4^{(21)}(\bar{R}|\bar{R}') = \frac{ik_2}{4\pi} \sum_{n=1}^{\infty} \sum_{m=0}^{n} (2 - \delta_0) \frac{2n+1}{n(n+1)} \frac{(n-m)!}{(n+m)!} \left[d_n^{(1)} \bar{M}_{\substack{e \\ 0}mn}(k_2) \bar{M}'^{(1)}_{\substack{e \\ 0}mn}(k_1) + c_n^{(1)} \bar{N}_{\substack{e \\ 0}mn}(k_2) \bar{N}'^{(1)}_{\substack{e \\ 0}mn}(k_1) \right] \tag{49}$$

for $R \leq a$.

Magnetic source in region II, observation point in region I:

$$\bar{\bar{G}}_4^{(12)}(\bar{R}|\bar{R}') = \frac{ik_1}{4\pi} \sum_{n=1}^{\infty} \sum_{m=0}^{n} (2 - \delta_0) \frac{2n+1}{n(n+1)} \frac{(n-m)!}{(n+m)!} \left[b_n^{(2)} \bar{M}_{\substack{e \\ 0}mn}^{(1)}(k_1) \bar{M}'_{\substack{e \\ 0}mn}(k_2) + a_n^{(2)} \bar{N}_{\substack{e \\ 0}mn}(k_1) \bar{N}'_{\substack{e \\ 0}mn}(k_2) \right] \tag{50}$$

for $R > a$.

Magnetic source in region II, observation point in region II:

$$\bar{\bar{G}}_4^{(22)}(\bar{R}|\bar{R}') = \frac{ik_2}{4\pi} \sum_{n=1}^{\infty} \sum_{m=0}^{n} (2 - \delta_0) \frac{2n+1}{n(n+1)} \frac{(n-m)!}{(n+m)!} \left\{ \left[\bar{M}_{\substack{e \\ 0}mn}^{(1)}(k_2) + d_n^{(2)} \bar{M}_{\substack{e \\ 0}mn}(k_2) \right] \bar{M}'_{\substack{e \\ 0}mn}(k_2) + \left[\bar{N}_{\substack{e \\ 0}mn}^{(1)}(k_2) + c_n^{(2)} \bar{N}_{\substack{e \\ 0}mn}(k_2) \right] \bar{N}'_{\substack{e \\ 0}mn}(k_2) \right\} \tag{51}$$

for $a > R > R'$, and

$$\bar{\bar{G}}_4^{(22)}(\bar{R}|\bar{R}') = \frac{ik_2}{4\pi} \sum_{n=1}^{\infty} \sum_{m=0}^{n} (2 - \delta_0) \frac{2n+1}{n(n+1)} \frac{(n-m)!}{(n+m)!} \left\{ \bar{M}_{\substack{e \\ 0}mn}(k_2) \left[\bar{M}'^{(1)}_{\substack{e \\ 0}mn}(k_2) + d_n^{(2)} \bar{M}'_{\substack{e \\ 0}mn}(k_2) \right] + \bar{N}_{\substack{e \\ 0}mn}(k_2) \left[\bar{N}'^{(1)}_{\substack{e \\ 0}mn}(k_2) + c_n^{(2)} \bar{N}'_{\substack{e \\ 0}mn}(k_2) \right] \right\} \tag{52}$$

for $R < R'$.

Electric Fields Due to a Huygens' Source in the Presence of a Dielectric Sphere

For the source located as shown in figure 36, the electric and magnetic current densities are represented by

$$\bar{J}(\bar{R}') = C_e \frac{\delta(R' - b_1)\ \delta(\theta')\ \delta(\phi')}{b_1^2 \sin\theta'} \hat{x} \tag{53}$$

and

$$\bar{J}_m(\bar{R}') = - C_m \frac{\delta(R' - b_1)\ \delta(\theta')\ \delta(\phi')}{b_1^2 \sin\theta'} \hat{y} \tag{54}$$

respectively. The electric fields due to the current given in equation (53) are easily found by using equations (8) to (11). In order to obtain the electric fields due to the magnetic source, however, equations (43) to (46) are used together with Maxwell's equation for a source-free region

$$\bar{E} = \frac{i}{\omega\epsilon} \nabla \times \bar{H} \tag{55}$$

The curl operator is easily performed in view of the symmetrical relation for the vector wave functions of equation (20).

The resulting fields for the combined source may be represented as follows:

Source in region I, observation point in region I:

$$\bar{E}_H(\bar{R}) = \frac{-k_1 \omega\mu C_e}{4\pi} \sum_{n=1}^{\infty} \frac{2n+1}{n(n+1)} \left[\left(A_n^{(1)} + D_n^{(1)} \right) \bar{M}_{01n}^{(1)}(k_1) + \left(B_n^{(1)} + C_n^{(1)} \right) \bar{N}_{e1n}^{(1)}(k_1) \right] \tag{56}$$

for $R > b_1$ and

$$\bar{E}_H(\bar{R}) = \frac{-k_1 \omega\mu C_e}{4\pi} \sum_{n=1}^{\infty} \frac{2n+1}{n(n+1)} \left(\left\{ h_n(\rho_3) - i \frac{\left[\rho_3 h_n(\rho_3)\right]'}{\rho_3} \right\} \left[\bar{M}_{01n}(k_1) + a_n^{(1)} \bar{M}_{01n}^{(1)}(k_1) \right] + \left\{ \frac{\left[\rho_3 h_n(\rho_3)\right]'}{\rho_3} + i h_n(\rho_3) \right\} \left[\bar{N}_{e1n}(k_1) + b_n^{(1)} \bar{N}_{e1n}^{(1)}(k_1) \right] \right) \tag{57}$$

for $a \leq R < b_1$.

Source in region I, observation point in region II:

$$\bar{E}_H(\bar{R}) = \frac{-k_1 \omega\mu C_e}{4\pi} \sum_{n=1}^{\infty} \frac{2n+1}{n(n+1)} \left(\left\{ h_n(\rho_3) - \left[\rho_3 h_n(\rho_3)\right]' \right\} c_n^{(1)} \bar{M}_{01n}(k_2) + \left\{ \frac{\left[\rho_3 h_n(\rho_3)\right]'}{\rho_3} + i h_n(\rho_3) \right\} d_n^{(1)} \bar{N}_{e1n}(k_2) \right)$$

for $0 \leq R \leq a$.

Source in region II, observation point in region I:

$$\bar{E}_H(\bar{R}) = \frac{-k_1 \omega\mu C_e}{4\pi} \sum_{n=1}^{\infty} \frac{2n+1}{n(n+1)} \left[\left(A_n^{(2)} + D_n^{(2)} \right) \bar{M}_{01n}^{(1)}(k_1) + \left(B_n^{(2)} + C_n^{(2)} \right) \bar{N}_{e1n}^{(1)}(k_1) \right] \tag{59}$$

for $R > a$.

Source in region II, observation point in region II:

$$\bar{E}_H(\bar{R}) = \frac{-k_2 \omega\mu C_e}{4\pi} \sum_{n=1}^{\infty} \frac{2n+1}{n(n+1)} \left(\left\{ j_n(\rho_4) - i \frac{\left[\rho_4 j_n(\rho_4)\right]'}{4\pi} \right\} \left[\bar{M}_{01n}^{(1)}(k_2) + c_n^{(2)} \bar{M}_{01n}(k_2) \right] + \left\{ \frac{\left[\rho_4 j_n(\rho_4)\right]'}{\rho_4} + i j_n(\rho_4) \right\} \left[\bar{N}_{e1n}^{(1)}(k_2) + d_n^{(2)} \bar{N}_{e1n}(k_2) \right] \right) \tag{60}$$

for $a \geq R > b_1$.

$$\bar{E}_H(\bar{R}) = \frac{-k_2 \omega\mu C_E}{4\pi} \sum_{n=1}^{\infty} \frac{2n+1}{n(n+1)} \left(\left\{ h_n(\rho_4) + c_n^{(2)} j_n(\rho_4) - i \frac{\left[\rho_4 h_n(\rho_4)\right]'}{\rho_4} - i c_n^{(2)} \frac{\left[\rho_4 j_n(\rho_4)\right]'}{\rho_4} \right\} \bar{M}_{01n}(k_2) + \left\{ \frac{\left[\rho_4 h_n(\rho_4)\right]'}{\rho_4} + d_n^{(2)} \frac{\left[\rho_4 j_n(\rho_4)\right]'}{\rho_4} + i h_n(\rho_4) + i d_n^{(2)} j_n(\rho_4) \right\} \bar{N}_{e1n}(k_2) \right) \tag{61}$$

for $R < b_1$, where

$$A_n^{(1)} = j_n(\rho_3) + a_n^{(1)} h_n(\rho_3) \tag{62}$$

$$B_n^{(1)} = \frac{\left[\rho_3 j_n(\rho_3)\right]'}{\rho_3} + b_n^{(1)} \frac{\left[\rho_3 h_n(\rho_3)\right]'}{\rho_3} \tag{63}$$

$$C_n^{(1)} = ij_n(\rho_3) + ib_n^{(1)} h_n(\rho_3) \tag{64}$$

$$D_n^{(1)} = -i \frac{\left[\rho_3 j_n(\rho_3)\right]'}{\rho_3} - ia_n^{(1)} \frac{\left[\rho_3 h_n(\rho_3)\right]'}{\rho_3} \tag{65}$$

$$\rho_3 = k_1 b_1$$

and

$$A_n^{(2)} = j_n(\rho_4)\, a_n^{(2)} \sqrt{\epsilon_r} \tag{66}$$

$$B_n^{(2)} = \frac{\left[\rho_4 j_n(\rho_4)\right]'}{\rho_4} b_n^{(2)} \sqrt{\epsilon_r} \tag{67}$$

$$C_n^{(2)} = ij_n(\rho_4)\, b_n^{(2)} \sqrt{\epsilon_r} \tag{68}$$

$$D_n^{(2)} = -i \frac{\left[\rho_4 j_n(\rho_4)\right]'}{\rho_4} a_n^{(2)} \sqrt{\epsilon_r} \tag{69}$$

$$\rho_4 = k_2 b_1$$

The coefficients in equations (56) and (57) were combined into A_n, B_n, C_n, and D_n since the electric field far from the antenna is of primary interest. Here, A_n and B_n represent the field contribution from the electric current source and, similarly, C_n and D_n were derived from the magnetic current source. Again, the superscript on the coefficient denotes the source region.

For the source located on the sphere surface, these coefficients may be reduced using the relation

$$j_n(\rho)\ \left[\rho h_n(\rho)\right]' - h_n(\rho)\left[\rho j_n(\rho)\right]' = \frac{i}{\rho}$$

Hence

$$A_n^{(1)} = \frac{i}{\rho_1} \frac{j_n(\rho_2)}{\left[\rho_1 h_n(\rho_1)\right]' j_n(\rho_2) - \left[\rho_2 j_n(\rho_2)\right]' h_n(\rho_1)} = A_n^{(2)} \tag{70}$$

$$B_n^{(1)} = \frac{i}{\rho_2^2} \frac{\left[\rho_2 j_n(\rho_2)\right]'}{\epsilon_r \left[\rho_1 h_n(\rho_1)\right]' j_n(\rho_2) - \left[\rho_2 j_n(\rho_2)\right]' h_n(\rho_1)} = B_n^{(2)} \tag{71}$$

$$\frac{C_n^{(1)}}{\sqrt{\epsilon_r}} = -\frac{\epsilon_r}{\rho_2} \frac{j_n(\rho_2)}{\epsilon_r \left[\rho_1 h_n(\rho_1)\right]' j_n(\rho_2) - \left[\rho_2 j_n(\rho_2)\right]' h_n(\rho_1)} = C_n^{(2)} \tag{72}$$

$$\frac{D_n^{(1)}}{\sqrt{\epsilon_r}} = \frac{1}{\rho_1 \rho_2} \frac{\left[\rho_2 j_n(\rho_2)\right]'}{\left[\rho_1 h_n(\rho_1)\right]' j_n(\rho_2) - \left[\rho_2 j_n(\rho_2)\right]' h_n(\rho_1)} = D_n^{(2)} \tag{73}$$

In the far zone the spherical Hankel functions of the first kind may be replaced by the leading term of their asymptotic expressions. Thus

$$\left.\begin{aligned} h_n(kR) &\sim (-i)^{n+1} \frac{e^{ikR}}{kR} \\ \frac{1}{kR} \frac{\partial}{\partial R} \left[R h_n(kR)\right] &\sim (-i)^n \frac{e^{ikR}}{kR} \end{aligned}\right\} \tag{74}$$

For large values of kR the spherical wave functions become

$$\bar{M}_{\substack{e \\ 0}mn}^{(1)}(kR) \sim (-i)^{n+1} \frac{e^{ikR}}{kR} \bar{m}_{\substack{e \\ 0}mn} \tag{75}$$

$$\bar{N}_{\substack{e \\ 0}mn}^{(1)}(kR) \sim (-i)^{n} \frac{e^{ikR}}{kR} \bar{n}_{\substack{e \\ 0}mn} \tag{76}$$

where

$$\bar{m}_{\substack{e\\0}mn} = \left[\mp \frac{m}{\sin\theta} P_n^m(\cos\theta) \begin{matrix}\sin\\\cos\end{matrix} m\phi\hat{\theta} - \frac{\partial P_n^m(\cos\theta)}{\partial\theta} \begin{matrix}\cos\\\sin\end{matrix} m\phi\hat{\phi} \right] \tag{77}$$

and

$$\bar{n}_{\substack{e\\0}mn} = \left[\frac{\partial P_n^m(\cos\theta)}{\partial\theta} \begin{matrix}\cos\\\sin\end{matrix} m\phi\hat{\theta} \mp \frac{P_n^m(\cos\theta)}{\sin\theta} \begin{matrix}\sin\\\cos\end{matrix} m\phi\hat{\phi} \right] \tag{78}$$

Using these results in equations (56) and (59), the far-zone field expressions are obtained for the Huygens' source in the presence of a dielectric sphere

$$\bar{E}_H(\bar{R}) = \frac{-\omega\mu_1 C_e}{4\pi} \frac{e^{ik_1 R}}{R} \sum_{n=1}^{\infty} \frac{2n+1}{n(n+1)} (-i)^n \left(\alpha_n \bar{m}_{01n} + \beta_n \bar{n}_{e1n}\right) \tag{79}$$

where

$$\alpha_n = -i\left(A_n^{(1)} + D_n^{(1)}\right) \tag{80}$$

$$\beta_n = B_n^{(1)} + C_n^{(1)} \tag{81}$$

or

$$\alpha_n = -i\left(A_n^{(2)} + D_n^{(2)}\right) \tag{82}$$

$$\beta_n = B_n^{(2)} + C_n^{(2)} \tag{83}$$

for the source located in region I or II, respectively.

In order to recover the far-zone field expressions due to the electric or magnetic source only, $C_n = D_n = 0$ or $A_n = B_n = 0$ in equations (79) to (83).

Properties of a Huygens' Source in the Presence of a Dielectric Sphere

Radiated power.- An expression for the total radiated power W is now derived by integrating the total power flow across an infinitely large sphere, centered at the origin, using the relation

$$W = \frac{1}{2\eta_0} \int_0^{2\pi} \int_0^{\pi} \bar{E} \cdot \bar{E}^* \, R^2 \, d\Omega \tag{84}$$

where $d\Omega = \sin\theta \, d\theta \, d\phi$ and the asterisk denotes complex conjugation.

The various scalar products formed in equation (84) are now investigated. It is seen from equations (77) and (78) that each term of the product $m_{01n} \cdot n_{e1\ell}$ will contain a factor of the form

$$\frac{P_n^1(\cos\theta)}{\sin\theta} \; \frac{\partial P_\ell^1(\cos\theta)}{\partial\theta} \tag{85}$$

Using the differential relations for the associated Legendre functions (ref. 5), it is found that

$$\frac{P_n^1(\cos\theta)}{\sin\theta} \; \frac{\partial P_\ell^1(\cos\theta)}{\partial\theta} = \frac{1}{2} \left[\ell(\ell+1) \, \frac{P_n^1(\cos\theta)}{\sin\theta} \, P_\ell^0(\cos\theta) - \frac{P_n^1(\cos\theta)}{\sin\theta} \, P_\ell^2(\cos\theta) \right] \tag{86}$$

It now follows that

$$\int_0^{\pi} \frac{P_n^1(\cos\theta)}{\sin\theta} \; \frac{\partial P_\ell^1(\cos\theta)}{\partial\theta} \sin\theta \, d\theta = 0 \tag{87}$$

since

$$\int_0^{\pi} P_n^m(\cos\theta) \, P_n^k(\cos\theta) \, d\theta = 0 \qquad (m \neq k) \tag{88}$$

Thus

$$\iint \bar{m}_{01n} \cdot \bar{n}_{e1\ell} \, d\Omega = 0 \tag{89}$$

Also, performing the integration results in

$$\iint \bar{m}_{01n} \cdot \bar{m}_{01\ell} \, d\Omega = \iint \bar{n}_{e1n} \cdot \bar{n}_{e1\ell} \, d\Omega = \frac{2\pi n^2 (n+1)^2}{2n+1} \, \delta_{n\ell} \tag{90}$$

where

$$\delta_{n\ell} = \begin{cases} 0 & (n \neq \ell) \\ 1 & (n = \ell) \end{cases} \tag{91}$$

and where the formula (Stratton, ref. 5)

$$\int_0^{\pi} \left(\frac{dP_n^m}{d\theta} \frac{dP_\ell^m}{d\theta} + m^2 \frac{P_n^m P_\ell^m}{\sin^2 \theta} \right) \sin \theta \, d\theta = \frac{2n(n+1)\,(n+m)!}{2n+1\,(n-m)!} \, \delta_{n\ell} \tag{92}$$

has been used. Inserting equation (79) into equation (84) and evaluating the integrals gives the desired relation for the radiated power as follows:

$$W = \frac{15}{2} \, k_1^2 C_e^2 \sum_{n=1}^{\infty} (2n+1) \, (\alpha_n \alpha_n^* + \beta_n \beta_n^*) \tag{93}$$

where $\eta_0 = 120\pi$ ohms.

Radiation resistance.- Suppose that instead of having an infinitesimal point source, the electric current element were of a short length ℓ with a constant magnitude I_0. Then $C_e = I_0 \ell$, and the radiation resistance for this system is easily obtained.

The radiation resistance of an antenna is defined as

$$R_r = \frac{2W}{|I_0|^2} \tag{94}$$

That is, assuming no losses, a current element with an rms value of I_0 flowing on an antenna with a radiation resistance R_r, will radiate an average power W. In order to determine the radiation resistance of the source in the presence of the dielectric sphere, equation (93) is substituted into equation (94). Hence

$$R_r = 15(k_1 \ell)^2 \sum_{n=1}^{\infty} (2n + 1) (\alpha_n \alpha_n^* + \beta_n \beta_n^*) \tag{95}$$

Directivity.- The directivity in the forward direction relative to an isotropic source is defined by

$$D_0 = \frac{4\pi \text{ (Radiation intensity in } \theta = 180^\circ \text{ direction)}}{\text{Total power radiated}} \tag{96}$$

since for the sphere concentric with the origin, and the source located on the +z-axis, the relative field intensity in the $-\hat{z}$ ($\theta = 180^\circ$) direction is of primary interest.

From equations (77) and (78), it is evident that

$$\bar{m}_{01n}\Big|_{\substack{\theta=\pi \\ \phi=0}} = (-1)^{n+1} \frac{n(n+1)}{2} \hat{\theta} \tag{97}$$

and

$$\bar{n}_{01n}\Big|_{\substack{\theta=\pi \\ \phi=0}} = (-1)^{n} \frac{n(n+1)}{2} \hat{\theta} \tag{98}$$

since

$$\frac{P_n^1(\cos\theta)}{\sin\theta}\Bigg|_{\theta=\pi} = (-1)^{n+1} \frac{n(n+1)}{2} \tag{99}$$

and

$$\frac{\partial P_n^1(\cos\theta)}{\partial\theta}\Bigg|_{\theta=\pi} = (-1)^{n} \frac{n(n+1)}{2} \tag{100}$$

Using this result in equation (94) an expression for the radiated power intensity in the $-\hat{z}$-direction is obtained. Thus

$$\frac{R_r^2}{2\eta_0}\,\bar{E}\cdot\bar{E}^*\Big|_{\theta=\pi} = \frac{15K_1^2C_e^2}{4\pi}\left|\sum_{n=1}^{\infty}\frac{2n+1}{2}(i)^n(\alpha_n+\beta_n)\right|^2 \tag{101}$$

Combining equations (101), (93), and (96) the desired directivity formula results:

$$D_0 = \frac{\left|\sum_{n=1}^{\infty}\frac{2n+1}{2}(i)^n(\alpha_n+\beta_n)\right|^2}{\sum_{n=1}^{\infty}\frac{2n+1}{2}(\alpha_n\alpha_n^*+\beta_n\beta_n^*)} \tag{102}$$

For comparison, it will be of interest to compute the directivity of a uniformly illuminated circular aperture. The normalized field pattern of a large uniform aperture can be found by the application of Huygens' principle and is given by Kraus (ref. 6) as

$$E(\theta) = \frac{2\lambda}{\pi d}\,\frac{J_1\left(\frac{\pi d}{\lambda}\sin\theta\right)}{\sin\theta} \tag{103}$$

where $d = 2a$ is the aperture diameter. For this case, the directivity is given by

$$D_0 = \frac{|E(0)|^2}{\frac{1}{4\pi}\int|E(\theta)|^2\,d\Omega} \tag{104}$$

and hence,

$$D_0 = \frac{\pi^2 d^2}{2\lambda^2\int_0^{\pi/2}\frac{\left[J_1\left(\frac{\pi d}{\lambda}\sin\theta\right)\right]^2}{\sin\theta}\,d\theta} \tag{105}$$

Efficiency.- For a lossy dielectric, ϵ_2 is complex and may be represented by

$$\epsilon_2 = \epsilon' + i\epsilon'' \tag{106}$$

where ϵ' and ϵ'' are the real and imaginary parts of the permittivity, respectively. The conductivity σ is related to ϵ'' by

$$\sigma = \omega\epsilon'' \tag{107}$$

and the loss tangent is defined as

$$\tan \delta = \frac{\epsilon''}{\epsilon'} \tag{108}$$

Equation (106), therefore, may be cast in the form

$$\epsilon_2 = \epsilon'(1 + i \tan \delta) \tag{109}$$

The propagation constant k_2 will also be complex, being equal to

$$k_2 = k' \sqrt{1 + i \tan \delta} \tag{110}$$

Thus in the previously derived equations ϵ_2 and k_2 are simply replaced by their complex values to account for the dielectric loss.

To find the power dissipated within the sphere, the source is placed in region I close to the surface of the sphere. With $C_m = \eta_2 C_e$, the electric field within the sphere may be expressed by

$$\bar{E}_H(\bar{R}) = \frac{-k_1 \omega\mu C_e}{4\pi} \sum_{n=1}^{\infty} \frac{2n + 1}{n(n + 1)} \left[\nu \bar{M}_{01n}(k_2) + \xi \bar{N}_{e1n}(k_2)\right] \tag{111}$$

where

$$\bar{M}_{01n}(k_2) = j_n(\rho) \left[\frac{P_n^1(\cos \theta)}{\sin \theta} \cos \phi \hat{\theta} - \frac{\partial P_n^1(\cos \theta)}{\partial \theta} \sin \phi \hat{\phi}\right] \tag{112}$$

$$\bar{N}_{e1n}(k_2) = \frac{n(n+1)}{\rho} j_n(\rho)\, P_n^1(\cos\theta)\cos\phi\hat{R}$$

$$+\frac{1}{\rho}\left[\rho j_n(\rho)\right]'\left[\frac{\partial P_n^1(\cos\theta)}{\partial\theta}\cos\phi\hat{\theta} - \frac{P_n^1(\cos\theta)}{\sin\theta}\sin\phi\hat{\phi}\right] \tag{113}$$

$$\rho = k_2 R$$

$$\nu = c_n^{(1)} h_n(\rho_3) - \frac{ic_n^{(1)}}{\sqrt{\epsilon_r}}\,\frac{\left[\rho_3 h_n(\rho_3)\right]'}{\rho_3}$$

$$\xi = d_n^{(1)}\,\frac{\left[\rho_3 h_n(\rho_3)\right]'}{\rho_3} + i\,\frac{d_n^{(1)}}{\sqrt{\epsilon_r}}\,h_n(\rho_3)$$

and $c_n^{(1)}$ and $d_n^{(1)}$ are given by equations (26) and (27), respectively.

The power dissipated within a region of conductivity σ is given by the formula

$$P_D = \frac{1}{2}\iiint \sigma \bar{E}\cdot\bar{E}^*\, dV \tag{114}$$

For a homogeneous sphere of radius a this equation becomes

$$P_D = \frac{\sigma}{2}\int_0^{2\pi}\int_0^{\pi}\int_0^{a} \bar{E}(\bar{R})\cdot\bar{E}(R)^* R^2 \sin\theta\, dR\, d\theta\, d\phi \tag{115}$$

Because of the orthogonality of the associated Legendre functions and their derivatives,

$$\int_0^{\pi} \bar{M}_{01n}\cdot\bar{N}_{e1\ell}\,\sin\theta\; d\theta = 0 \tag{116}$$

Also, it is easy to show that

$$\int_0^{2\pi}\int_0^{\pi} \bar{M}_{01n}(\rho)\cdot\bar{M}^{*}_{01\ell}(\rho)\,d\Omega = 2\pi n^2\,\frac{(n+1)^2}{2n+1}\,j_n(\rho)\,j^{*}_n(\rho)\,\delta_{n\ell} \tag{117}$$

and

$$\int_0^{2\pi}\int_0^{\pi} \bar{N}_{e1n}(\rho)\cdot\bar{N}^{*}_{e1\ell}(\rho)\,d\Omega$$

$$= \frac{2\pi n^2(n+1)^2}{\rho\rho^{*}(2n+1)}\left[n(n+1)\,j_n(\rho)\,j^{*}_n(\rho) + \left[\rho j_n(\rho)\right]'\left[\rho j_n(\rho)\right]'^{*}\right]\delta_{n\ell} \tag{118}$$

where equation (92) and the formula (also given by Stratton in ref. 5)

$$\int_0^{\pi} P_n^m(\cos\theta)\,P_\ell^m(\cos\theta)\,\sin\theta\,d\theta = \frac{2}{2n+1}\,\frac{(n+m)!}{(n-m)!}\,\delta_{n\ell} \tag{119}$$

have been used. With the aid of equation (118) the θ and ϕ integrations are performed and an expression for the dielectric loss is obtained. Thus

$$P_D = \frac{\sigma k_1^2\omega^2\mu_1^2C_e^2}{16\pi}\sum_{n=1}^{\infty}(2n+1)\int_0^a\left\{\nu\nu^{*}j_n(\rho)j_n(\rho)^{*} + \frac{\xi\xi^{*}}{\rho\rho^{*}}\left[n(n+1)j_n(\rho)j^{*}_n(\rho)\right.\right.$$

$$\left.\left. + \left[\rho j_n(\rho)\right]'\left[\rho j_n(\rho)\right]'^{*}\right]\right\}R^2\,dR \tag{120}$$

or

$$P_D = \frac{15\sigma\eta_0k_1^2C_e^2}{2|\epsilon_r|}\sum_{n=1}^{\infty}(2n+1)\int_0^a\left|\nu\rho j_n(\rho)\right|^2 + n(n+1)\left|\xi j_n(\rho)\right|^2 + \left|\xi\left[\rho j_n(\rho)\right]'\right|^2 dR \tag{121}$$

Now that expressions for the dissipated power P_D (eqs. (120) and (121) and the radiated power W (eq. (93)) are available, the antenna efficiency may be computed from the relation

$$\frac{\text{Radiated power}}{\text{Total input power}} = \frac{W}{W + P_D} \tag{122}$$

NUMERICAL RESULTS

The far-zone electric fields radiated from a Huygens' source on the surface of a dielectric sphere (see eq. (79)) were numerically calculated using the computer program listed in the appendix. Since the series for the far field converges in n in a manner similar to the spherical Bessel functions, it was found that $N \geq kD + 7$ terms provided sufficient accuracy in the calculations within plotting error.

The normalized radiation patterns for various diameter spheres, computed in 1° increments, are presented in figure 38. Here the E- and H-planes correspond to the $\phi = 0$ and $\phi = \pi/2$ planes, respectively. In each case a dielectric constant of 2.57 with a loss tangent of 0.0065 was used, which is typical of Plexiglas in the frequency range of interest (ref. 7). It should be noted that with the source oriented as shown in figure 36, the maximum radiation occurs in the $-\hat{z}$-direction, and hence the top of the computed patterns correspond to $\theta = 180^{\circ}$.

In order to investigate the effect of moving the source away from the sphere, the curves of figure 39 were calculated using equation (79) in 2° intervals. Since b_1 is the distance from the origin to the source and a is the sphere radius, the ratios of b_1/a shown in figures 39(a) to (h) correspond to the source displaced 0.0, 0.25, 0.5, and 1.0 free-space wavelengths from the sphere surface. In a similar manner, the radiation patterns of figure 40 correspond to the source spaced 0.1 and 0.5 inside the sphere surface.

By increasing the dielectric constant, directive patterns can be produced for the source lying inside the dielectric sphere. Typical patterns computed for 12.70-cm spheres operating at 10 GHz are shown in figure 41.

Figure 42 shows the optimum ratio of source to sphere radius for various diameter spheres. These points were obtained by fixing the dielectric constant at 4, 6, 9, and 12, and varying the source position until the maximum directivity was found. The additional points corresponding to the source on the sphere surface were obtained by adjusting the dielectric constant. In each case a loss tangent of 0.0065 was used. For comparison, the upper curve shows the location of the geometrical optics paraxial focus.

Figure 43 shows the directivity (computed from eq. (102)) of the Huygens' source on the surface of the sphere. Again, a dielectric constant of 2.57 and loss tangent of 0.0065 have been used. For comparison, the directivity of a uniformly illuminated circular aperture (eq. (105)) is also shown. The abscissa is measured in aperture diameter or sphere diameter in free-space wavelengths. The circles and squares in the figure represent

directivities derived from measured patterns for waveguide excited Plexiglas spheres using the empirical formula

$$D_0 = \frac{K}{\theta_1 \theta_2} \tag{123}$$

where K is a constant and θ_1 and θ_2 are the half-power beamwidths in the two principal planes measured in degrees. By comparing the computed directivity with the beamwidths of the Huygens' source patterns it was found that $K = 26\ 500$ yielded an error less than 0.5 dB for sphere diameters in the range of interest. Since the measured and computed patterns have the same general shape, this value of K was used in the above formula. The roughness in the curve is caused by a resonance effect within the sphere which has been damped by the dielectric loss. Figure 44 was constructed by drawing smooth curves through maximum points on directivity curves for other dielectric constants.

The antenna efficiency, computed using equation (122), is plotted in figure 45. For this computation, the source was placed $0.01\lambda_0$ from the sphere surface to avoid the problem of infinite loss associated with a point source in contact with a lossy medium (Tai, ref. 8). The dips in the curve at the larger diameter spheres are, again, due to the damped resonances.

Figure 46 shows the radiation resistance, computed from equation (95), together with reflection coefficient curves measured for 5.08- and 7.62-cm Plexiglas spheres. It is noted that both the computed and measured curves tend to have maximums spaced about $0.25\lambda_0$ apart.

DISCUSSION

Computed results and measurements using a circular waveguide feed are presented in figure 47 for a variety of Plexiglas sphere diameters. These results provide a direct comparison of the theoretical Huygens' source model and the experimental measurements. It can be seen by inspecting figure 47 that the agreement between results is good, particularly down to the -10-dB pattern level. The theoretical patterns do, however, show sharper nulls in the main beam and stronger side lobes in the rear direction than do the measured patterns. These differences may be due to the scattering from the feed waveguide structure used in the measurements or due to the fact that the Huygens' source model does not have the same forward directivity as the open-end waveguide feed antenna. Also precise agreement may not be possible in particular cases because of the lack of knowledge as to where to place the position of the equivalent Huygens' source. For example, in the case of the AED antennas using spheres, part of the dielectric protrudes into the feed waveguide,

particularly for a circular waveguide feed using small spheres. The effects of moving the Huygens' source inside and outside the sphere are given in figures 39 and 40. Although the patterns are not given here, it has been found (ref. 3) that extending the Huygens' point source into curved-line sources, subtending about the same angle as the waveguide aperture, did not significantly alter the calculated patterns.

As noted above, the radiation patterns tend to degrade as the source is moved away from the Plexiglas sphere. A similar result was also seen in the computed patterns, for the Plexiglas dielectric constant, as the source is moved into the sphere. These results indicate, therefore, that the optimum source location for Plexiglas is near the sphere surface. As seen from the curves given in figure 42 and the patterns given in figure 41, it should be possible to produce directive patterns with a source located interior to the sphere by increasing the dielectric constant appropriately.

The directivity curve, figure 43, computed using the Huygens' source model, shows close agreement with the directivity computed from experimental measurements, and confirms that the directivity of the AED antenna is indeed greater than that of a uniformly illuminated aperture of the same cross-sectional area. However, gain measurements, which include possible losses in the dielectric material, show that such losses are significant, figure 48. Such a behavior can be inferred from the radiation-efficiency curve given in figure 45, which clearly shows a loss in gain with increased volume of dielectric material, about the order of the measured values in figure 48.

The computed antenna efficiency decreases with increased sphere size because the propagation path through the lossy dielectric material is increased. It is noted, however, that near certain frequencies the efficiency curve exhibits large changes in efficiency. Similar changes, although not as pronounced, occur in the directivity curves. These changes are caused by a resonance effect within the dielectric sphere, such resonances being damped by losses in the material. For example, consider the computed radiation patterns given in figure 49. For the lossless case at resonance, much of the energy is radiated into side and back lobes, resulting in a drop in directivity and changes in the radiation resistance. With increased loss the side and back lobes are reduced at a sacrifice in efficiency. This resonance effect becomes more pronounced with increased sphere size and dielectric constant. Further detailed discussion of the resonance effect is given in reference 3.

CONCLUDING REMARKS

The results of a study of the radiation from waveguide-excited dielectric objects have been presented. The radiation patterns measured for small Plexiglas cubes and spheres exhibit gains in excess of those which can be obtained using an optimized horn of

the same cross-sectional area. It was also noted that the depolarization with the dielectric loading was no greater than that of an open-end waveguide.

By using the model of a waveguide opening onto an infinite dielectric slab-covered ground plane, it was found that the input admittance of the aperture excited dielectric (AED) antenna could be roughly predicted.

The coupling between adjacent loaded antennas was reduced below that of the unloaded waveguide aperture. This was in agreement with near-field amplitude measurements taken around the outside of a waveguide-excited sphere, which showed that most of the energy was concentrated in the forward part of the dielectric object.

Expressions for the radiated fields and other antenna parameters were derived for the Huygens' source in the presence of a dielectric sphere, using the method of dyadic Green's functions. The calculated radiation patterns and directivity using this source model on the surface of the sphere closely corresponded to the measurements. A dielectric constant of about 3.0 tended to yield the maximum directivity for spheres greater than 2.5 wavelengths in diameter. It has been confirmed from the methods of geometrical optics (ref. 3) that this value of dielectric constant yields little phase error across an equivalent aperture plane. Desirable patterns could also be produced, with the source located inside the sphere, if the dielectric constant were increased appropriately.

Finally, it was noted that the resonance effect of the dielectric sphere became stronger with increasing dielectric constant and sphere diameter. With dielectric materials such as Plexiglas, however, the resonance does not degrade the radiation pattern, but is manifest as a decrease in the antenna efficiency. This is due to the damping effect of the dielectric loss.

Langley Research Center,
National Aeronautics and Space Administration,
Hampton, Va., September 21, 1973.

APPENDIX

COMPUTER PROGRAM

Although numerous computer programs were used throughout this research, the one of primary significance, together with the necessary subroutines, is listed in this appendix. The program was written in standard IBM FORTRAN IV for use with the G level compiler and was run on an IBM System 360/67 computer.

The MAIN program calculates and prints out the normalized far-zone radiation patterns (magnitude, phase, and intensity in dB) in the two principal planes for a Huygens' source on the surface or inside a lossy dielectric sphere. It also prints the coefficients of the functions $\bar{m}$ and $\bar{n}$ and the directivity and provides the pattern data (truncated to -40 dB) in an array suitable for plotting. This program may easily be modified to compute data for only the electric or magnetic current source or, for the case where the source lies outside the dielectric sphere, to make the appropriate changes in the coefficient formulas of lines 35 to 39.

The input parameters to the MAIN program are defined as follows:

FORTRAN parameter	Description
DIAM	Sphere diameter, λ_0
PER	Dielectric constant
TAN	Dielectric loss tangent, X1000
SP	Distance from source to sphere surface, λ_0
THINC	Increment in θ variable, degrees. (The parameter THINC should divide evenly into 180^o. If THINC = 1, for example, data are calculated from $\theta = 0^o$ to $\theta = 180^o$ in 1^o intervals.)

Subroutine ASLEG is used to generate arrays of associated Legendre functions of the first order and their derivatives. The parameters are as follows:

FORTRAN parameter	Description
NMAX	Maximum value of degree, N, desired
THINC	Increment in θ variable, degrees. (See note above.)
SLEGEN DLEGEN	Names of single-precision two-dimensional arrays in which the output functions are returned
SLEGEN(N,M)	$\frac{P_N^1(\cos M)}{\sin M}$, where M = (N - 1)THINC
DLEGEN(N,M)	$\frac{\partial P_N^1(\cos M)}{\partial M}$, where M = (N - 1)THINC

Subroutine CBESS generates arrays of spherical Bessel and Hankel functions of complex arguments and their derivatives. The parameters are as follows:

FORTRAN parameter	Description
BES DBES HANK DHANK	Names of single-precision complex arrays in which the output functions are returned
BES(N)	$j_{N-1}(X)$
DBES(N)	$\frac{\partial}{\partial X}\left[Xj_{N-1}(X)\right]$
HANK(N)	$h_{N-1}^{(1)}(X)$
DHANK(N)	$\frac{\partial}{\partial X}\left[Xh_{N-1}^{(1)}(X)\right]$
X	Double precision complex argument
NMAX	Maximum value of order (N) desired

Double precision arithmetic is used throughout these subroutines, with the final output converted to single precision.

```
                      PROGRAM ERSSHOS(INPUT,OUTPUT,TAPE5=INPUT,TAPE6=OUTPUT)
000003                DIMENSION DLEGEN(45,181),PI(181),R2(181),TH(181),PMAX(2)
000003                DOUBLE PRECISION SLEGEN(45,181)
000003                COMPLEX ANPN(181),BNPN(181),ANOPN(181),BNOPN(181),PB(181,2),Z1(45)
                     2,DB1(45),B2(45),DB2(45),B3(45),DB3(45),H1(45),DH1(45),H2(45),
                     3DH2(45),H3(45),DH3(45),AN,BN,CNA,I,AX,ANA,BNA,SER,CER,DI
000003                COMPLEX R01,R02,R03
000003              1 READ 500,DIAM,PER,TAM,SP,THINC
000021                IF(EOF,5)305,315
000024            315 L=2
000025                X=.0001*TAN
000027                PI=3.14159265358979
000031                CONV=180./PI
000032                I=(0.,1.)
000035                TA=180./THINC+1
000041                CER=PER*(1.+I*X)
000054                SER=CSQRT(CER)
000057                R01=DIAM*PI
000062                R1=R01
000064                R02=R1*R01
000072                R00=R02
000074                R03=(DIAM-2.*SP)*PI*SER
                C     R01=K1A,R02=K2A,R03=K2R
000105                NMAX=2.*R01+6.5
000114                NSUM=NMAX+1
000116                CALL ASLEG(NSUM,THINC,SLEGEN,DLEGEN)
000121                CALL CBESS(B1,DB1,H1,DH1,R01,NMAX)
000125                CALL CBESS(B2,DB2,H2,DH2,R02,NMAX)
000131                CALL CBESS(B3,DB3,H3,DH3,R03,NMAX)
000135                SUM=0.
000136                DO 20 J=1,MA
000140                ANPN(J)=0
000142                BNPN(J)=0
000144                ANOPN(J)=0
000146                BNOPN(J)=0
000150             20 CONTINUE
000152                GTN= 200
000156                DO 25 N=1,NMAX
000160                M=N+1
000162                ANA=-I/(R02*(H1(M)*DH2(M)-DH1(M)*H2(M)))
000216                BNA=-I/(R02*(H1(M)*DH2(M)/SER-SER*DH1(M)*H2(M)))
000261                CNA=R3(M)-1*DB3(M)/R03
```

```
00 277          BN=-BNA*CNA
00 305          AN=ANA*CNA
                C  AN AND BN ARE THE COEFFICIENTS OF THE M AND N FUNCTIONS.
00 313       21 CONTINUE
00 313          PRINT 198,AN,BN
00 323          Y=
00 325          AY=((2.*Y+1.)/(Y*(Y+1.)))*(0.-I)**Y
00 347          BY=(2*Y+1.)/2.
00 353          SDAN=SDAN+BY*((ABS(AN)**2+CABS(BN)**2)
                C  SDAN IS THE DENOMINATOR OF THE DIRECTIVITY EXPRESSION
00 363          DO 22 L=1,MA
00 364          ANPN(L)=ANPN(L)+AY*SLEGEN(N,L)*AN
00 402          BNPN(L)=BNPN(L)+AY*SLEGEN(N,L)*BN
00 421          ANDPN(L)=ANDPN(L)+AY*DLEGEN(N,L)*AN
00 436          BNDPN(L)=BNDPN(L)+AY*DLEGEN(N,L)*BN
00 453       22 CONTINUE
00 457          DO 25 K=1,2
00 461       25 EHMAX(K)=0
00 464          DO 50 L=1,MA
00 465          EH(L,1)=ANPN(L)+BNDPN(L)
00 474          EH(L,2)=-ANDPN(L)-BNPN(L)
00 503          DO 50 K=1,2
00 504       40 EHMAX(K)=AMAX1(EHMAX(K),CABS(EH(L,K)))
00 516       50 CONTINUE
00 522          DI=10.*ALOG10((CABS(EH(MA,1))**2)/SDAN)
00 532          DO 55 K=1,2
00 533          DO 55 L=1,MA
00 534       55 EH(L,K)=EH(L,K)/EHMAX(K)
00 552          PRINT 302,DIAM,FER,R,RDO,N,X
00 571          PRINT 305
00 575          PRINT 303,SP
00 603          PRINT 304,FREQ
00 613          DO 75 L=1,MA
00 615          ANGLE=(L-1)*THINC
00 621          THT(L)=ANGLE
00 622          AMAG1=CABS(EH(L,1))
00 625          AMAG2=CABS(EH(L,2))
00 630          ANG1=ATAN2(AIMAG(EH(L,1)),REAL(EH(L,1)))*CONV
00 642          ANG2=ATAN2(AIMAG(EH(L,2)),REAL(EH(L,2)))*CONV
00 654          R1(L)=20.*ALOG10(AMAG1)
00 660          R2(L)=20.*ALOG10(AMAG2)
00 664          PRINT 310,ANGLE,AMAG1,ANG1,R1(L),ANGLE,AMAG2,ANG2,R2(L)
00 707          IF(R1(L).LT.-40.) R1(L)=-40.
```

```
00 713          IF(P2(L).LT.-40.) P2(L)=-40.
00 717       75 CONTINUE
00 722       77 POINT 213,EHMAX(1),EHMAX(2)
00 732      100 CONTINUE
00 732          WRITE(10,114) MA,(R1(L),P2(L),L=1,MA)
             C  THIS STATEMENT PRINTS ON DEVICE 10 THE NUMBER OF POINTS TO BE
             C  PLOTTED AND THEN THE E- AND H- PLANE INTENSITY ARRAYS.
00 751          GO TO 1
00 752      114 FORMAT(I4,(13F10.4))
00 752      302 FORMAT(*1*,21X,*NORMALIZED FAR ZONE ELECTRIC FIELD FROM SOURCE LOC
                 'ATED ON SURFACE OF DIELECTRIC SPHERE*/*-----  SOURCE: HUYGEN
                 '          DIAMETER IN WAVELENGTHS: *,F6.3,5X,*DIELECTRIC CONSTANT: *
                3,F6.3/52X,*AT  FA: *,F6.3,11X,*DIELECTRIC K : *,F6.3/
                4                  2X,*NUMBER OF TERMS USED IN SERIES: *,I2,19X
                .*LOSS TAN: *,F6.6)
00 752      303 FORMAT(17X,*SOURCE DISTANCE FROM SPHERE IN WAVELENGTHS: *,F7.4)
00 752      305 FORMAT(52X,*SOURCE INSIDE SPHERE SURFACE*)
00 752      304 FORMAT(                //, 6X,*PHI:   DEGREES     *,46X,*PHI: 90 DEGREES
                5     DIRECTIVITY: *,F6.3,* DB*/*          THETA      ELECTRIC FIELD
                7 INTENSITY          *, 6X,*THETA      ELECTRIC FIELD      INTENSITY
                          */*     (DEGREES)  MAGNITUDE   ANGLE          (DB)
                G*,12X,*DEGREES)  MAGNITUDE   ANGLE *,7X,*(DB)                *,3X,I2)
00 752      310 F  MAT(5X,2(F7.2,2X,F10.4,1X,F7.2,3X,F9.3,24X))
00 752      198 FORMAT(10X,2E12.4,5X,2E12.4,5X,2E12.4,5X,2E12.4)
00 752      200 FORMAT(*0*,14X,*R COEFFICIENT*,14X,*N COEFFICIENT*,/15X,*REAL*,6X,*
                 I*IMAGINARY*,1 X,*REAL*,6X,*IMAGINARY*)
00 752      213 FORMAT(*0NORMALIZATION CONSTANT: *,E12.4,35X,*NORMALIZATION CONSTA
                 'T: *,E12.4)
00 752      500 FORMAT(5E10.3,I1)
00 752      300 STOP
00 754          E
```

```
                      SUBROUTINE ASLEG(NMAX,THINC,SLEGEN,DLEGEN)
                C
000007                DIMENSION DLEGEN(45,181)
000007                DOUBLE PRECISION SLEGEN(45,181),X,TH,RAD,CONV,PI
000007                MMAX=180./THINC
000011                MA=MMAX+1.
000015                PI=3.14159265358979
000017                CONV=PI/180.
000031                RAD=THINC*CONV
000037                DO 10 N=1,NMAX
000040                A=N-1
000041                SLEGEN(N,1)=A*(A+1.)/2.
000046                DLEGEN(N,1)=SLEGEN(N,1)
000051                DLEGEN(N,MA)=A*(A+1.)/2.*(-1)**N
000065                SLEGEN(N,MA)=-DLEGEN(N,MA)
000076             10 CONTINUE
000100                DO 20 M=2,MMAX
000101                L=M-1
000103                TH=L*RAD
000111                X=DCOS(TH)
000113                SLEGEN(1,M)=1.
000123                DLEGEN(1,M)=X
000130                SLEGEN(2,M)=1.5*DSIN(2.*TH)/DSIN(TH)
000171                DLEGEN(2,M)=3.*DCOS(2.*TH)
000214                DO 20 N=3,NMAX
000215                SLEGEN(N,M)=((2.*N-1)**SLEGEN(N-1,M)-N*SLEGEN(N-2,M))/(N-1)
000266                DLEGEN(N,M)=N*X*SLEGEN(N,M)-(N+1)*SLEGEN(N-1,M)
000316             20 CONTINUE
000322                RETURN
000323                END
```

```
      SUBROUTINE CBESS(BES,DBES,HANK,DHANK,X,MAX)
C
C     INDEX IS ONE GREATER THAN ORDER OF THE FUNCTION
000011      COMPLEX BES(1),DBES(1),HANK(1),DHANK(1),I
000011      COMPLEX X,J0,J(97),P,Y(7)
000011      I=(0.,1.)
000013      NN=N+AX+15
000014      N0=NN-1
000016      NP=NN-2
000020      N0=N+AX+1
000021      N =N+AX+2
000022      J(NN)=(0.,0.)
000025      J(N0)=(1.,1.)
000032      J0=CSIN(X)/X
000047      Y(1)=-CCOS(X)/X
000064      Y(2)=Y(1)/X-J0
000075      DO 10 I=1,NP
000076      N=N0-I
000077   10 J(N)=(2*(N-1)+3)*J(N+1)/X-J(N+2)
000125      DO 12 N=3,NP
000126   12 Y(N)=((2*(N-1)-1)/X)*Y(N-1)-Y(N-2)
000156      P=J0/J(1)
000166      BES(1)=J(1)*P
000174      HANK(1)=BES(1)+I*Y(1)
000205      DO 20 L=1,N0
000207      K=L+1
000210      BES(K)=J(K)*P
000221      HANK(K)=BES(K)+I*Y(K)
000235      DBES(L)=L*BES(L)-X*BES(K)
000254   20 DHANK(L)=L*HANK(L)-X*HANK(K)
000275      RETURN
000276      END
```

REFERENCES

1. Bailey, Marion C.; and Swift, Calvin T.: Input Admittance of a Circular Waveguide Aperture Covered by a Dielectric Slab. IEEE Trans. Antennas & Propagation, vol. AP-16, no. 4, July 1968, pp. 386-391.

2. Rudge, A. W.: An Electromagnetic Radiation Probe for Near-Field Measurements at Microwave Frequencies. J. Microwave Power, vol. 5, Nov. 1970, pp. 155-174.

3. Mason, V. Bradford: The Electromagnetic Radiation From Simple Sources in the Presence of a Homogeneous Dielectric Sphere. NASA CR-2211, 1973.

4. Tai, Chen-To: Dyadic Green's Functions in Electromagnetic Theory. Intext Educational Publ., c.1971.

5. Stratton, Julius Adams: Electromagnetic Theory. McGraw-Hill Book Co., Inc., 1941.

6. Kraus, John D.: Antennas. McGraw-Hill Book Co., Inc., 1950.

7. Von Hippel, Arthur R., ed.: Dielectric Materials and Applications. M.I.T. Press, c.1954.

8. Tai, C-T.: Radiation of a Hertzian Dipole Immersed in a Dissipative Medium. TR-21, Cruft Lab., Harvard Univ., Oct. 10, 1947.

TABLE 1.- MEASURED GAIN OF AED ANTENNAS USING CIRCULAR OR SQUARE WAVEGUIDE FEED

Size and shape of dielectric object	Gain, dB, using circular waveguide measured at –			Gain, dB, using square waveguide at f = 10.0 GHz
	5.4 GHz	5.5 GHz	5.6 GHz	
Open-end waveguide	9.45	9.12	8.33	10.00
5.08-cm cube	12.70	12.95	12.54	13.82
5.08-cm sphere	10.32	10.75	9.92	13.36
7.62-cm sphere	13.05	13.20	13.00	17.40
10.16-cm sphere	17.26	17.02	16.45	19.72

TABLE 2.- MEASURED VSWR OF A CIRCULAR WAVEGUIDE, 5.08-cm SPHERE

Frequency, GHz	Open-end waveguide	Without taper	VSWR for –		
			Taper (a)	Taper (b)	Taper (c)
5.0	1.95	2.40	1.26	1.68	1.70
5.2	1.55	2.50	1.68	1.08	1.17
5.4	1.08	2.40	1.32	1.40	1.45
5.6	1.20	2.42	1.13	1.08	1.01
5.8	1.13	2.40	1.16	1.02	1.21
6.0	1.52	2.20	1.63	1.50	1.53

TABLE 3.- COUPLING OF PLEXIGLAS-LOADED CIRCULAR WAVEGUIDE ANTENNAS AS A FUNCTION OF FREQUENCY

Center-to-center spacing, cm	Frequency, GHz	Coupling, dB, in H-plane of –				Coupling, dB, in E-plane of –			
		Open-end waveguide	5.08-cm cube	5.08-cm sphere	7.62-cm sphere	Open-end waveguide	5.08-cm cube	5.08-cm sphere	7.62-cm sphere
6.35	5.2	32.7	43.9	28.3		26.0	45.9	43.7	
	5.4	33.9	34.5	32.2		26.2	47.8	48.2	
	5.6	34.7	27.1	34.1		26.6	41.6	47.5	
	5.8	35.8	29.4	37.3		28.1	40.7	45.2	
	6.0	36.5	32.9	42.8		29.7	42.4	44.2	
8.89	5.2	38.8	49.4	34.8	28.1	27.5	44.9	41.4	42.2
	5.4	39.3	52.1	38.8	33.2	28.9	41.3	45.6	45.9
	5.6	40.1	48.1	40.1	33.4	29.2	36.1	48.7	48.3
	5.8	41.8	45.4	44.0	34.5	30.7	35.9	48.9	44.2
	6.0	43.1	46.1	50.0	36.2	32.2	50.3	52.8	42.3
12.7	5.2	46.4	58.0	42.8	40.3	31.2	48.8	42.8	44.8
	5.4	48.1	55.2	47.2	48.4	32.1	46.4	45.7	45.6
	5.6	48.0	57.2	49.9	60.1	32.2	41.8	47.3	41.4
	5.8	48.2	55.4	53.3	52.4	33.8	41.2	50.9	41.4
	6.0	48.4	50.5	51.9	44.4	35.3	44.1	61.8	45.5
17.78	5.2	49.7	57.5	49.7	38.3	33.9	53.2	43.7	47.1
	5.4	49.9	57.9	53.9	46.5	35.3	53.6	46.4	45.9
	5.6	51.4	52.4	55.5	48.3	35.7	48.4	48.0	41.3
	5.8	52.7	54.9	57.9	51.5	37.3	47.2	50.1	39.5
	6.0	54.9	55.7	59.3	52.3	38.6	47.9	55.1	43.1

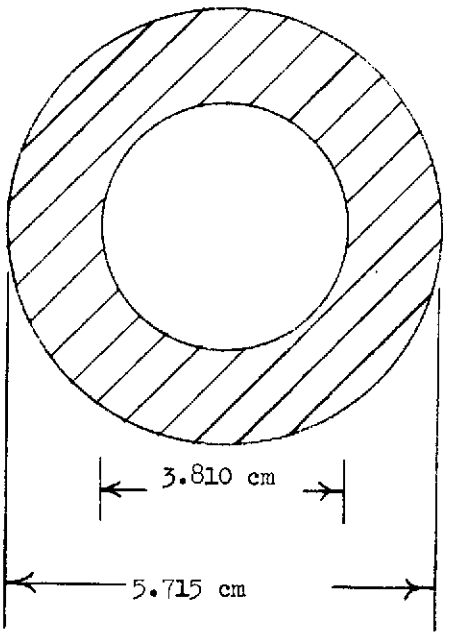

(a) Circular waveguide.

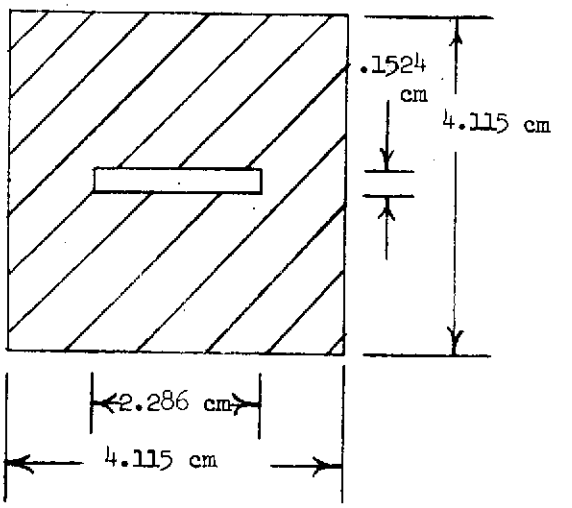

(b) Rectangular waveguide fed slot.

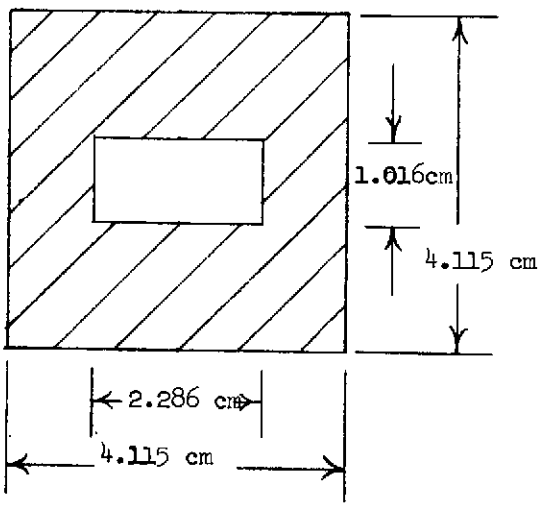

(c) Rectangular waveguide.

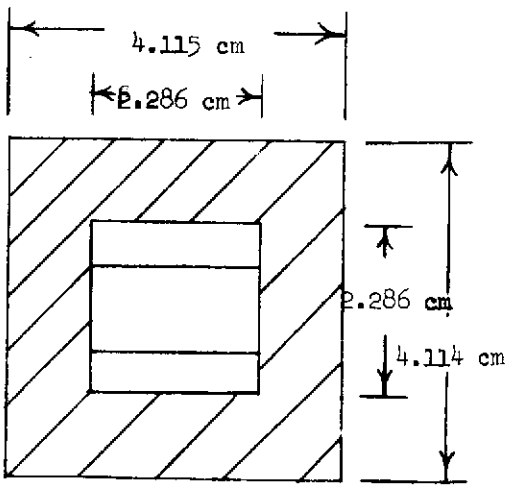

(d) Rectangular waveguide fed square horn.

Figure 1.- Sketch of the aperture and flange dimensions of the waveguide feeds.

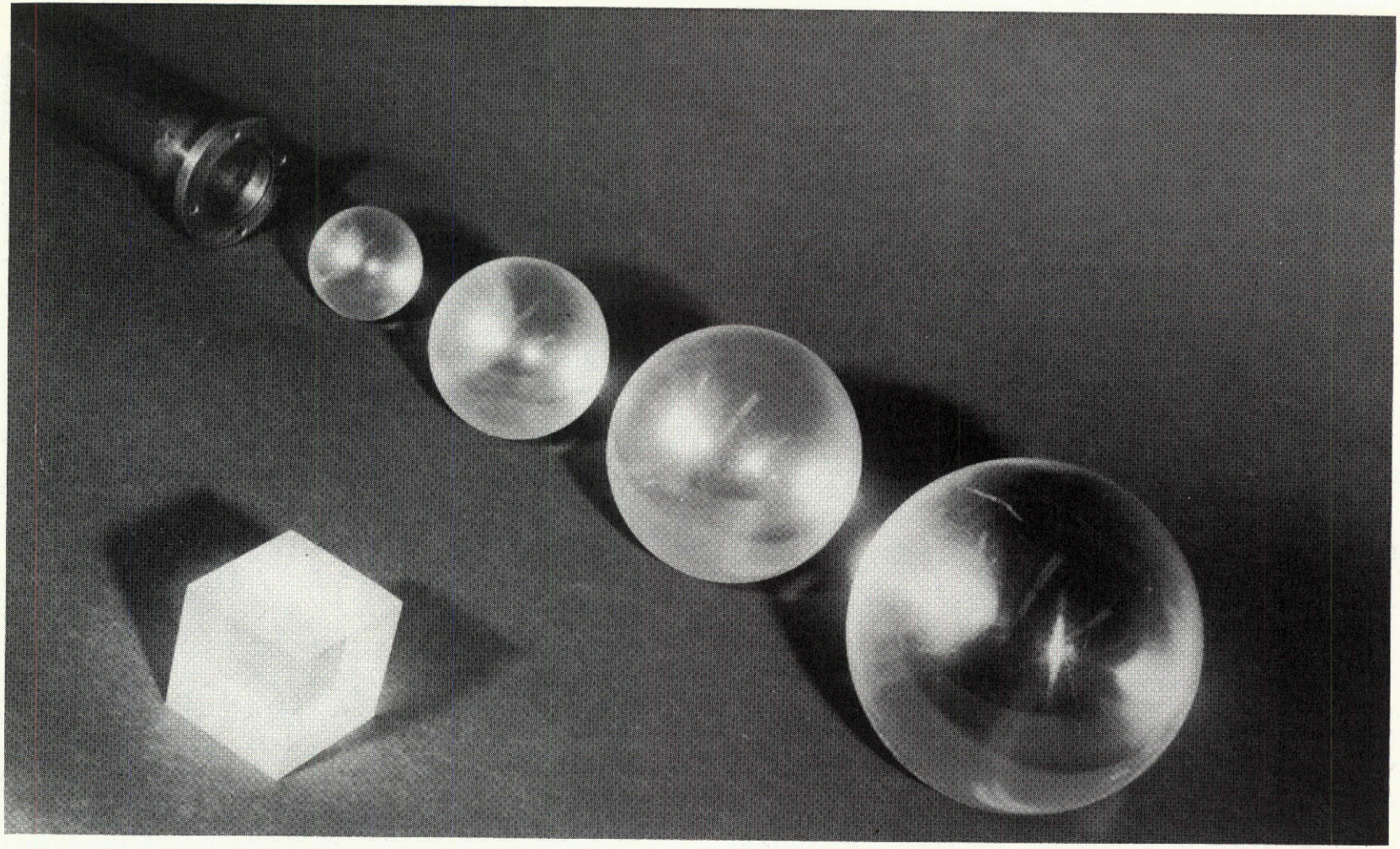

L-73-3800

Figure 2.- Photograph of the circular waveguide feed with Plexiglas objects.

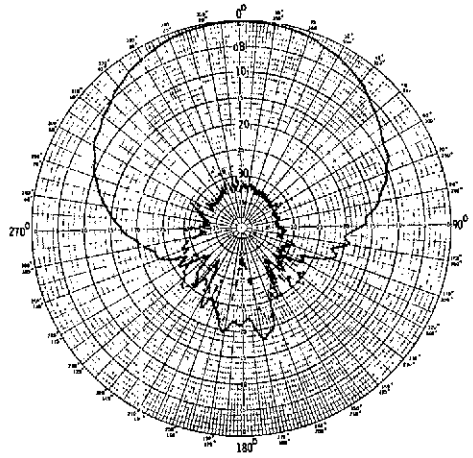

(a) Open-end waveguide (cross-polarized pattern is dashed).

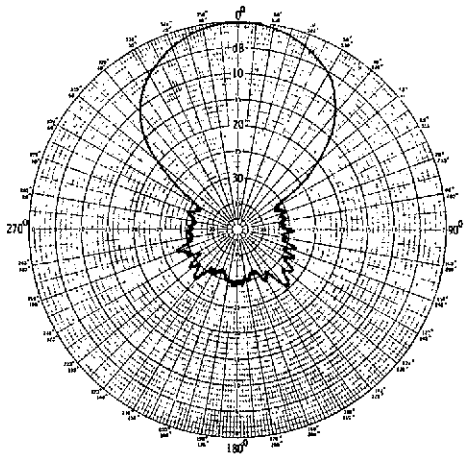

(b) 5.08-cm cube.

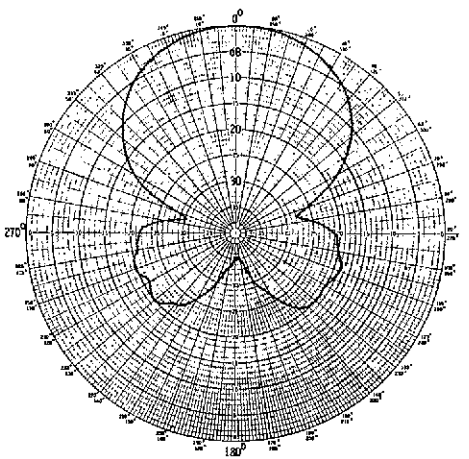

(c) 5.08-cm sphere.

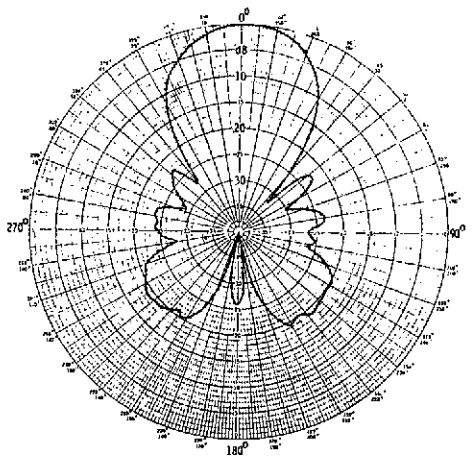

(d) 7.62-cm sphere.

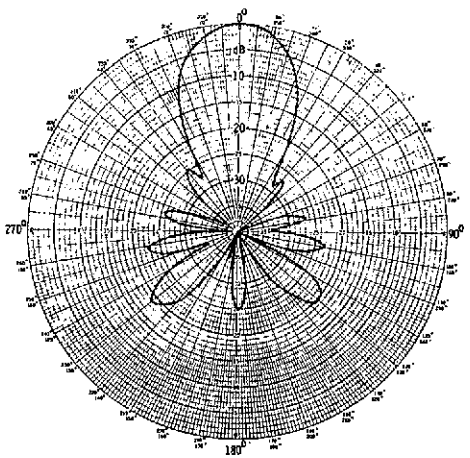

(e) 12.70-cm sphere.

Figure 3.- Radiation patterns of AED antennas in the E-plane for a circular waveguide feed at 5.0 GHz.

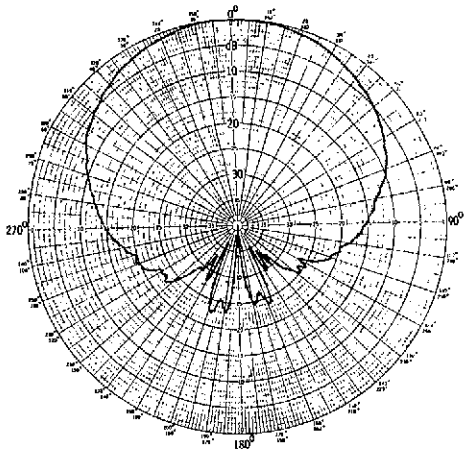

(a) Open-end waveguide.

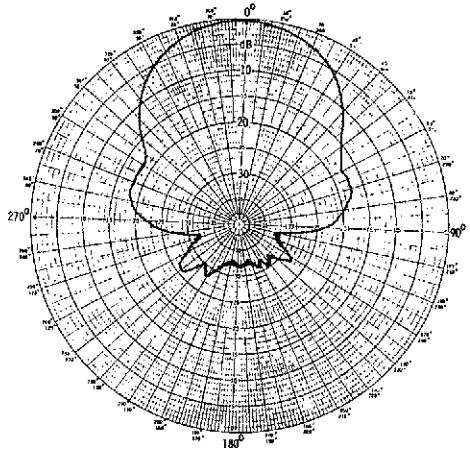

(b) 5.08-cm cube.

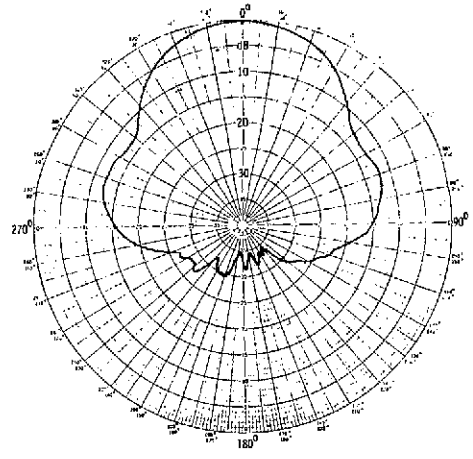

(c) 5.08-cm sphere.

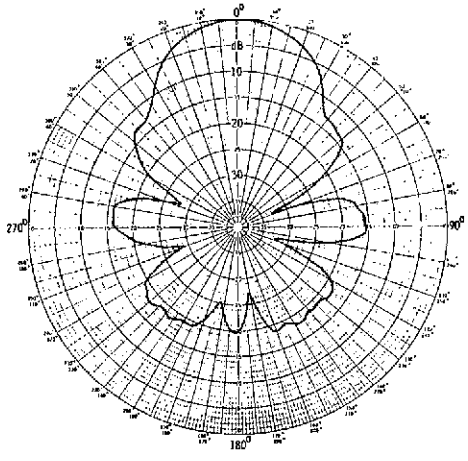

(d) 7.62-cm sphere.

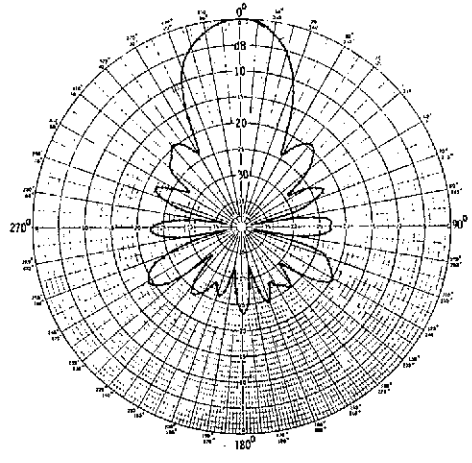

(e) 12.70-cm sphere.

Figure 4.- Radiation patterns of AED antennas in the H-plane for a circular waveguide feed at 5.0 GHz.

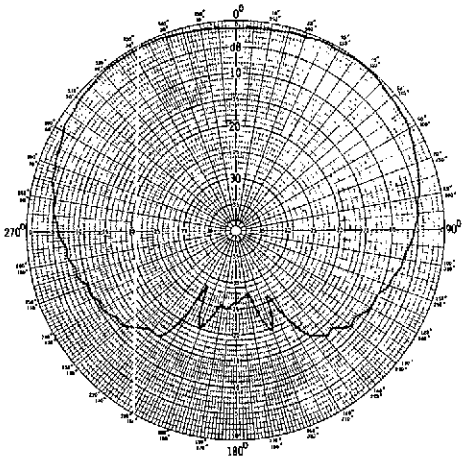

(a) Open slot.

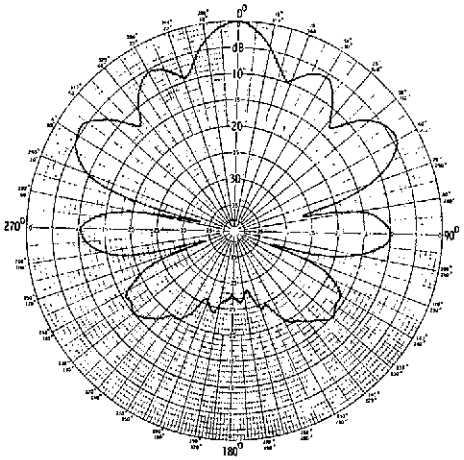

(b) 5.08-cm cube.

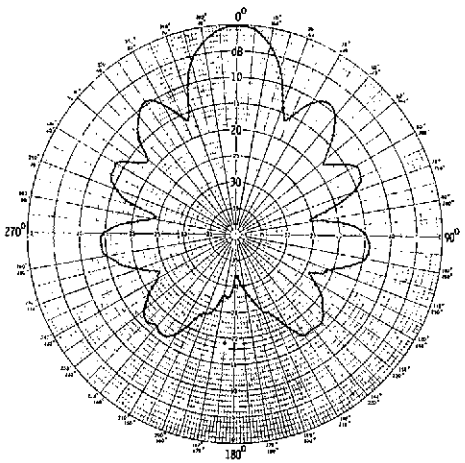

(c) 5.08-cm sphere.

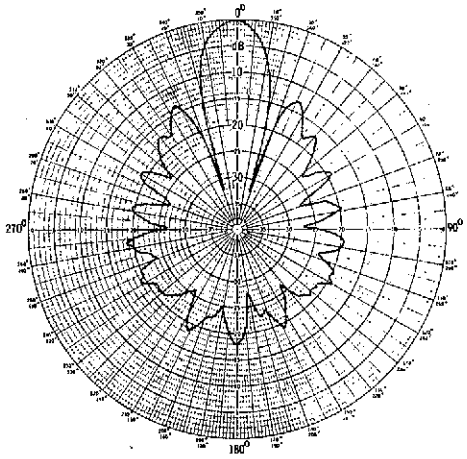

(d) 7.62-cm sphere.

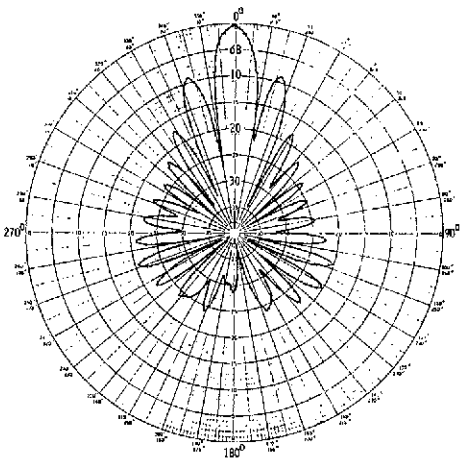

(e) 12.70-cm sphere.

Figure 5.- Radiation patterns for AED antennas in the E-plane for a slot feed at 10.0 GHz.

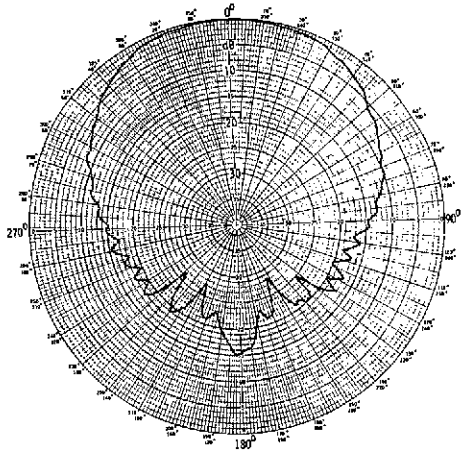

(a) Open slot.

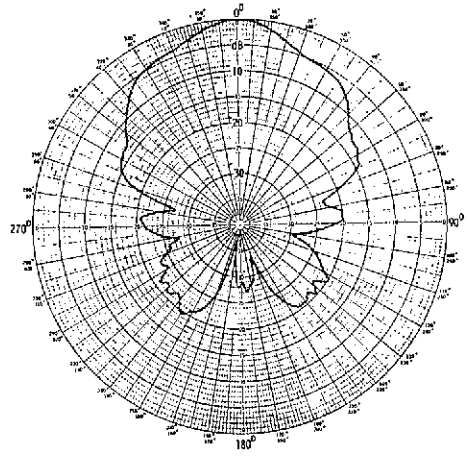

(b) 5.08-cm cube.

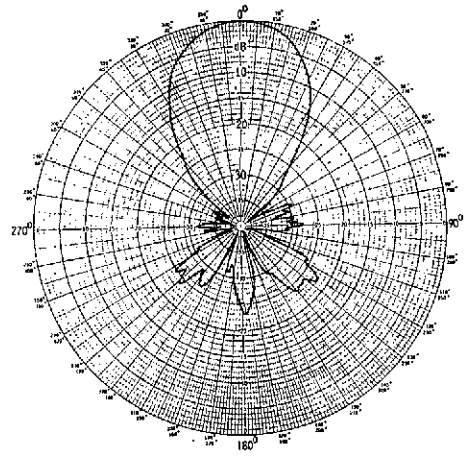

(c) 5.08-cm sphere.

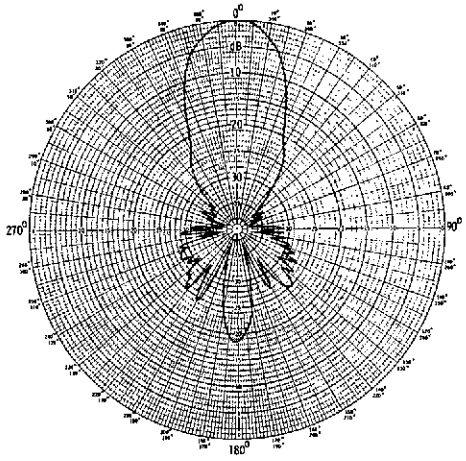

(d) 7.62-cm sphere.

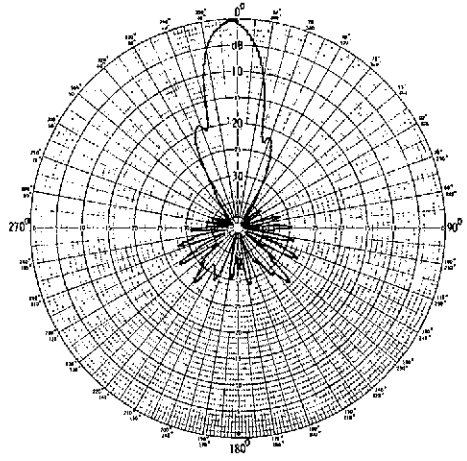

(e) 12.70-cm sphere.

Figure 6.- Radiation pattern for AED antennas in the H-plane for a slot feed at 10.0 GHz.

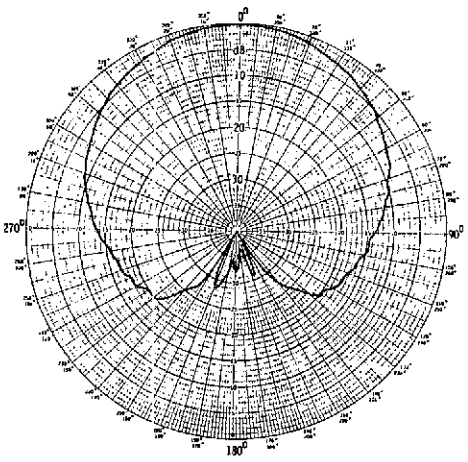

(a) Open end.

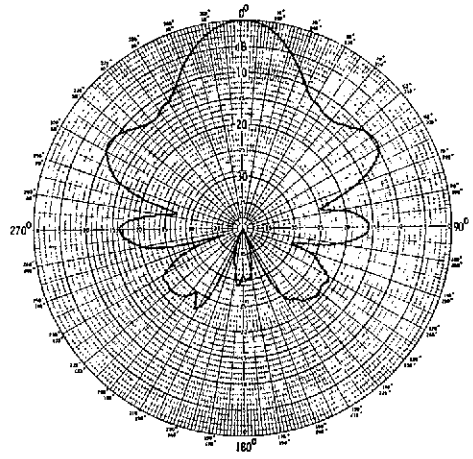

(b) 5.08-cm cube.

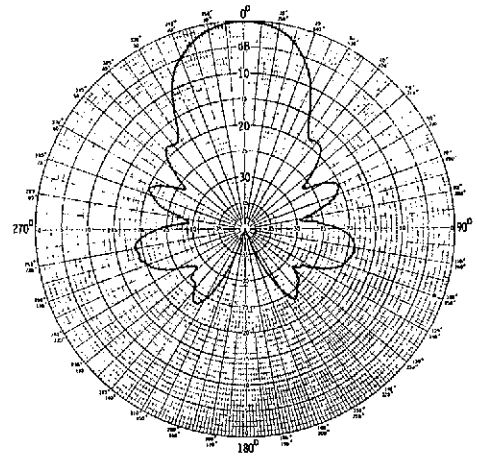

(c) 5.08-cm sphere.

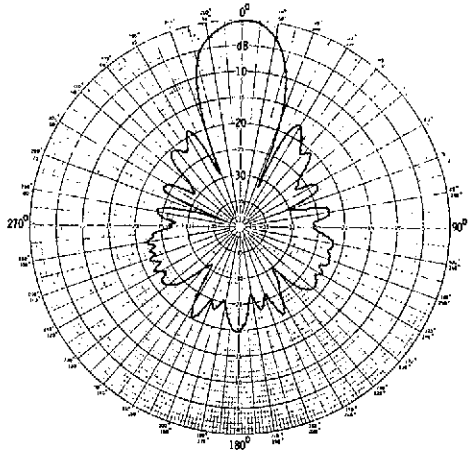

(d) 7.62-cm sphere.

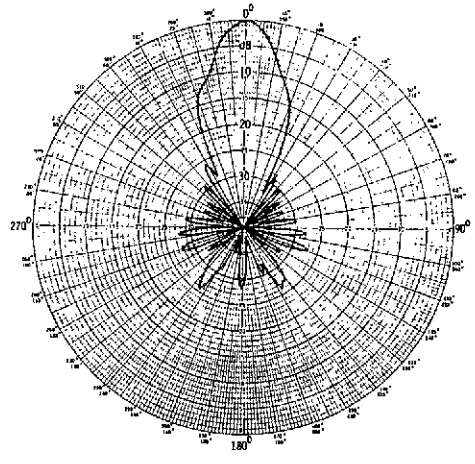

(e) 12.70-cm sphere.

Figure 7.- Radiation patterns for AED antennas in the E-plane for a rectangular waveguide feed at 10.0 GHz.

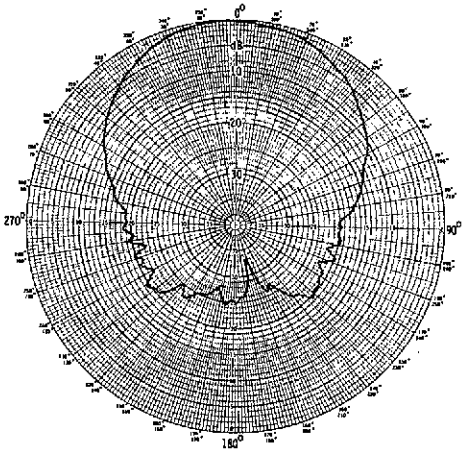

(a) Open end.

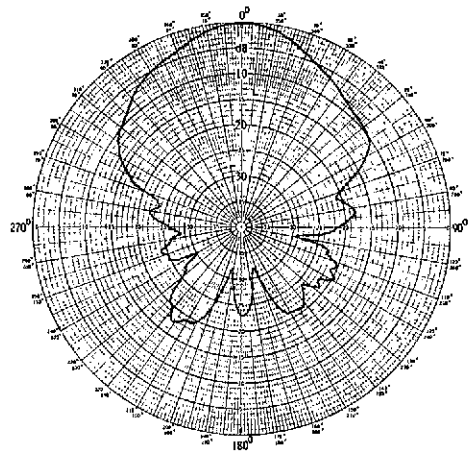

(b) 5.08-cm cube.

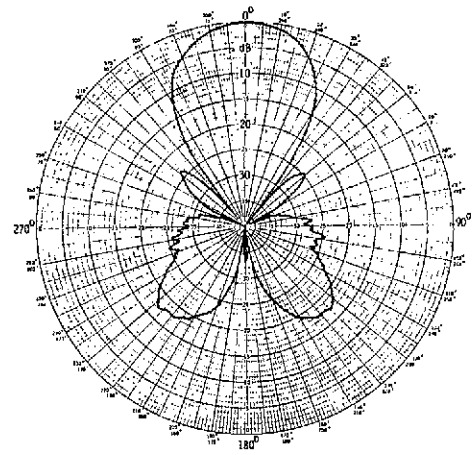

(c) 5.08-cm sphere.

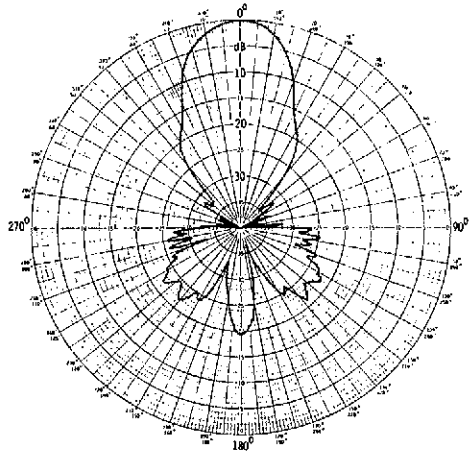

(d) 7.62-cm sphere.

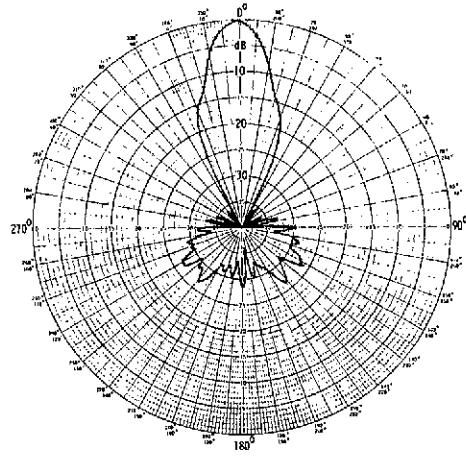

(e) 12.70-cm sphere.

Figure 8.- Radiation patterns for AED antennas in the H-plane for a rectangular waveguide feed at 10.0 GHz.

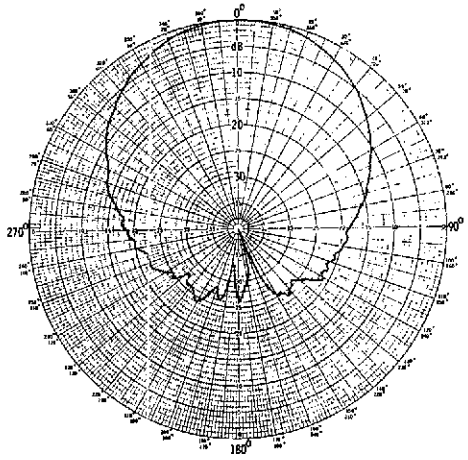

(a) Open end.

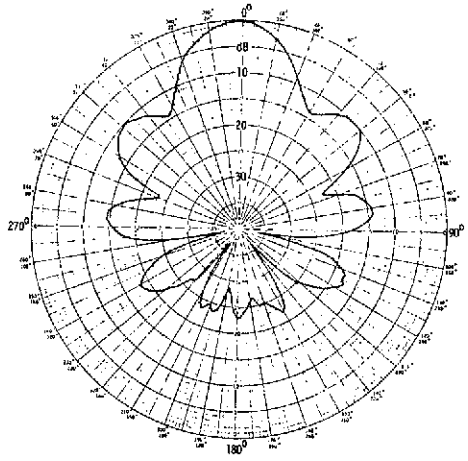

(b) 5.08-cm cube.

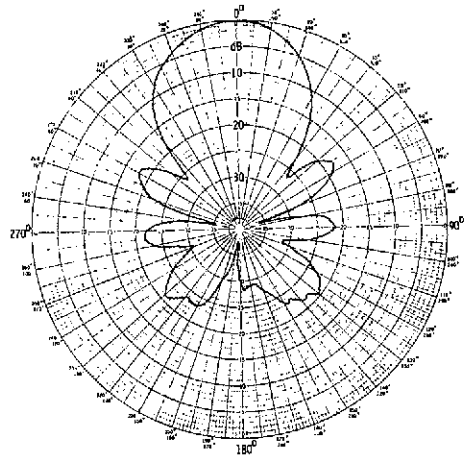

(c) 5.08-cm sphere.

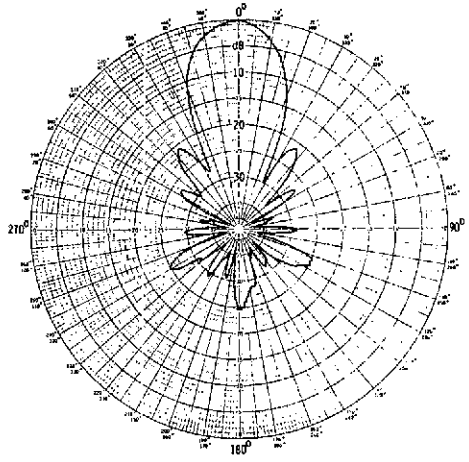

(d) 7.62-cm sphere.

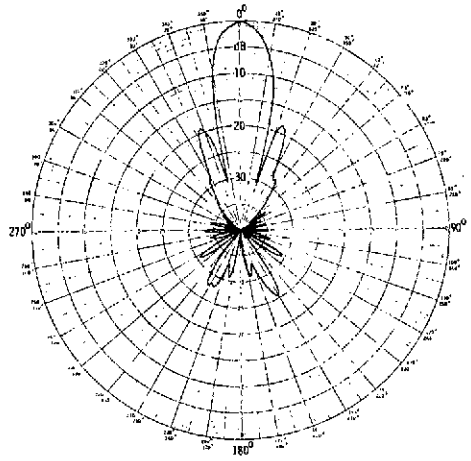

(e) 12.70-cm sphere.

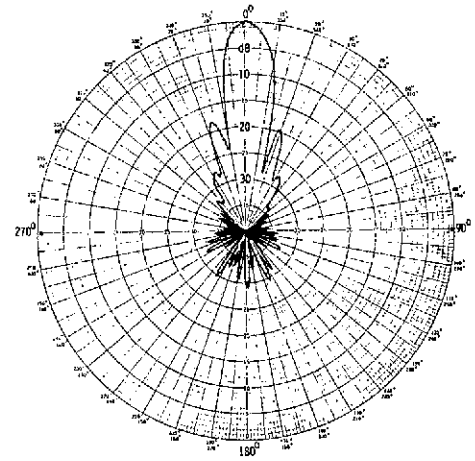

(f) 15.24-cm sphere.

Figure 9.- Radiation patterns for AED antennas in the E-plane for a square-horn waveguide feed at 10.0 GHz.

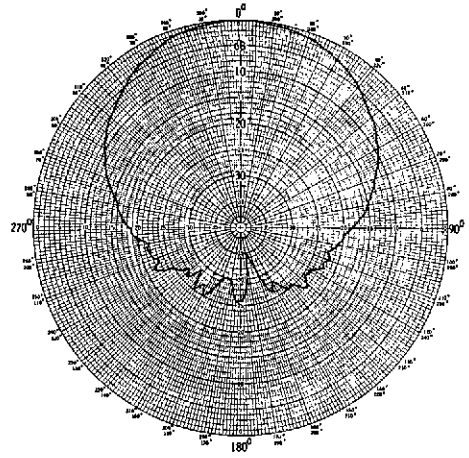

(a) Open end.

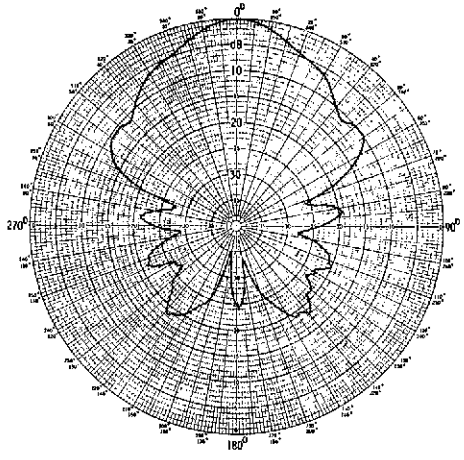

(b) 5.08-cm cube.

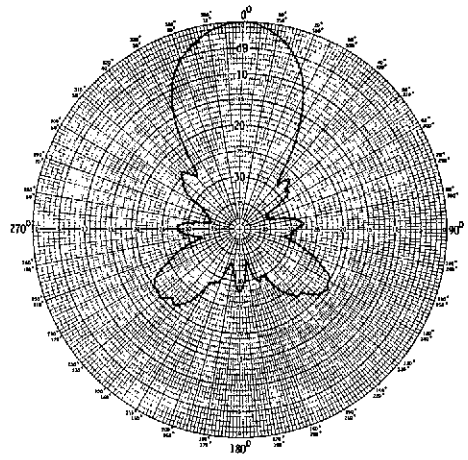

(c) 5.08-cm sphere.

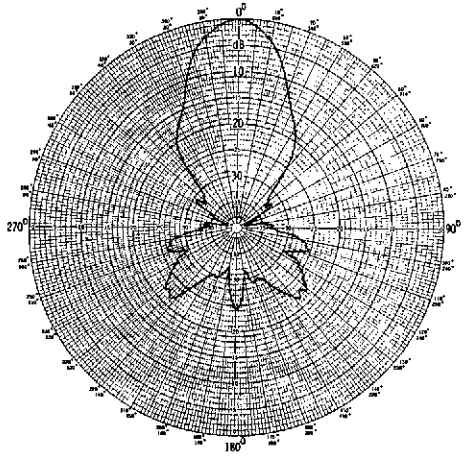

(d) 7.62-cm sphere.

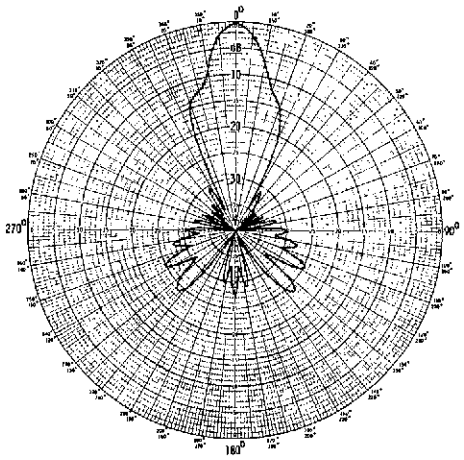

(e) 12.70-cm sphere.

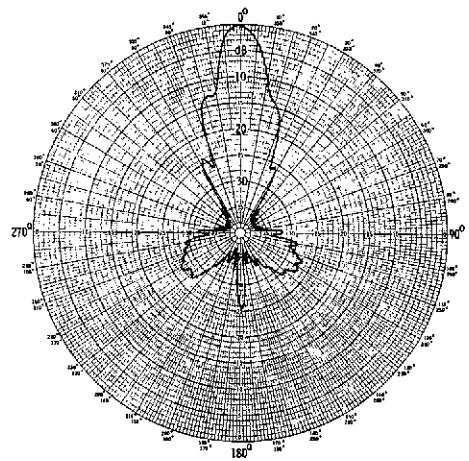

(f) 15.24-cm sphere.

Figure 10.- Radiation patterns for AED antennas in the H-plane for a square-horn waveguide feed at 10.0 GHz.

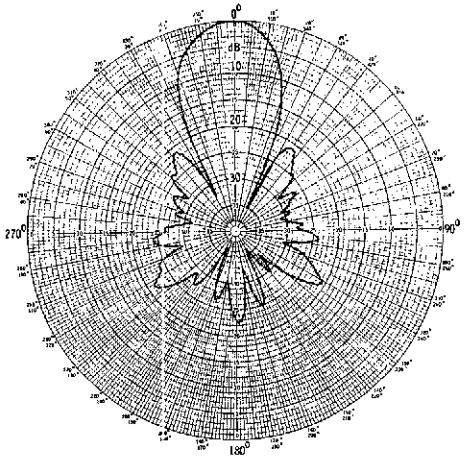

(a) E-plane; 0.0-cm spacing.

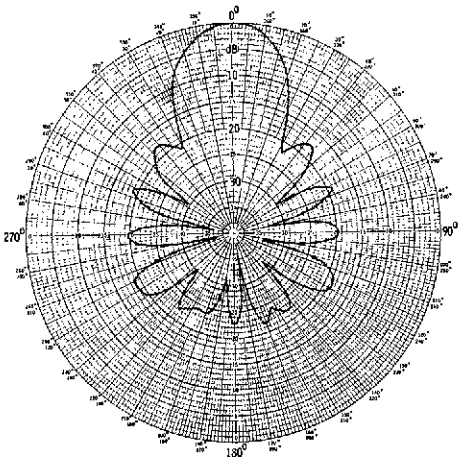

(b) E-plane; 0.635-cm spacing.

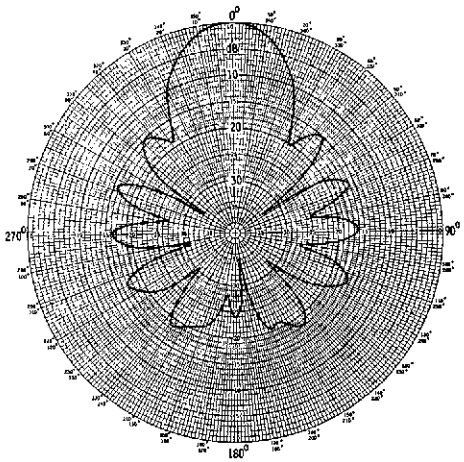

(c) E-plane; 1.27-cm spacing.

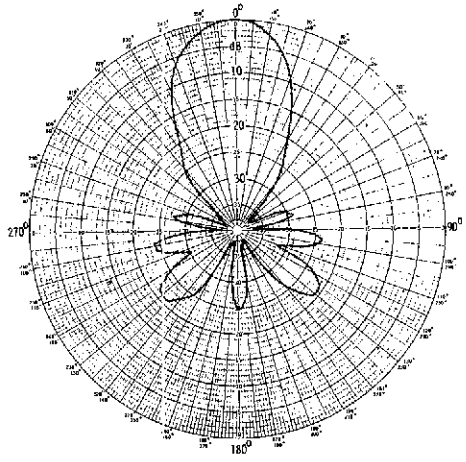

(d) H-plane; 0.0-cm spacing.

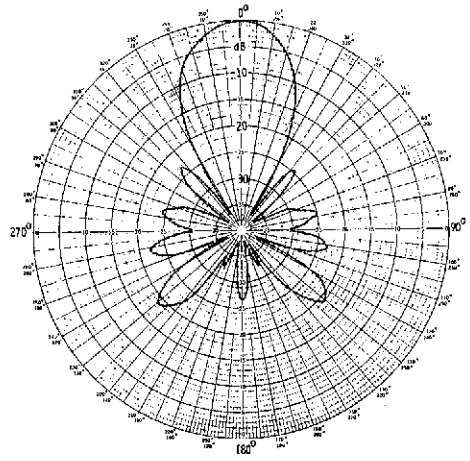

(e) H-plane; 0.635-cm spacing.

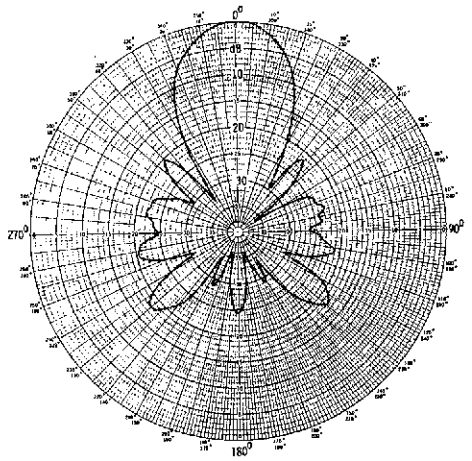

(f) H-plane; 1.27-cm spacing.

Figure 11.- Radiation patterns of a circular waveguide feed exciting a 12.70-cm Plexiglas sphere placed various distances from the waveguide aperture operating at 5.0 GHz.

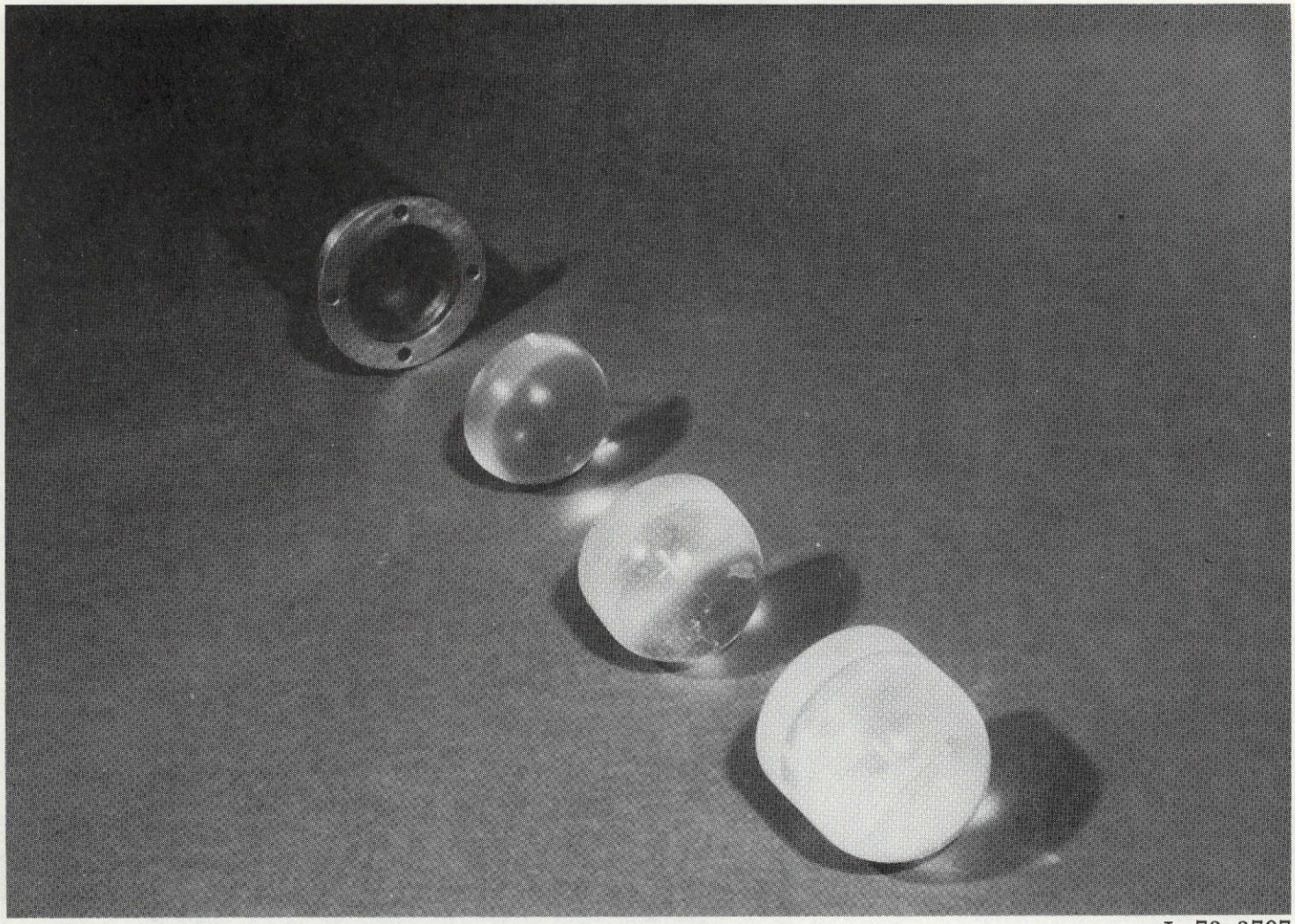

L-73-3797

(a) Hemispherically capped.

Figure 12.- Photographs of hemispherically capped and rectangular block AED antennas.

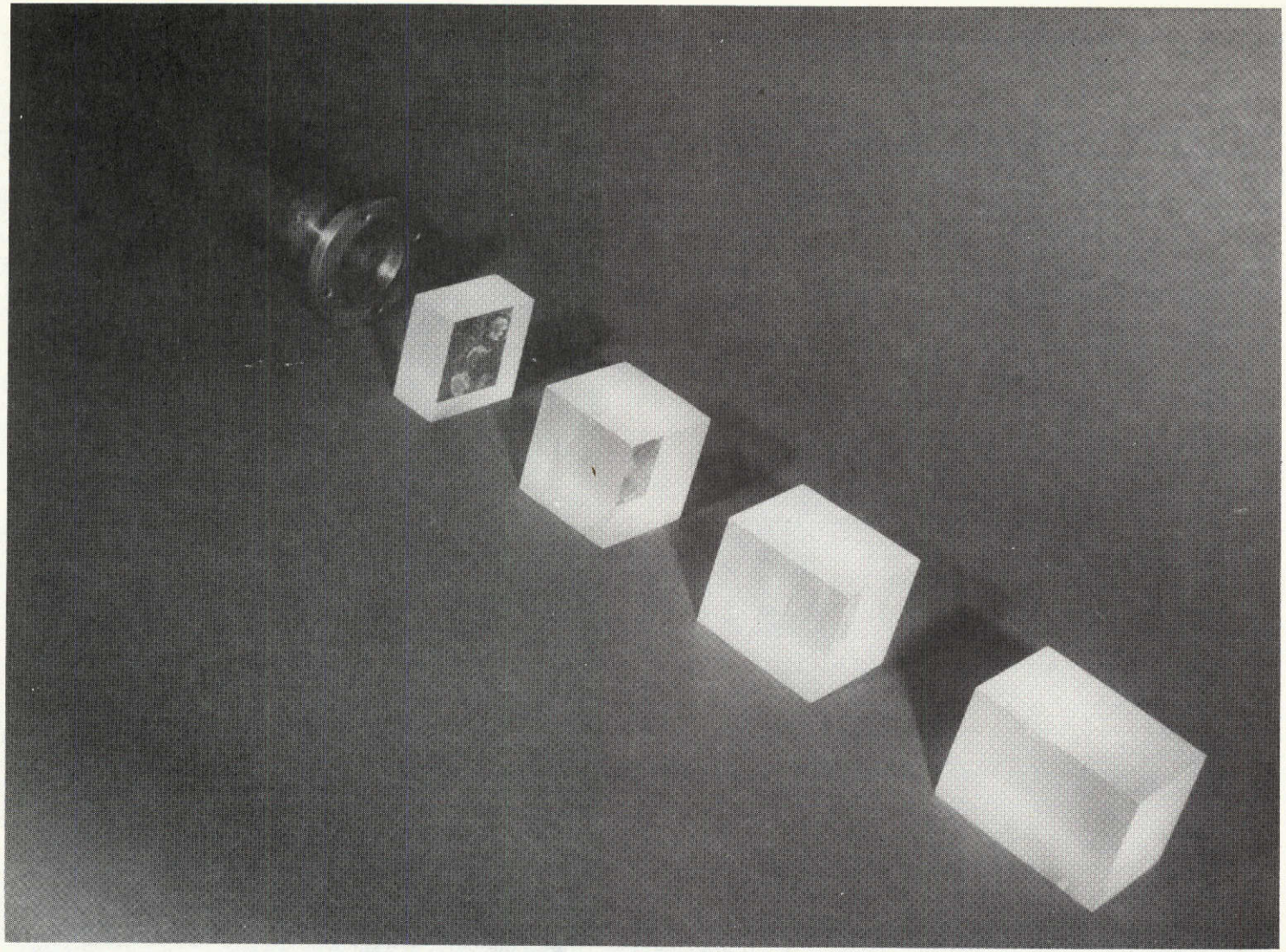

L-73-3799

(b) Rectangular.

Figure 12.- Concluded.

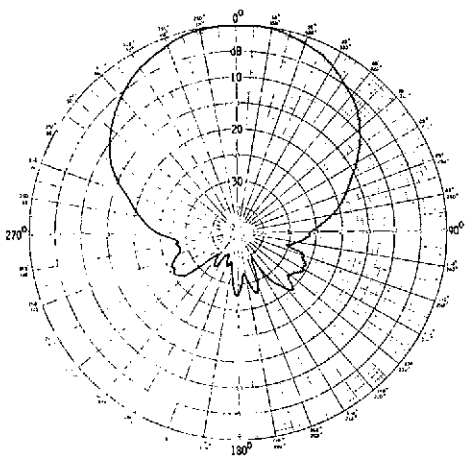

(a) E-plane; 5.08 × 5.08 × 2.54 cm.

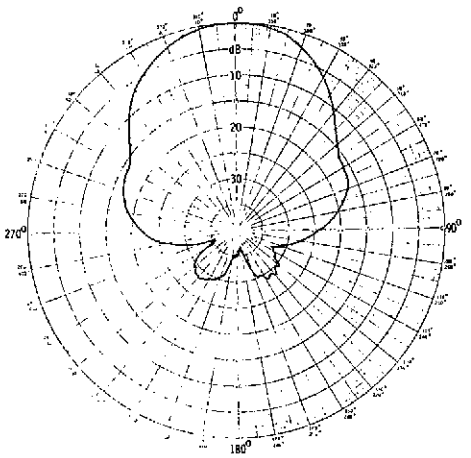

(b) E-plane; 5.08 × 5.08 × 5.08 cm.

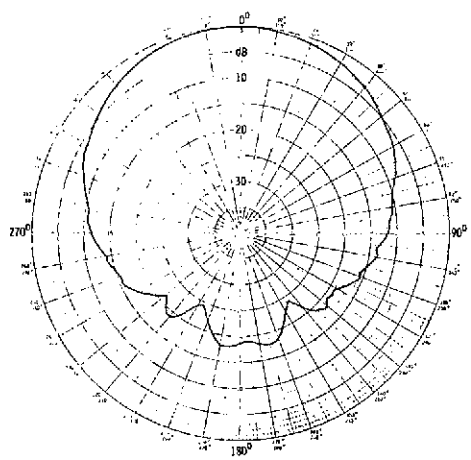

(c) H-plane; 5.08 × 5.08 × 2.54 cm.

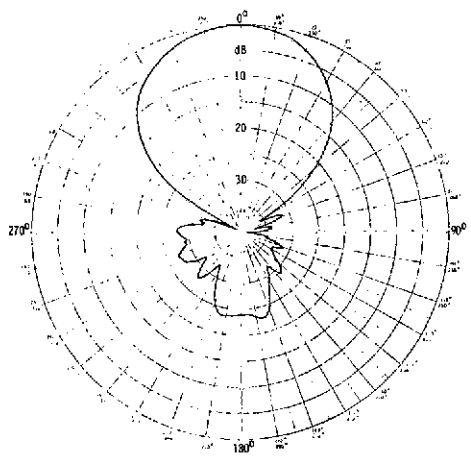

(d) H-plane; 5.08 × 5.08 × 5.08 cm.

Figure 13.- Radiation patterns of a circular waveguide exciting a Plexiglas block of different dimensions at 5.0 GHz.

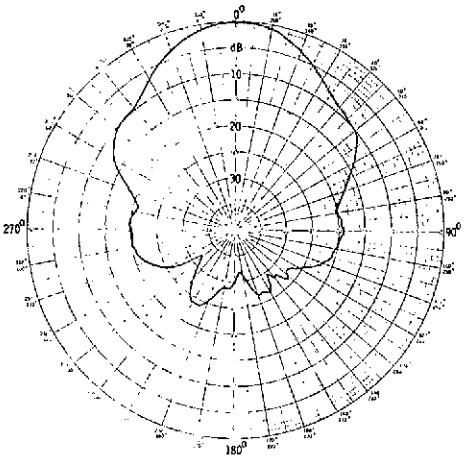

(e) E-plane; 5.08 × 5.08 × 15.24 cm.

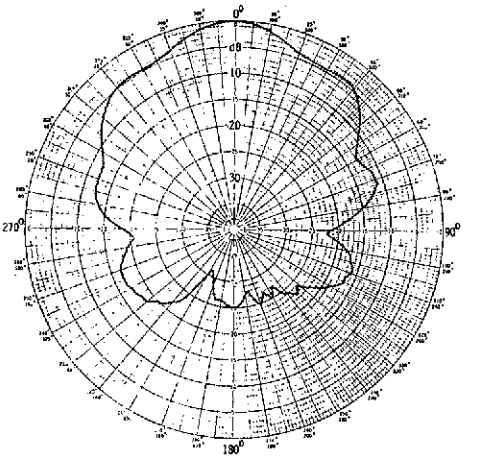

(f) E-plane; 5.08 × 5.08 × 20.32 cm.

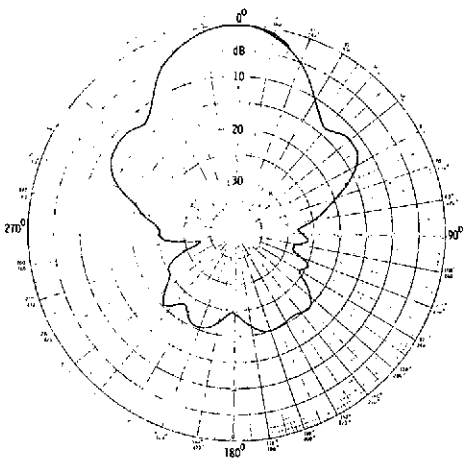

(g) H-plane; 5.08 × 5.08 × 15.24 cm.

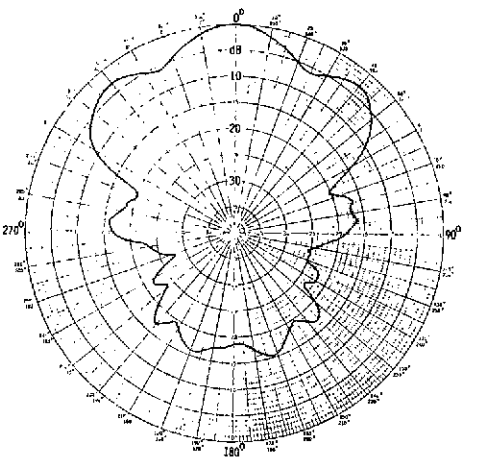

(h) H-plane; 5.08 × 5.08 × 20.32 cm.

Figure 13.- Concluded.

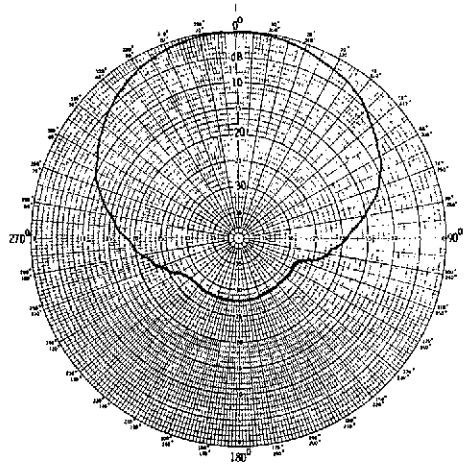

(a) E-plane; 0.0 cm.

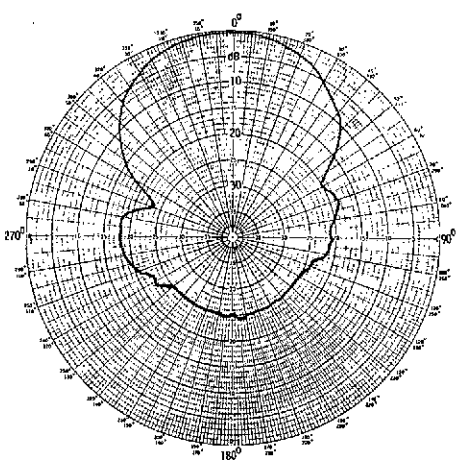

(b) E-plane; 1.27 cm.

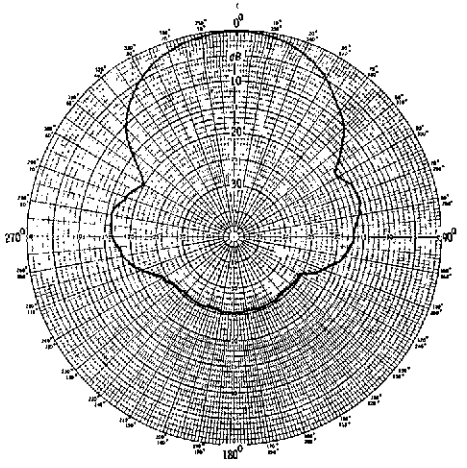

(c) E-plane; 2.54 cm.

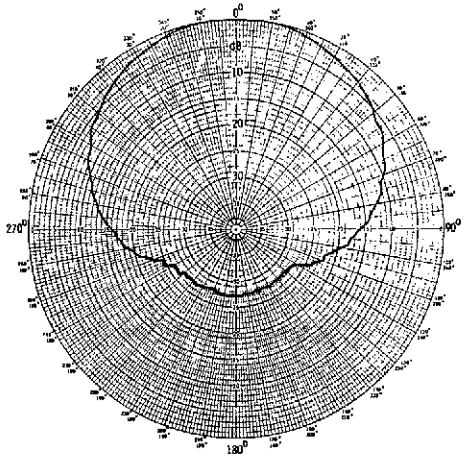

(d) H-plane; 0.0 cm.

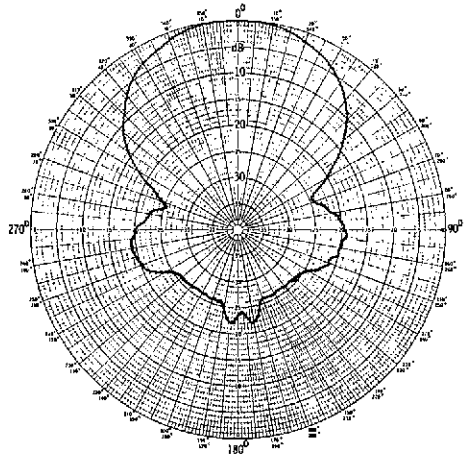

(e) H-plane; 1.27 cm.

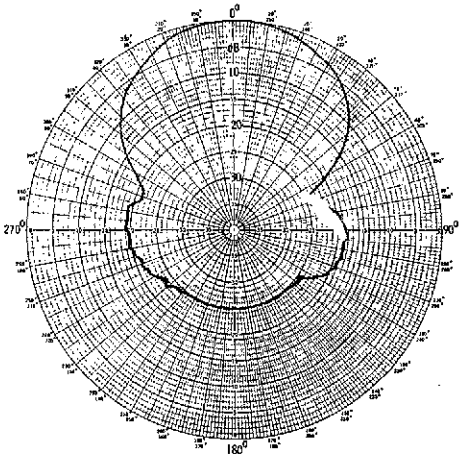

(f) H-plane; 2.54 cm.

Figure 14.- Radiation patterns of a circular waveguide antenna exciting a 5.08-cm hemispherically capped circular Plexiglas cylinder at 5.0 GHz as a function of cylinder length.

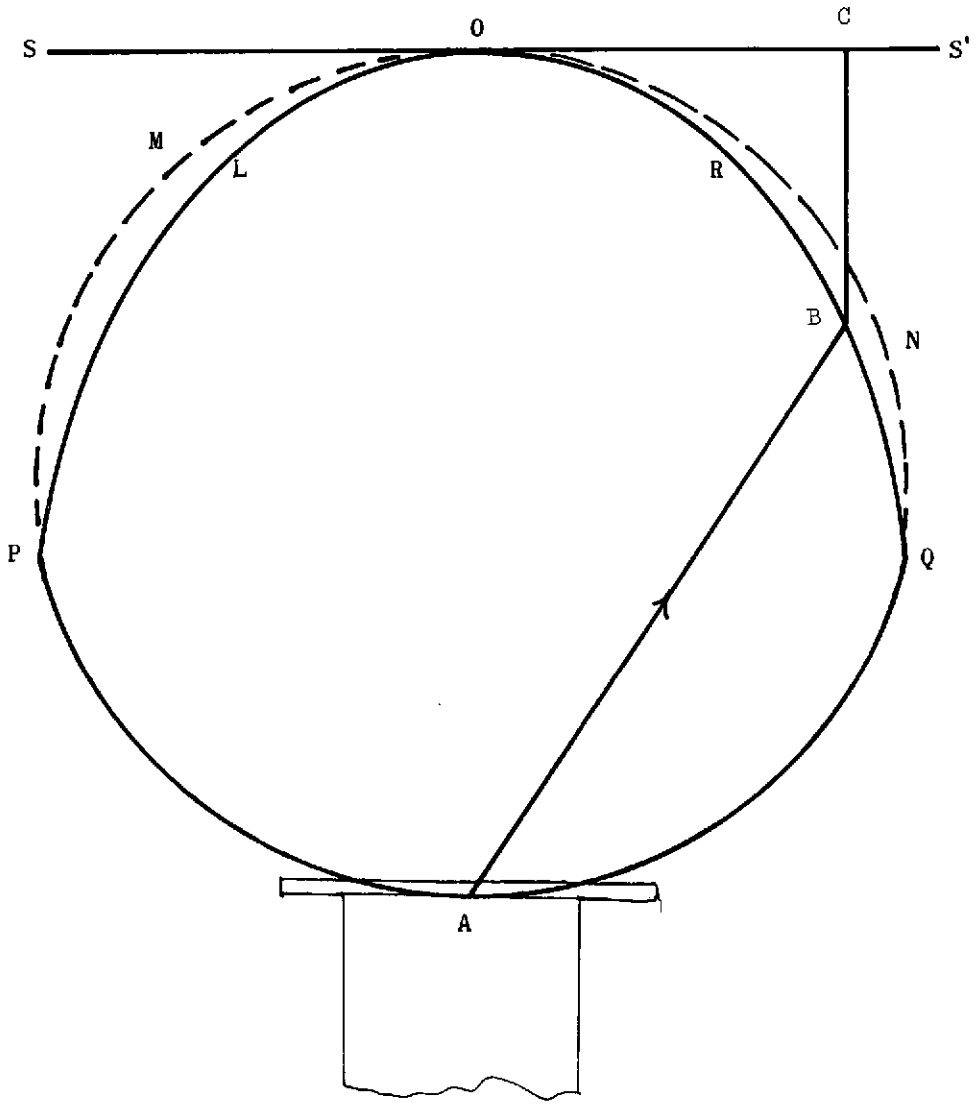

(a) Sketch.

Figure 15.- Shaped dielectric object. (Shaped in a manner so as to produce uniform phase in a plane in front of the object for all rays emanating from a point.)

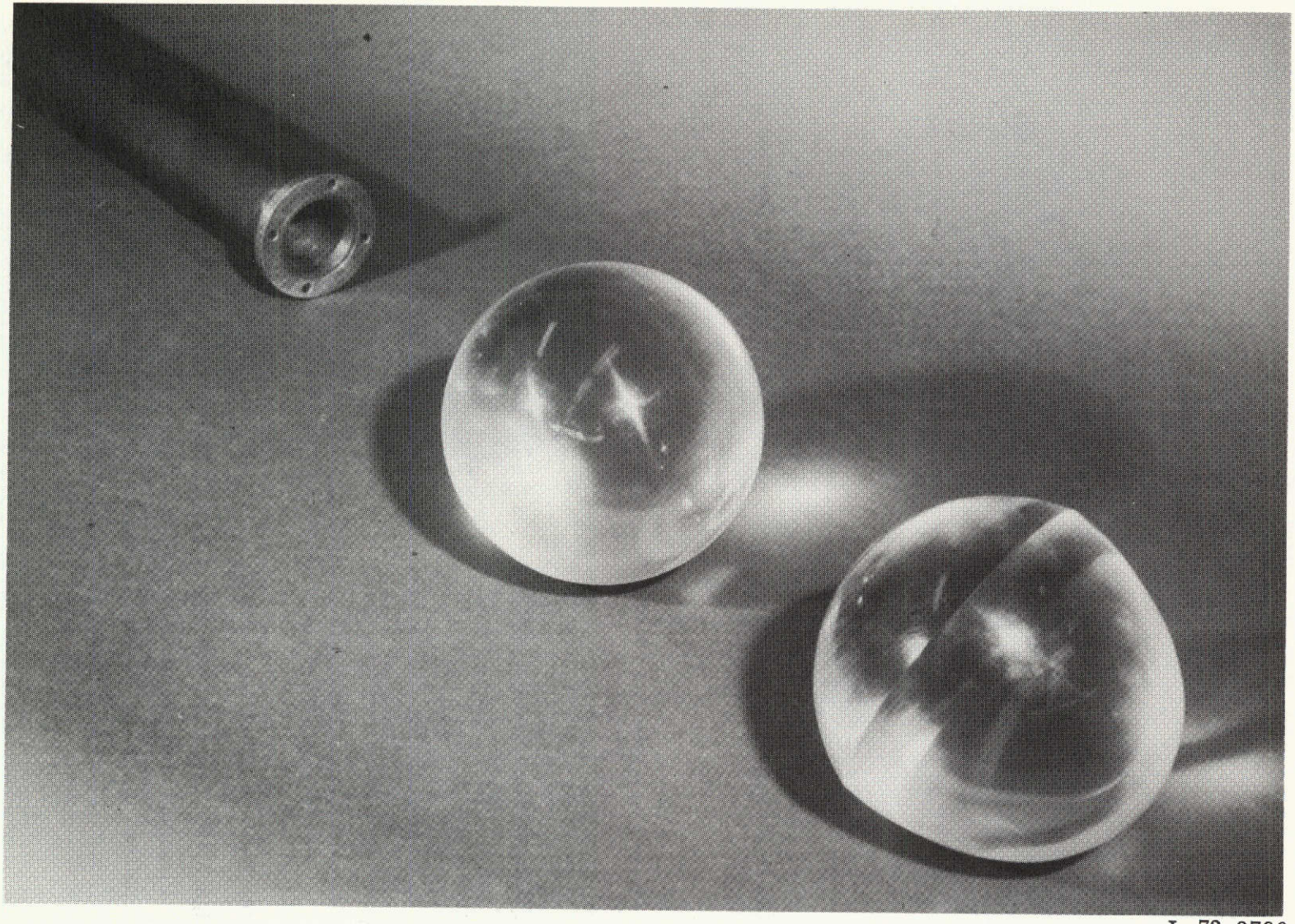

L-72-3796

(b) Photograph.

Figure 15.- Concluded.

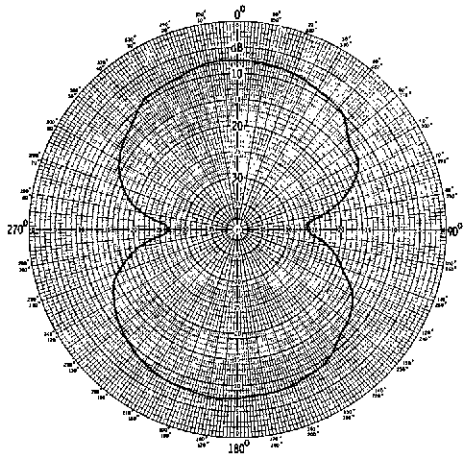

(a) E-plane; inverted position.

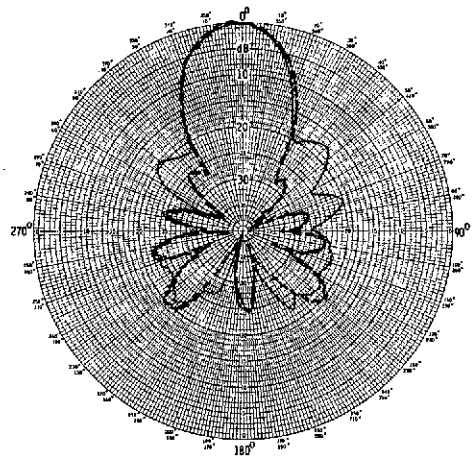

(b) E-plane; direct position.

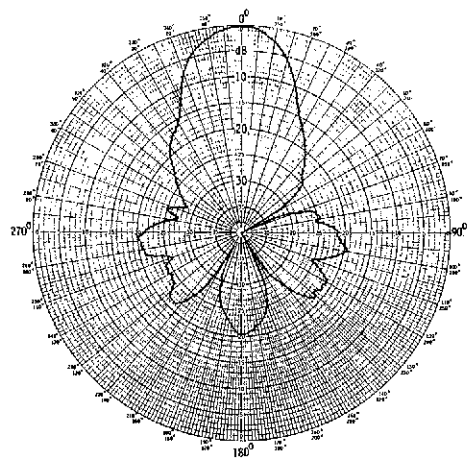

(c) H-plane; inverted position.

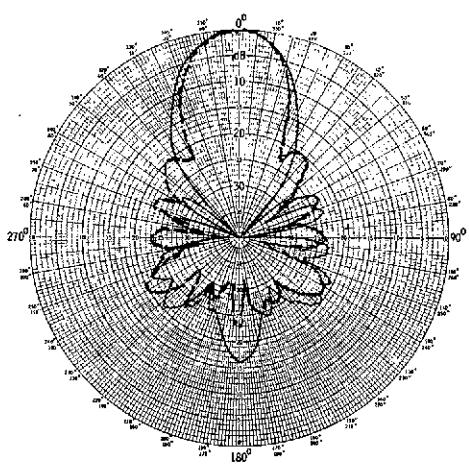

(d) H-plane; direct position.

Figure 16.- Radiation patterns of a circular waveguide exciting a shaped Plexiglas obstacle at an operating frequency of 5.0 GHz. (The dashed pattern is for the unshaped sphere in the same waveguide.)

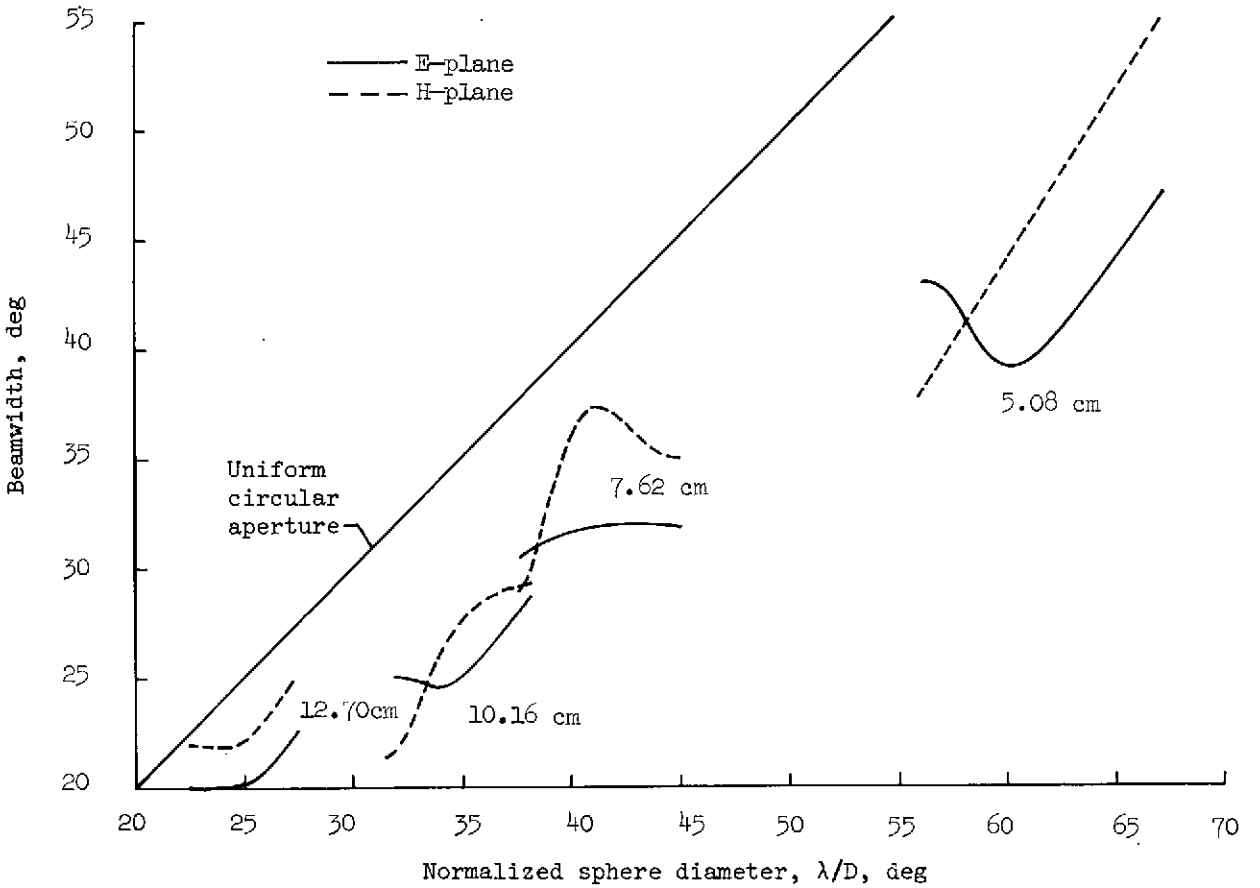

(a) Circular waveguide feed.

Figure 17.- Variation of the E-plane and H-plane 3-dB beamwidth as a function of the normalized sphere diameter for various diameter Plexiglas spheres.

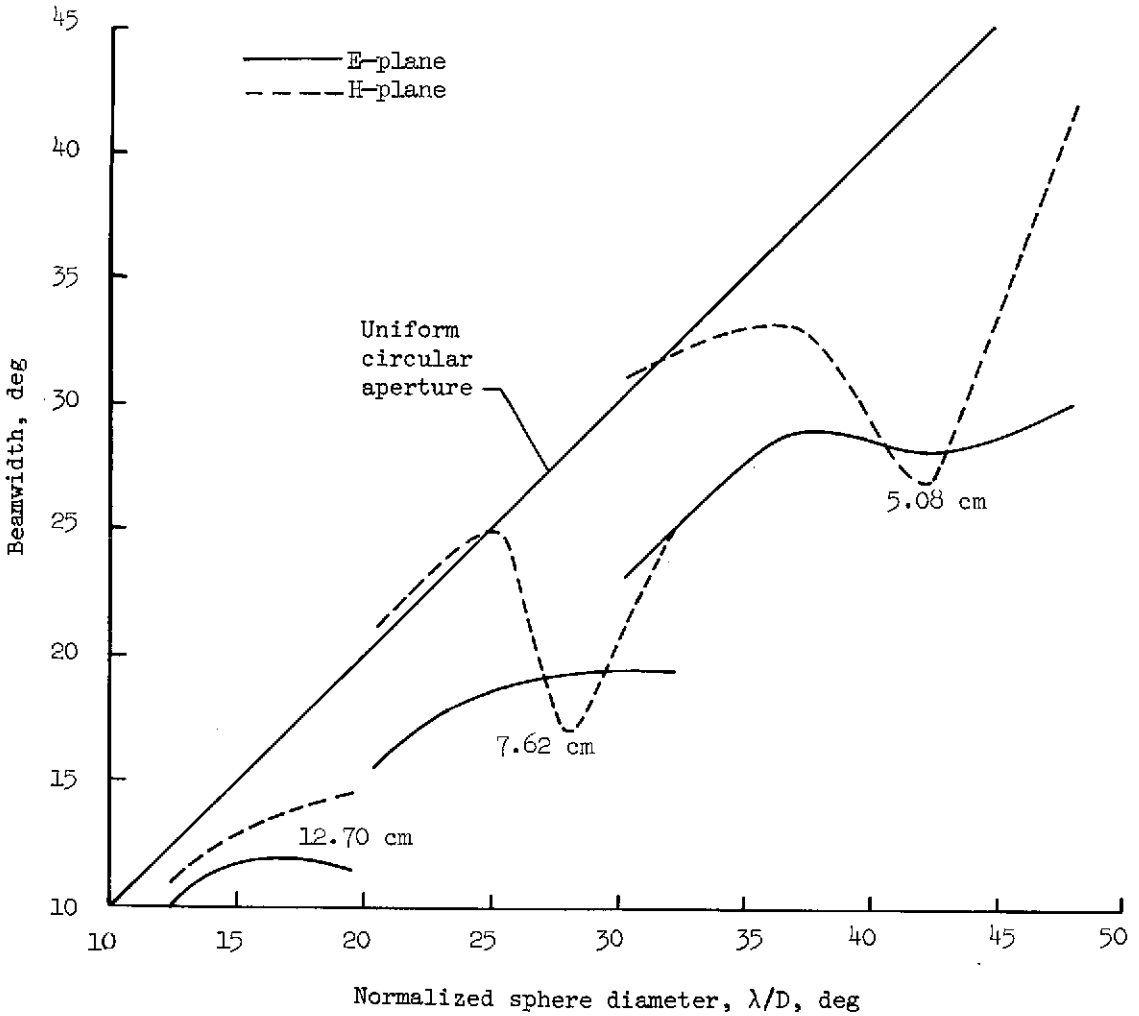

(b) Rectangular waveguide feed.

Figure 17.- Continued.

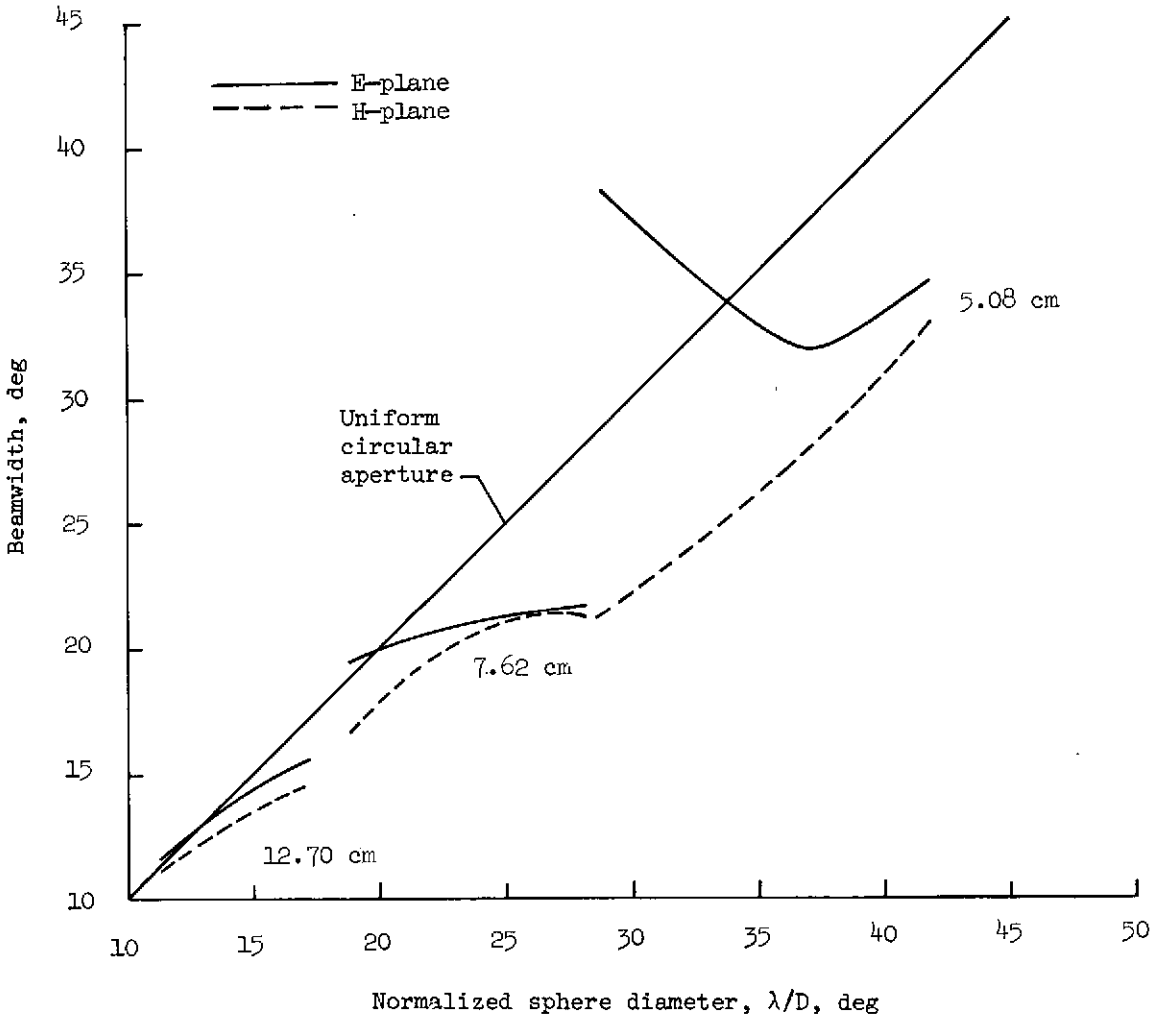

(c) Square-horn waveguide feed.

Figure 17.- Concluded.

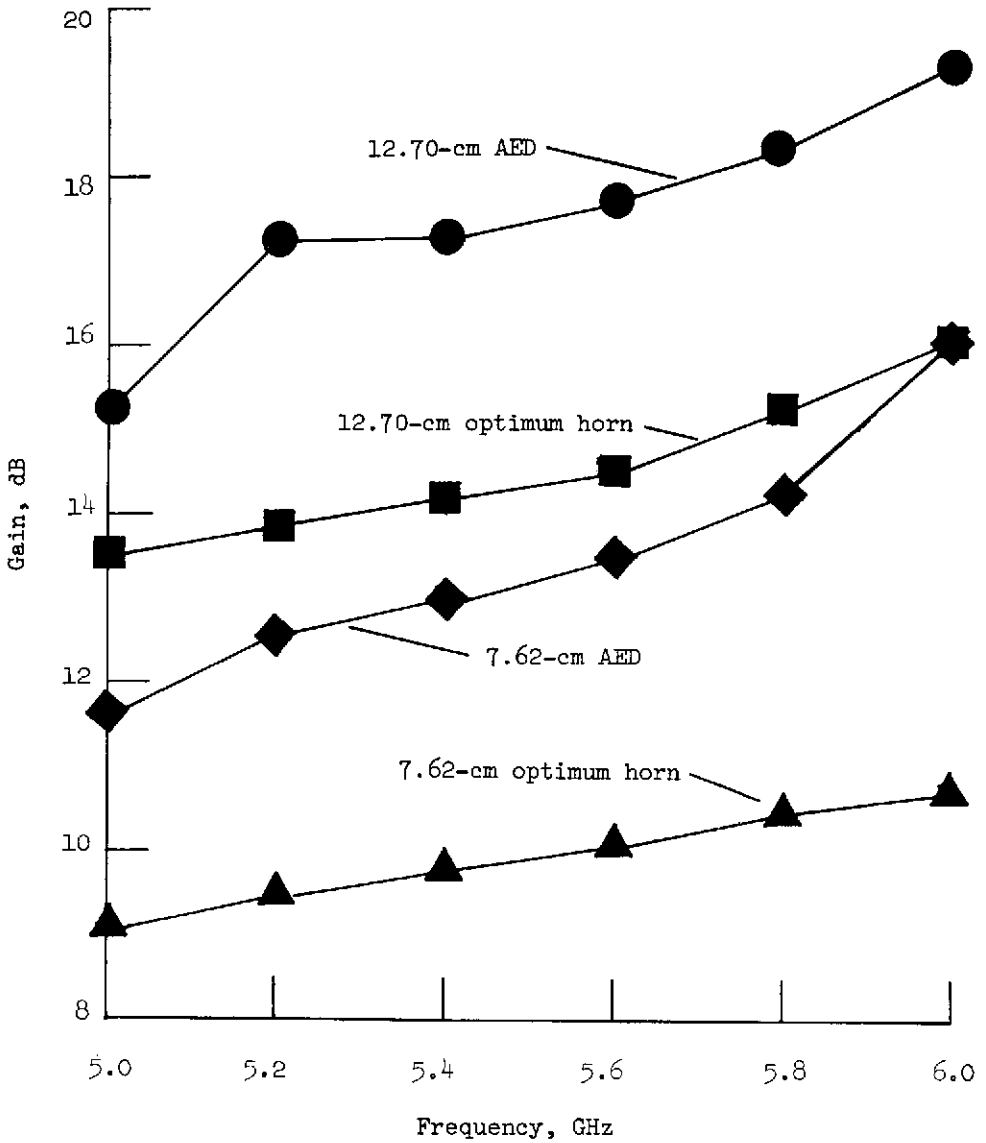

Figure 18.- Gain of spherical AED antennas fed by a circular waveguide compared with the gain of the optimum horn having the same cross section.

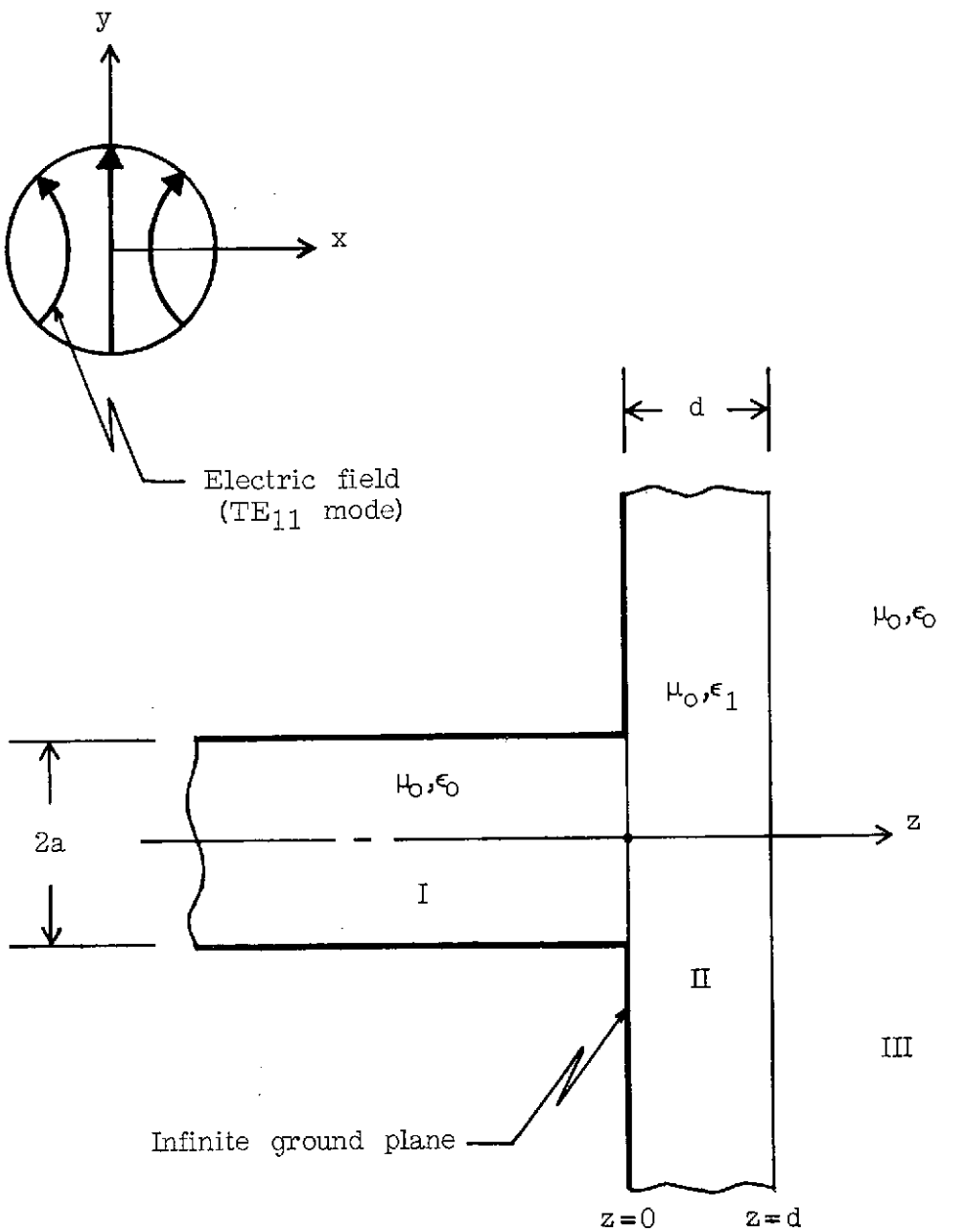

Figure 19.- Circular aperture coated with homogeneous lossy dielectric.

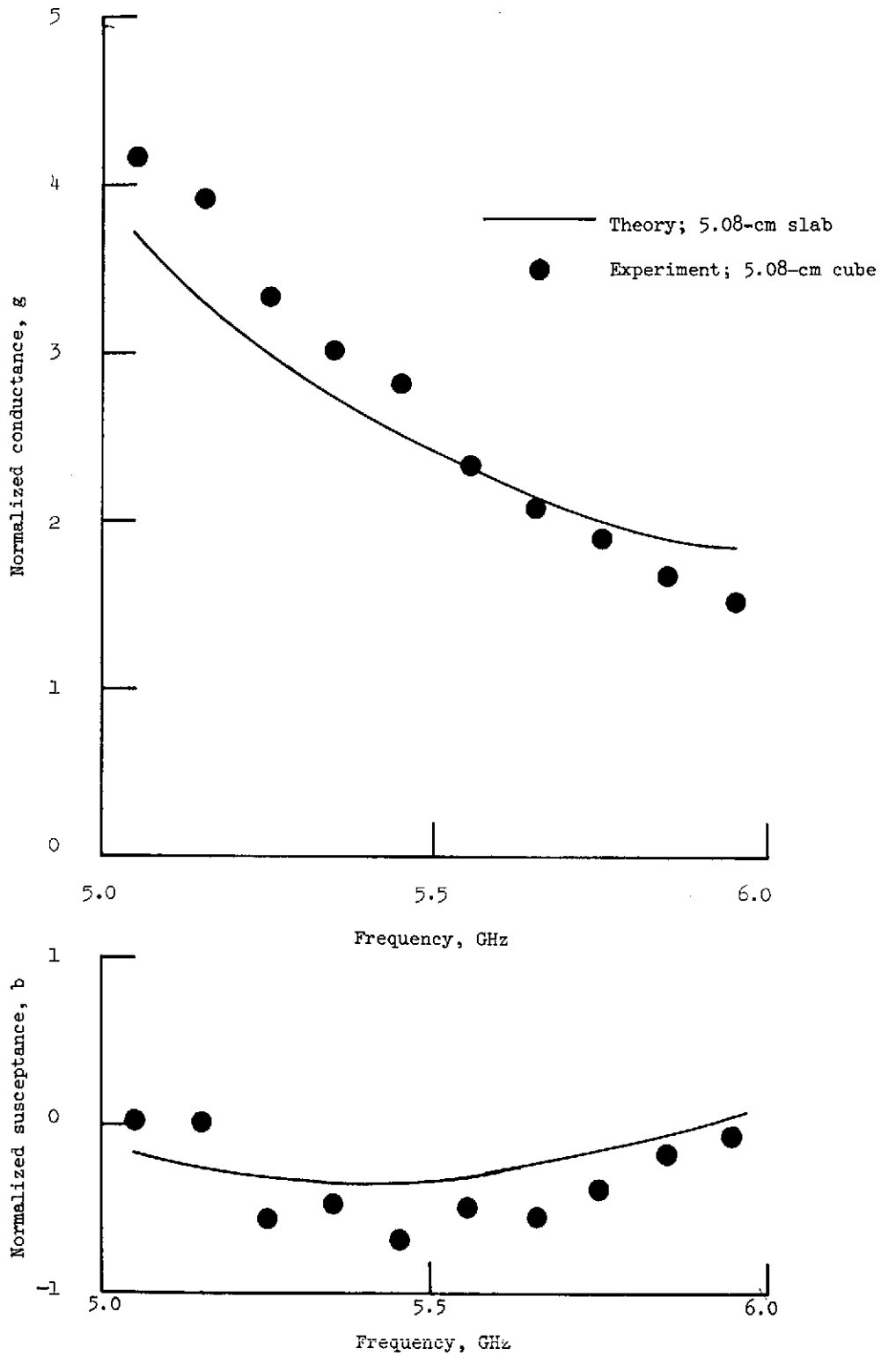

Figure 20.- Comparison of calculated and measured aperture admittance of the circular waveguide feed covered by a Plexiglas slab or cube.

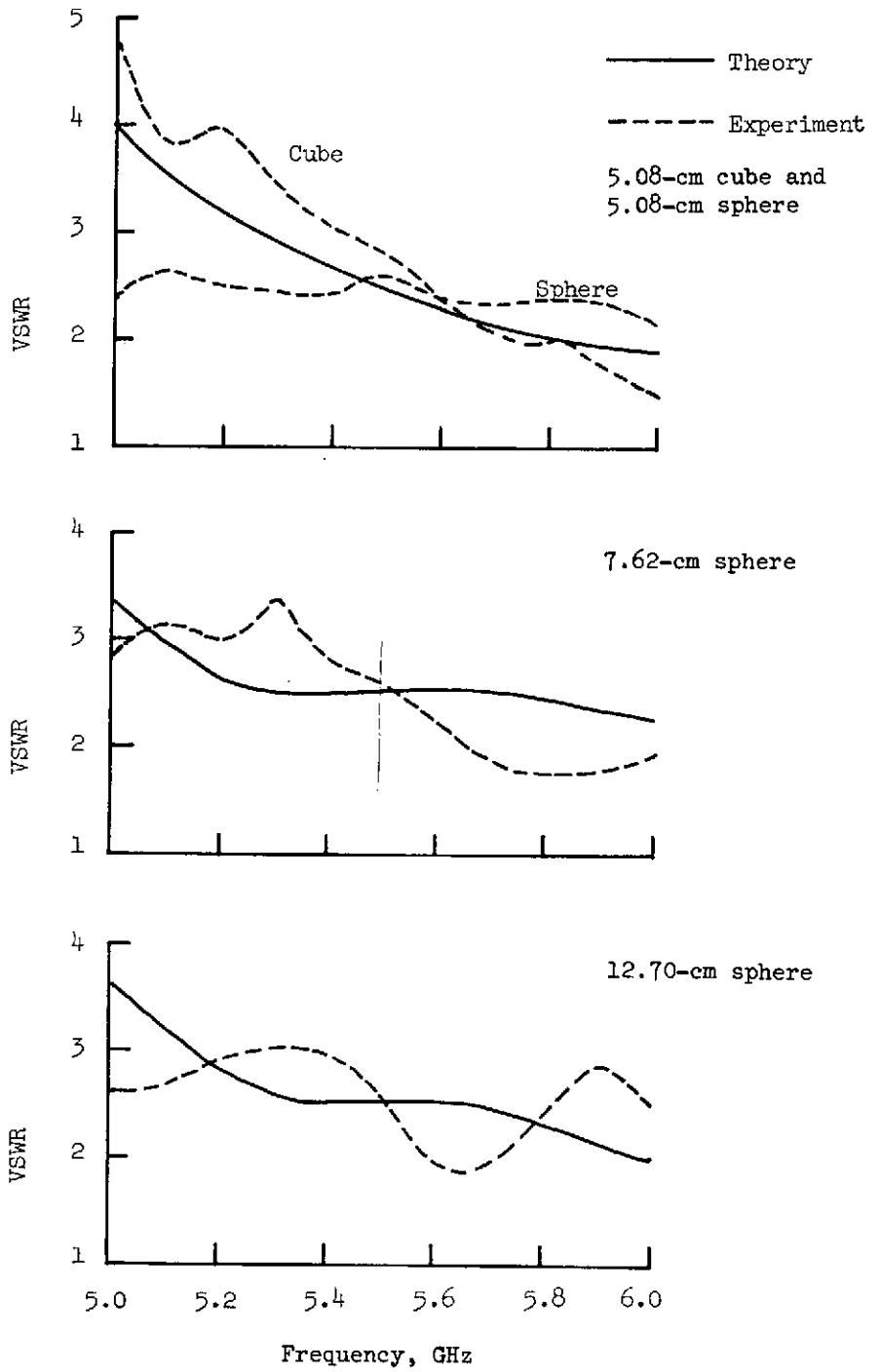

Figure 21.- Calculated and measured values of the VSWR of circular waveguide fed AED antennas over the frequency range from 5.0 to 6.0 GHz.

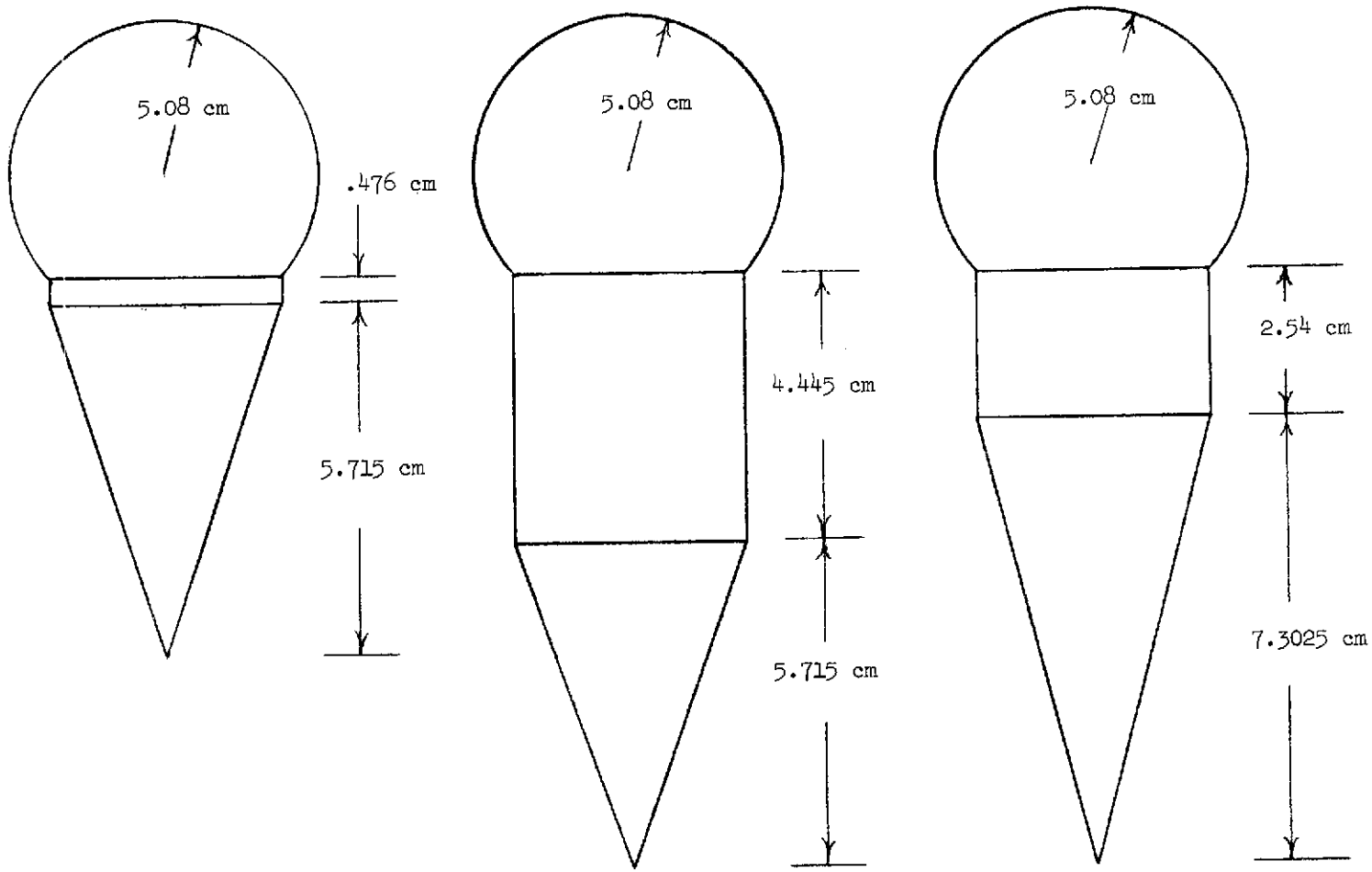

(a) Taper (a). (b) Taper (b). (c) Taper (c).

Figure 22.- Sketch and photograph of tapered Plexiglas sections for matching the circular waveguide AED antennas.

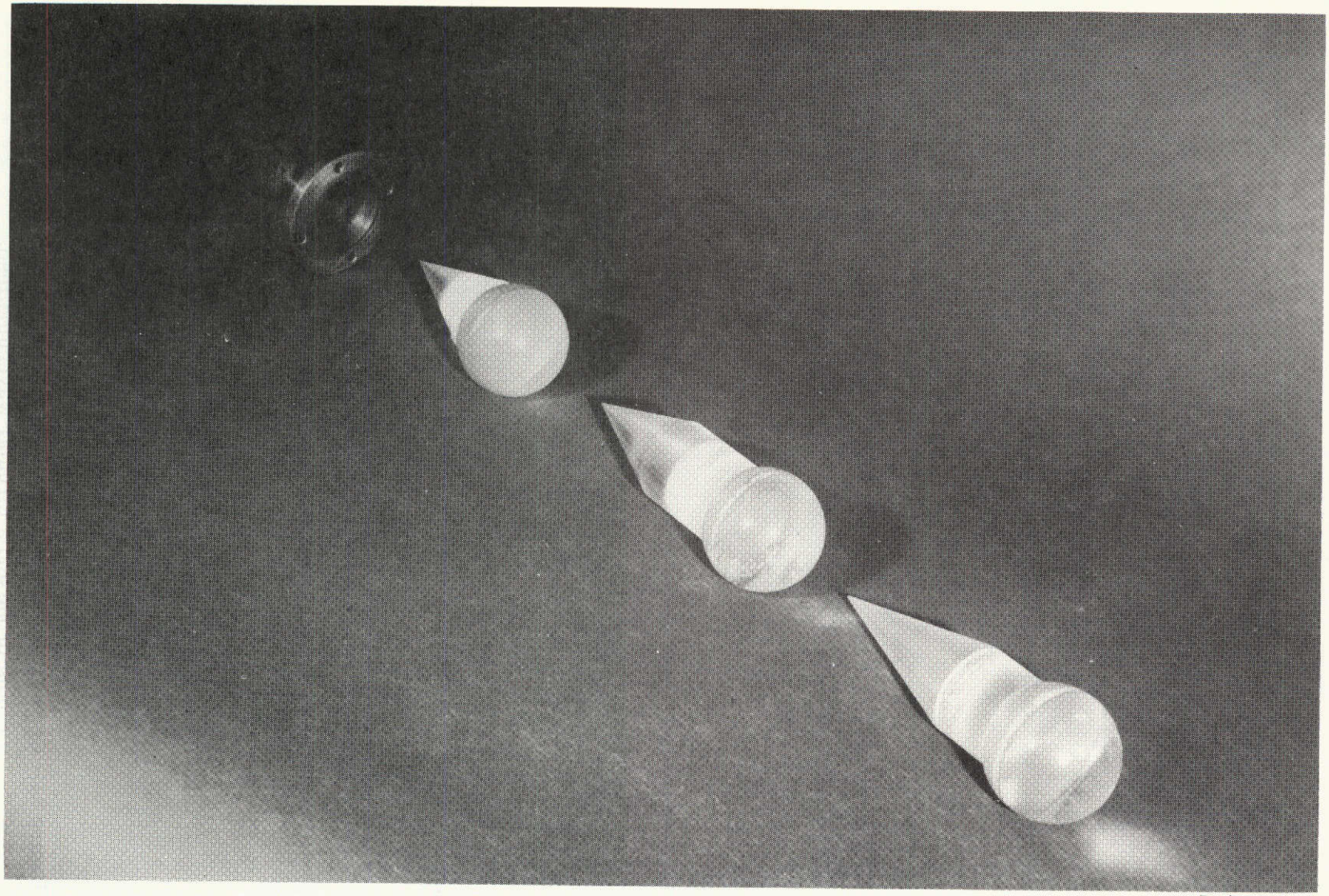

L-73-3798

(d) Photograph of tapered Plexiglas sections.

Figure 22.- Concluded.

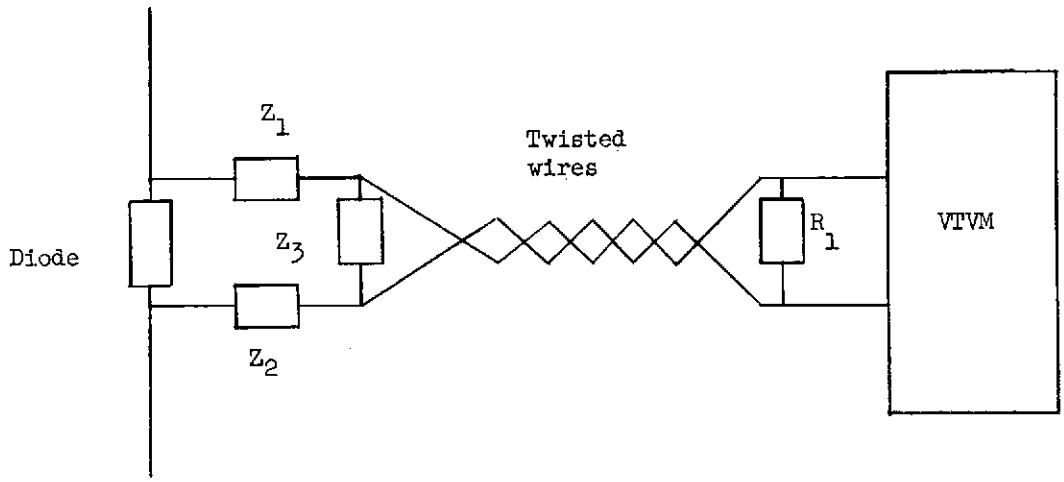

Figure 23.- Sketch showing the detection circuit for the near-field amplitude measurements. (Diode, MA 4I512; Z_1, 1000 ohms; Z_2, 1000 ohms; Z_3, 500 pF; R_1, 10 000 ohms.)

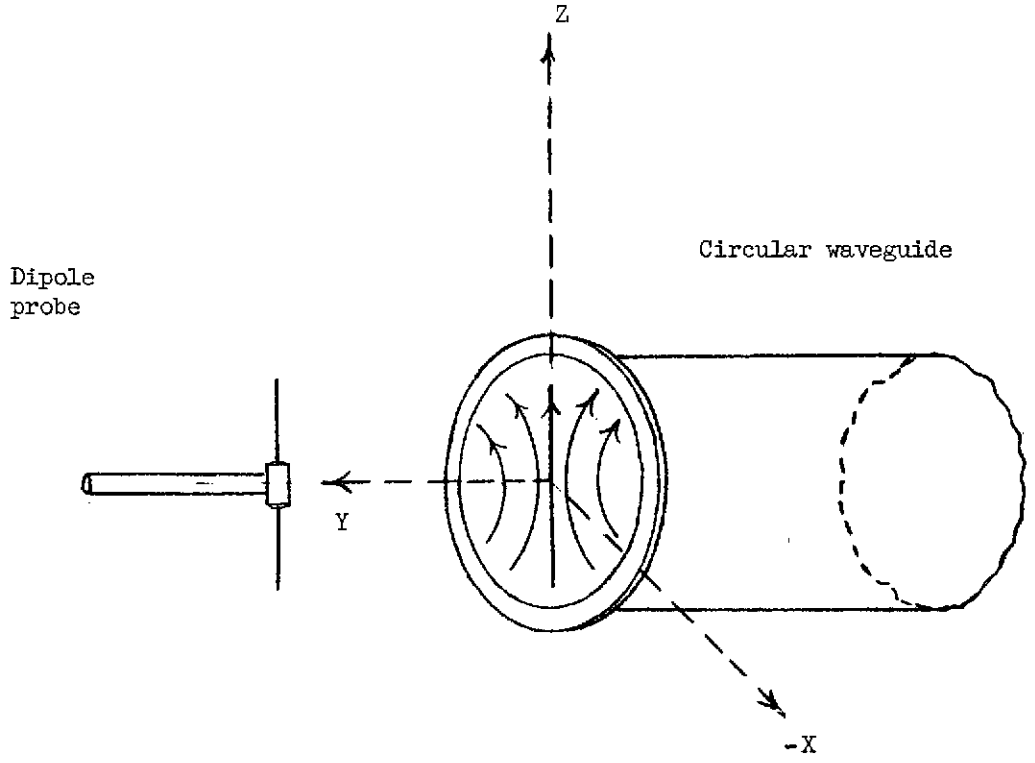

Figure 24.- Geometry of the near-field amplitude measurements using a dipole probe and a circular waveguide feed.

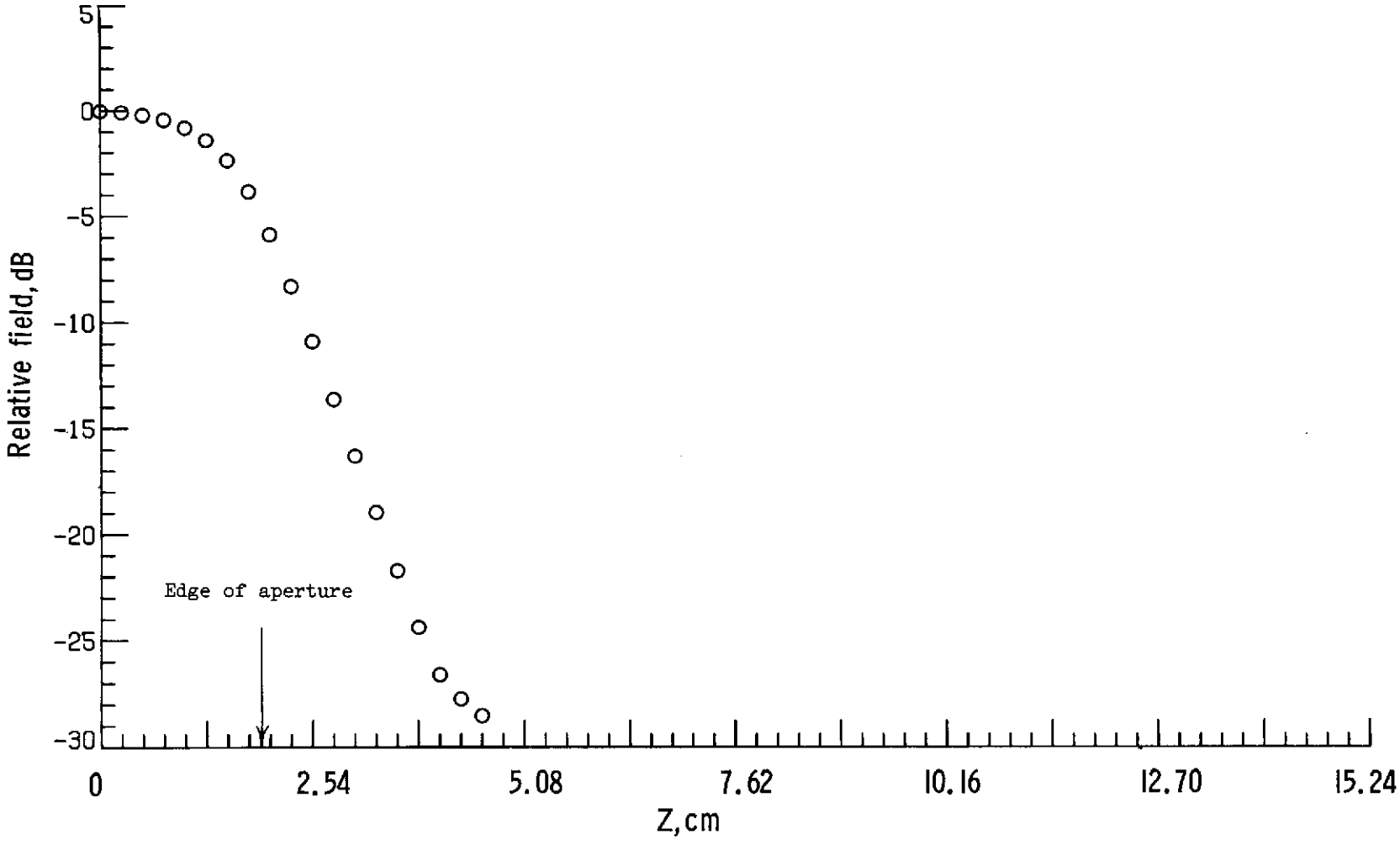

(a) E-plane at Y = 0.508 cm, X = 0.0 cm, and f = 6.0 GHz.

Figure 25.- Near-field amplitude measurement of an open-end circular waveguide feed.

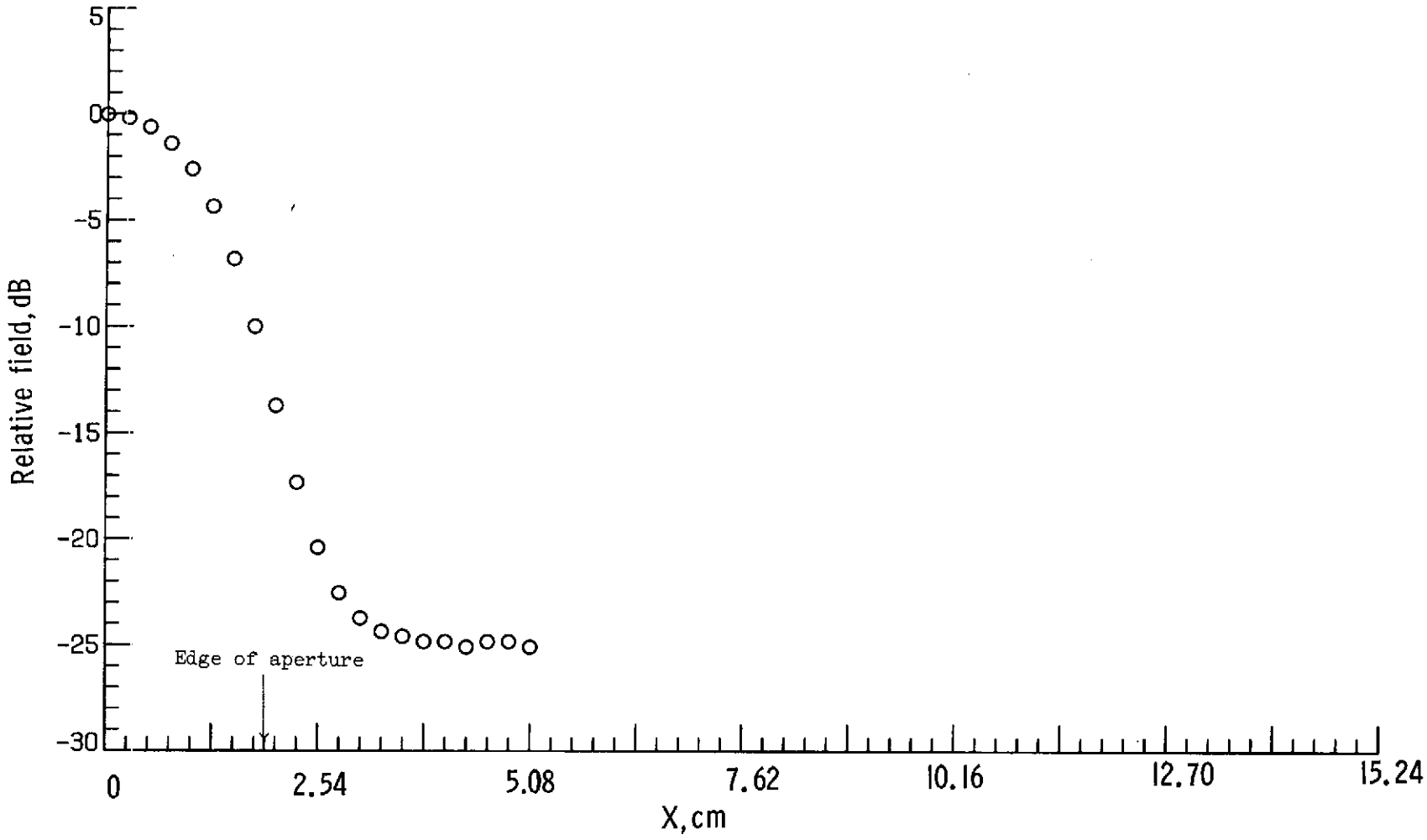

(b) H-plane at Y = 0.508 cm, Z = 0.0 cm, and f = 6.0 GHz.

Figure 25.- Continued.

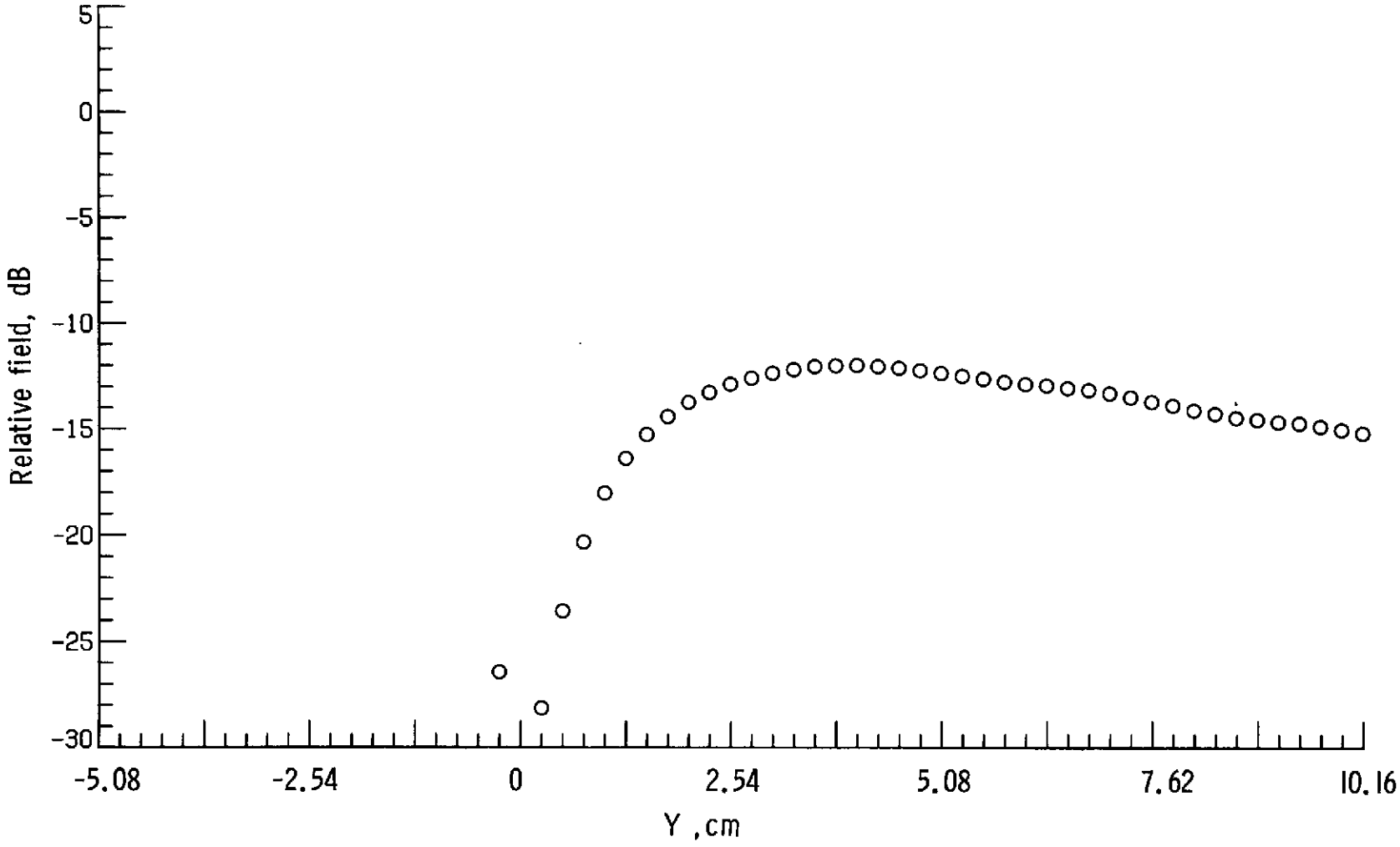

(c) Along the side at X = 3.048 cm, Z = 0.0 cm, and f = 6.0 GHz.

Figure 25.- Concluded.

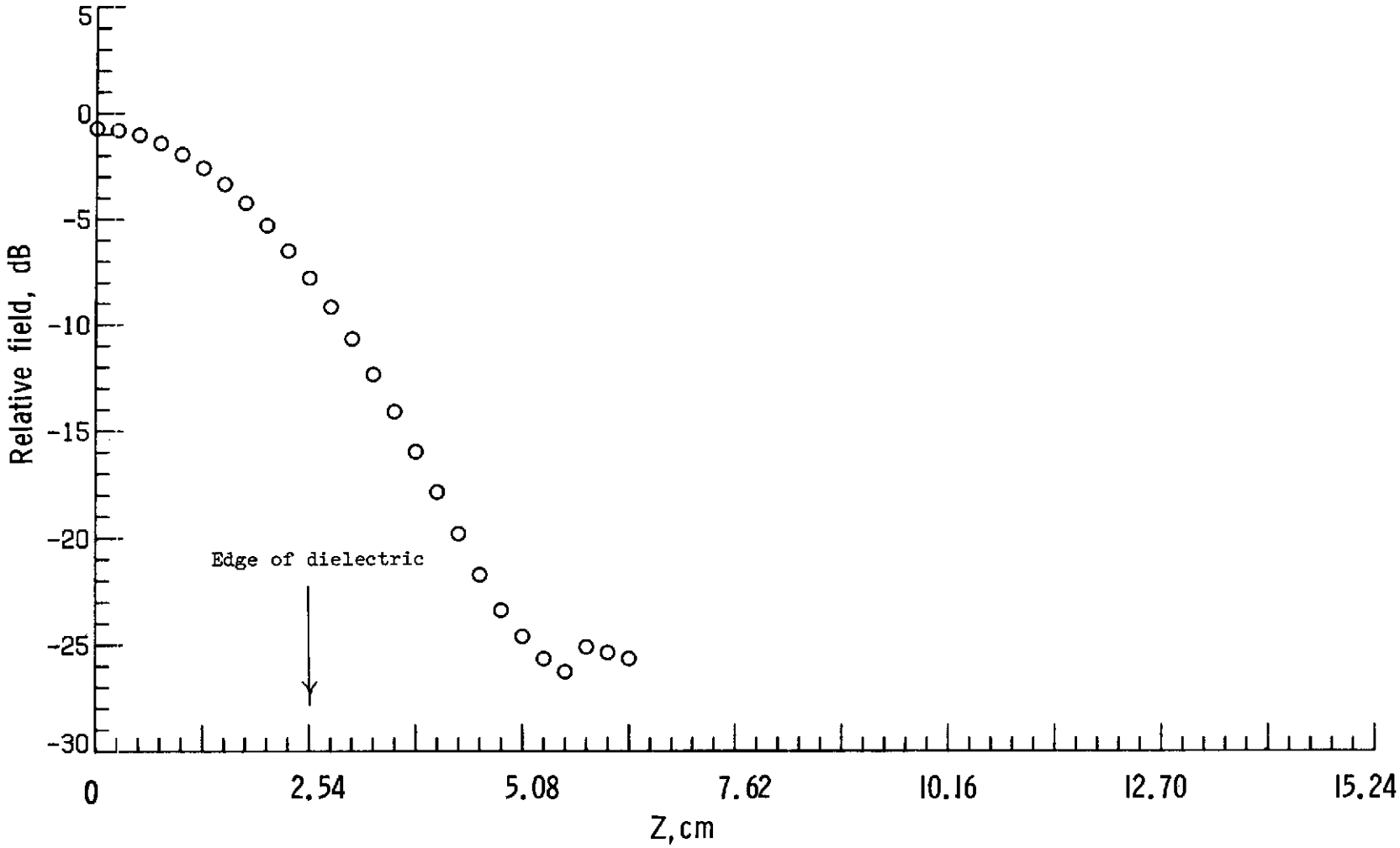

(a) E-plane at Y = 0.508 cm, X = 0.0 cm, and f = 6.0 GHz.

Figure 26.- Near-field amplitude measurement of a circular waveguide feeding a 5.08-cm Plexiglas cube.

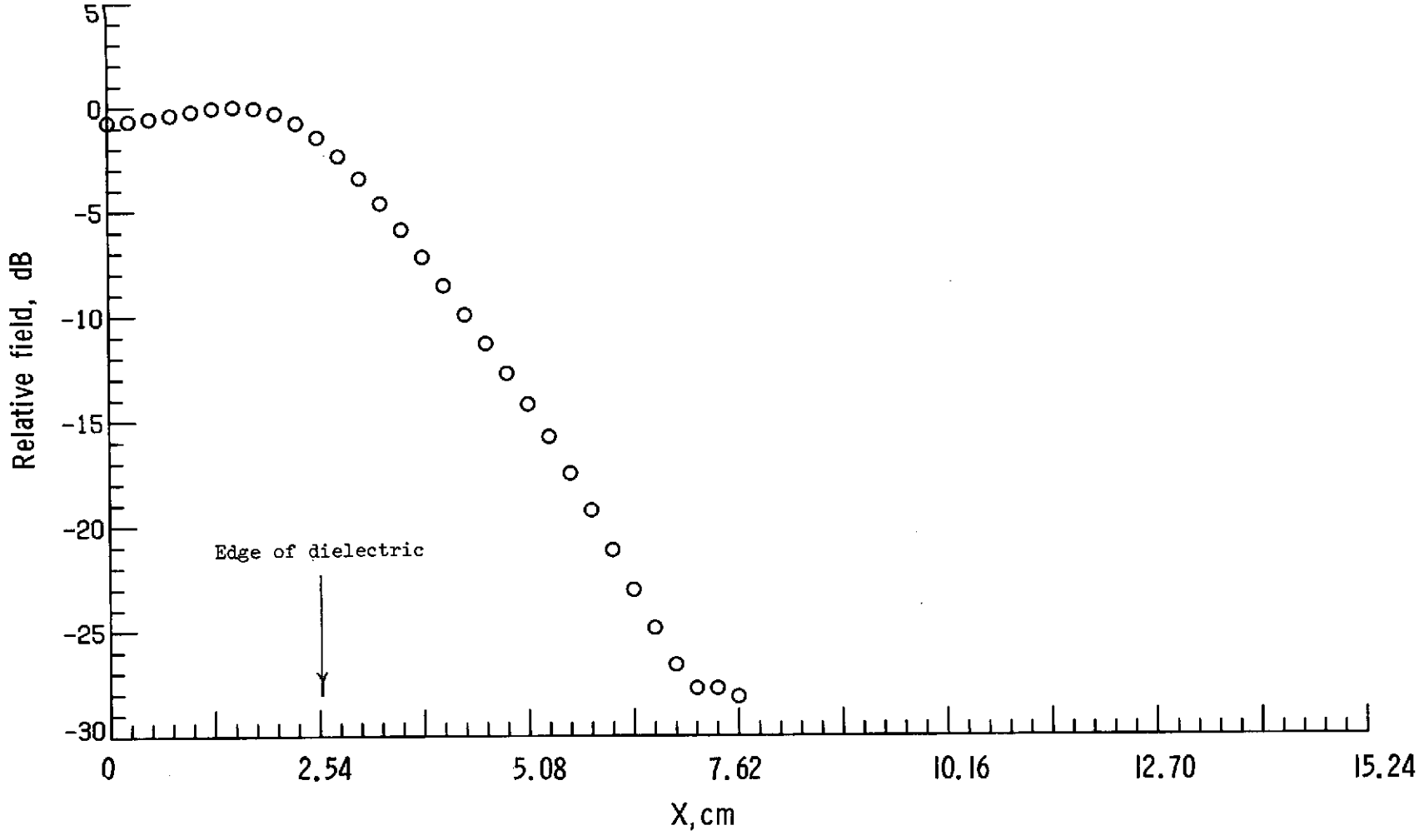

(b) H-plane at Y = 0.508 cm, Z = 0.0 cm, and f = 6.0 GHz.

Figure 26.- Continued.

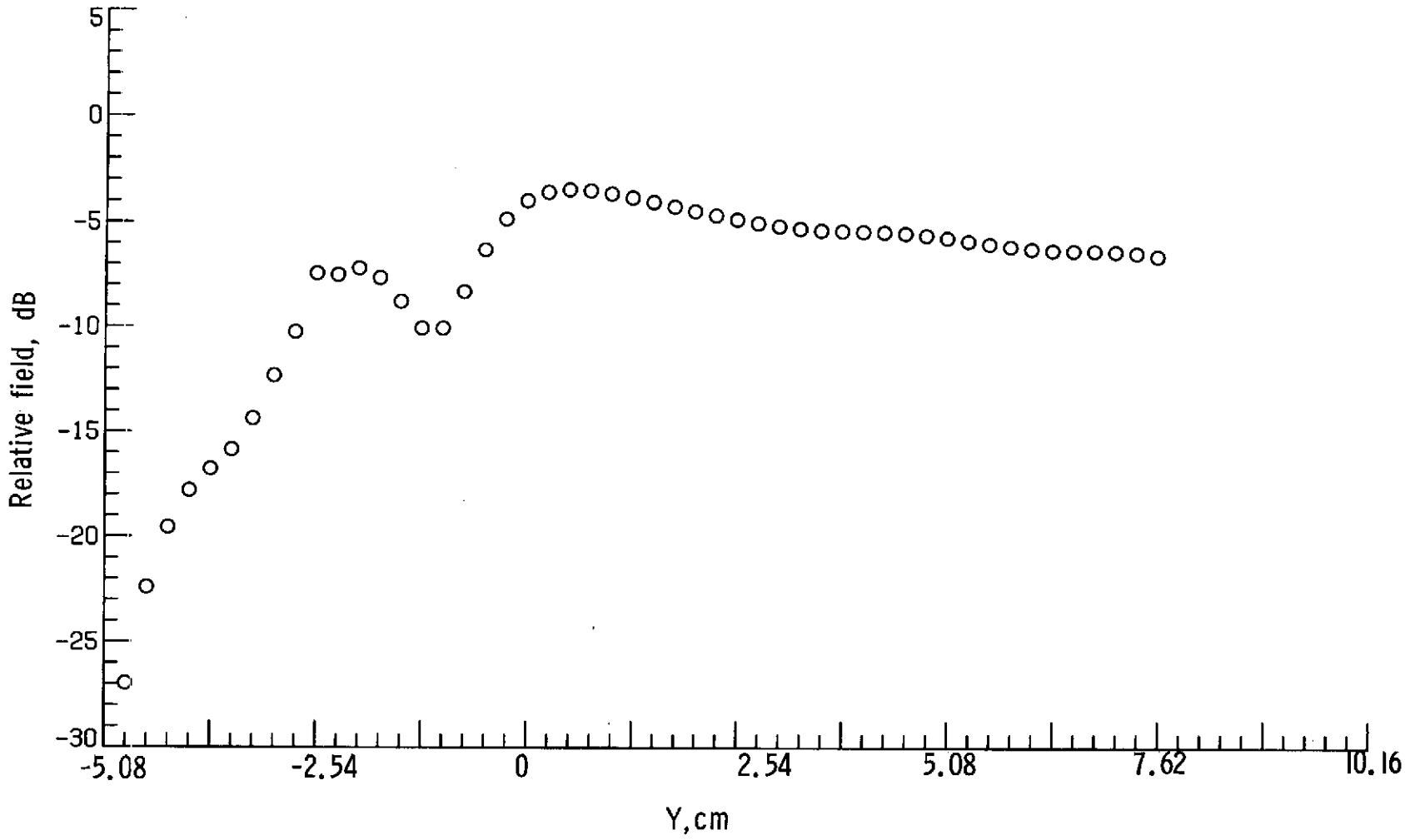

(c) Along the side at X = 3.048 cm, Z = 0.0 cm, and f = 6.0 GHz.

Figure 26.- Concluded.

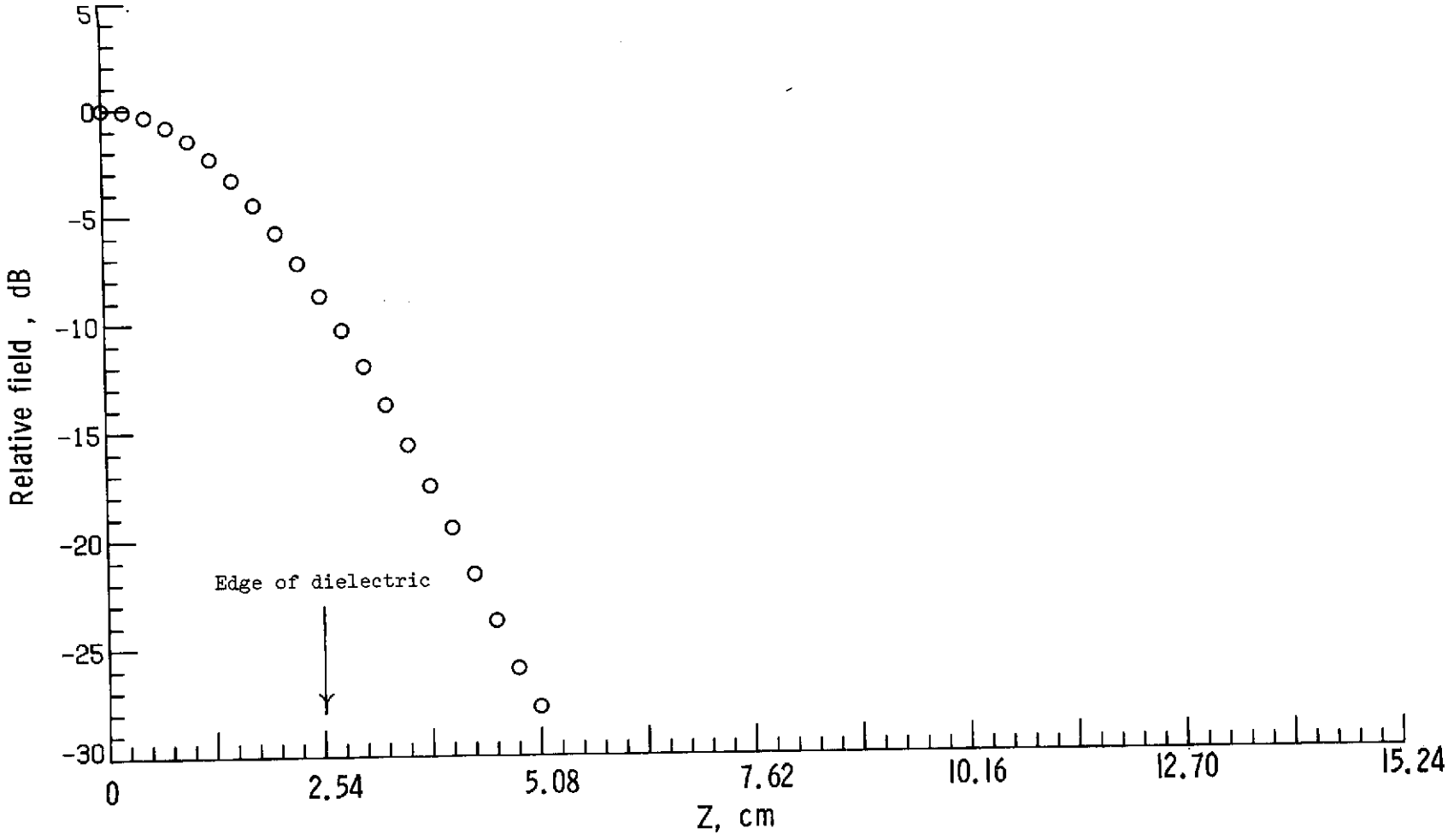

(a) E-plane at Y = 0.508 cm, X = 0.0 cm, and f = 6.0 GHz.

Figure 27.- Near-field amplitude measurement of a circular waveguide feeding a 5.08-cm Plexiglas sphere.

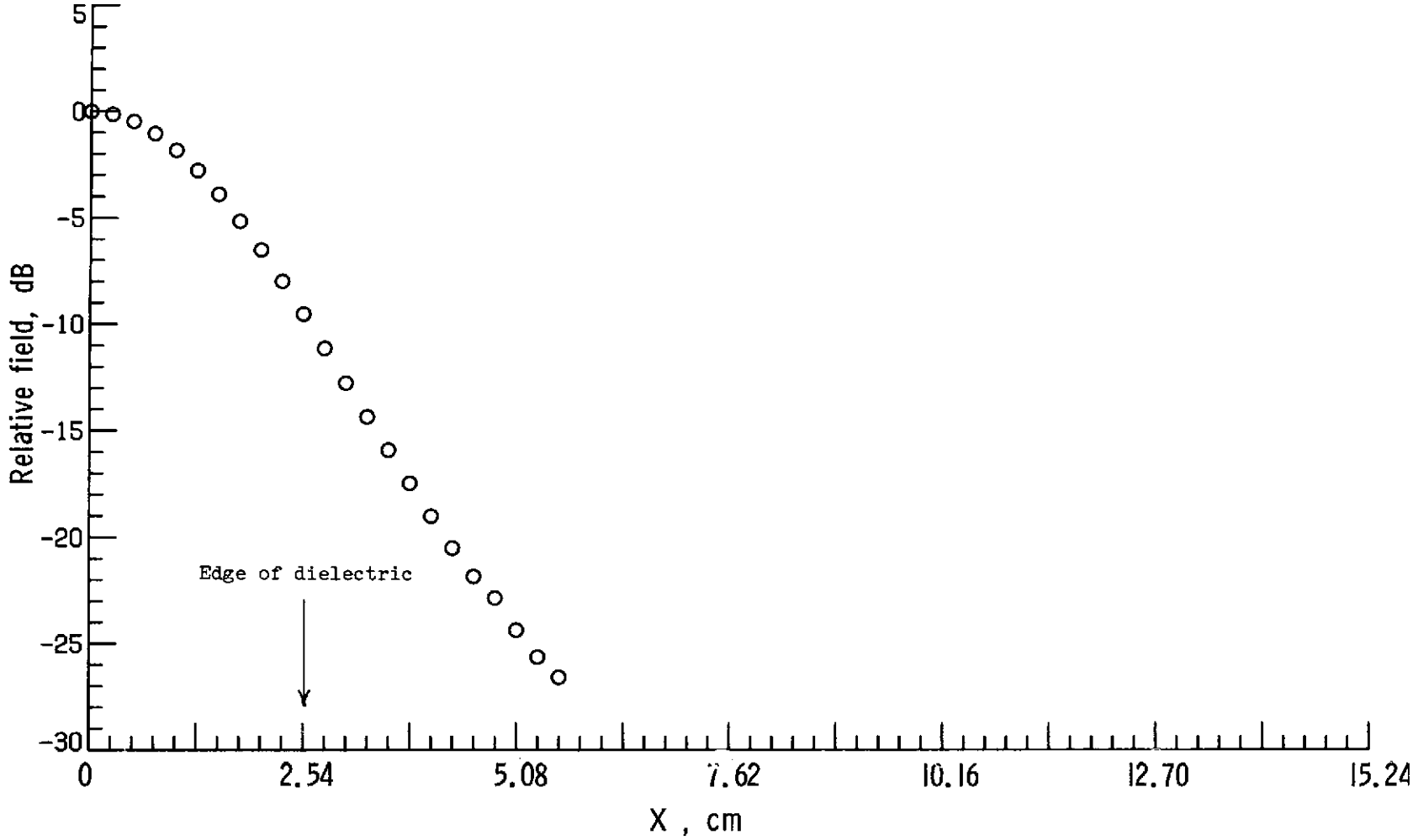

(b) H-plane at Y = 0.508 cm, Z = 0.0 cm, and f = 6.0 GHz.

Figure 27.- Continued.

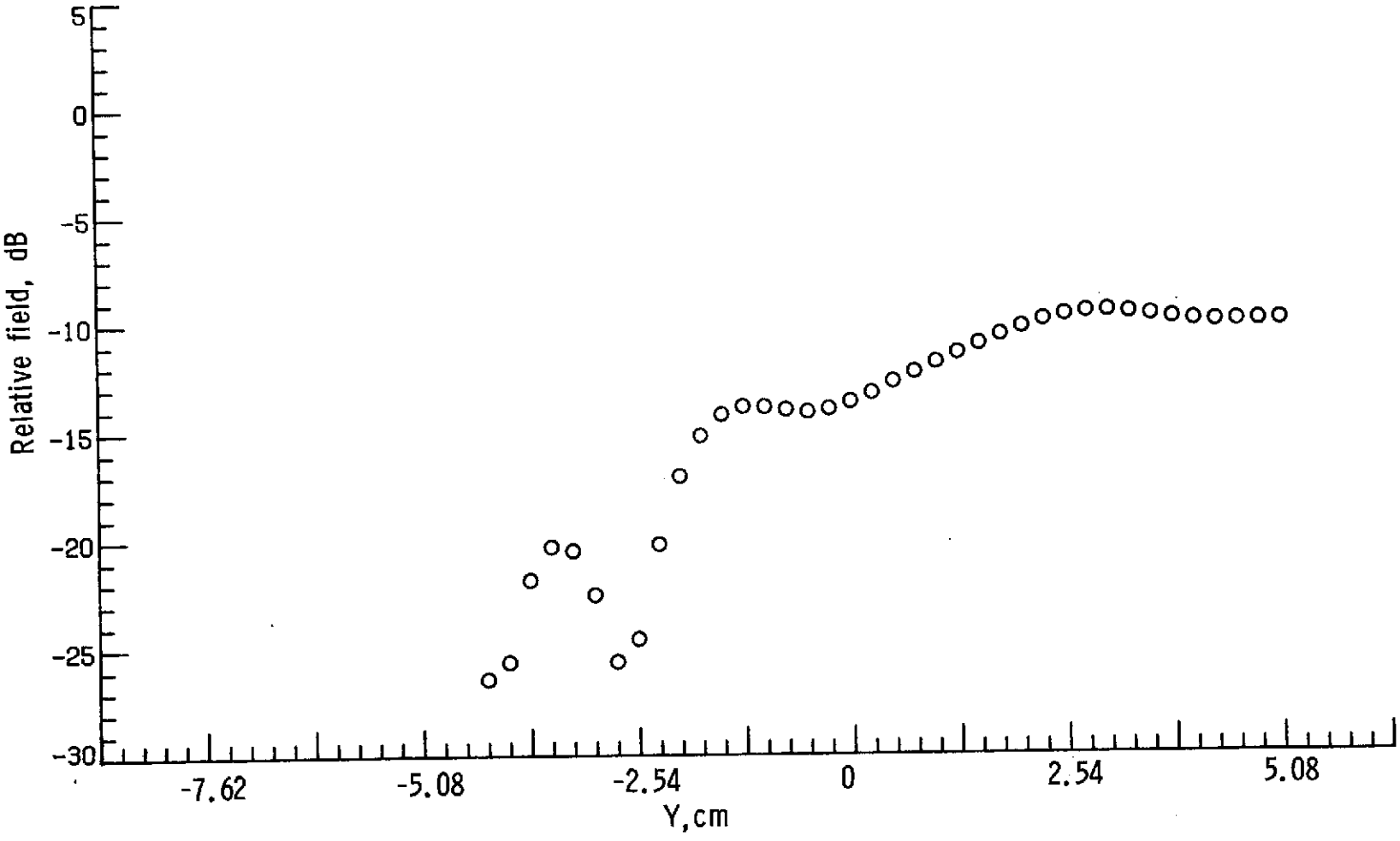

(c) Along the side at X = 3.048 cm, Z = 0.0 cm, and f = 6.0 GHz.

Figure 27.- Concluded.

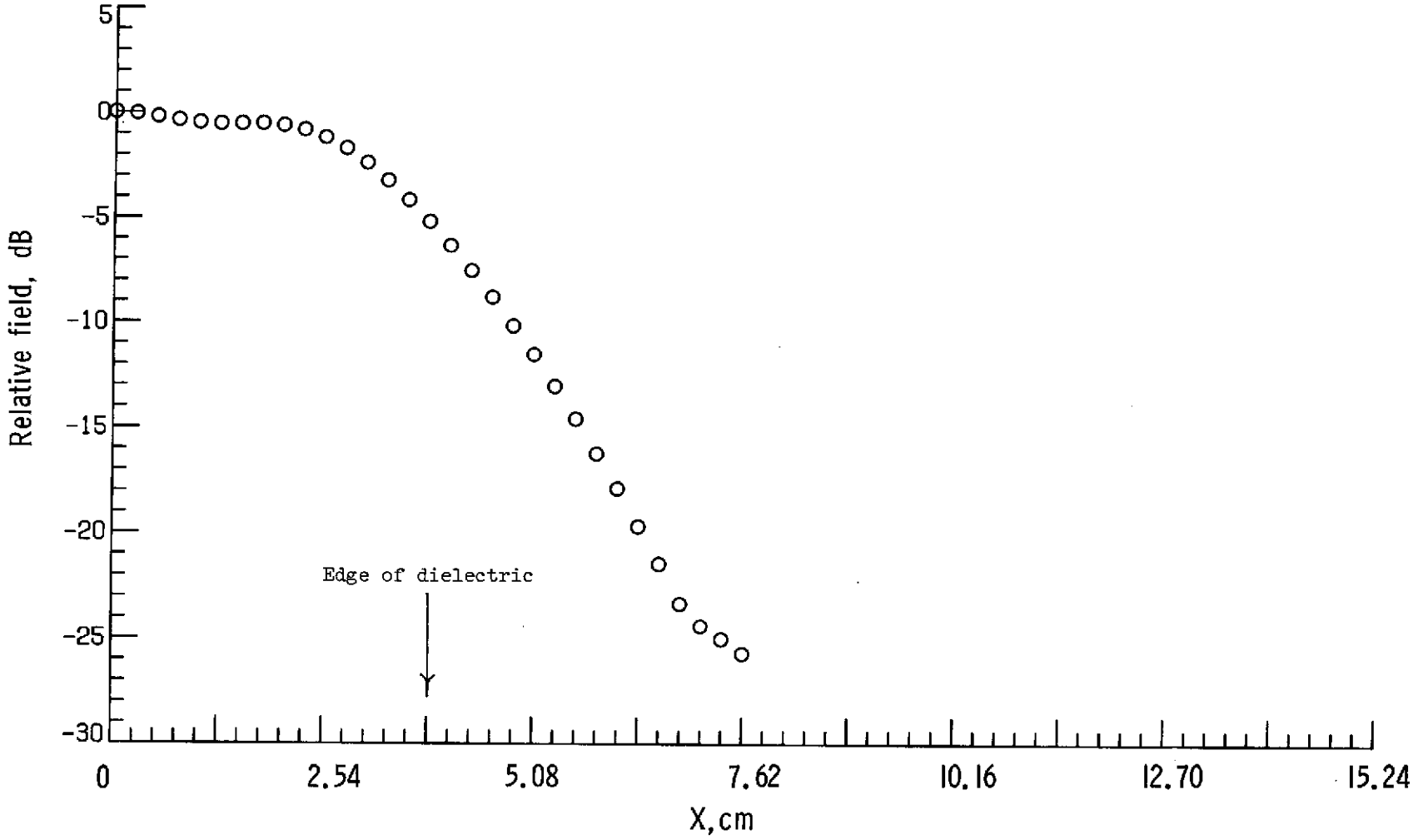

(a) E-plane at Y = 0.508 cm, X = 0.0 cm, and f = 6.0 GHz.

Figure 28.- Near-field amplitude measurement of a circular waveguide feeding a 7.62-cm Plexiglas sphere.

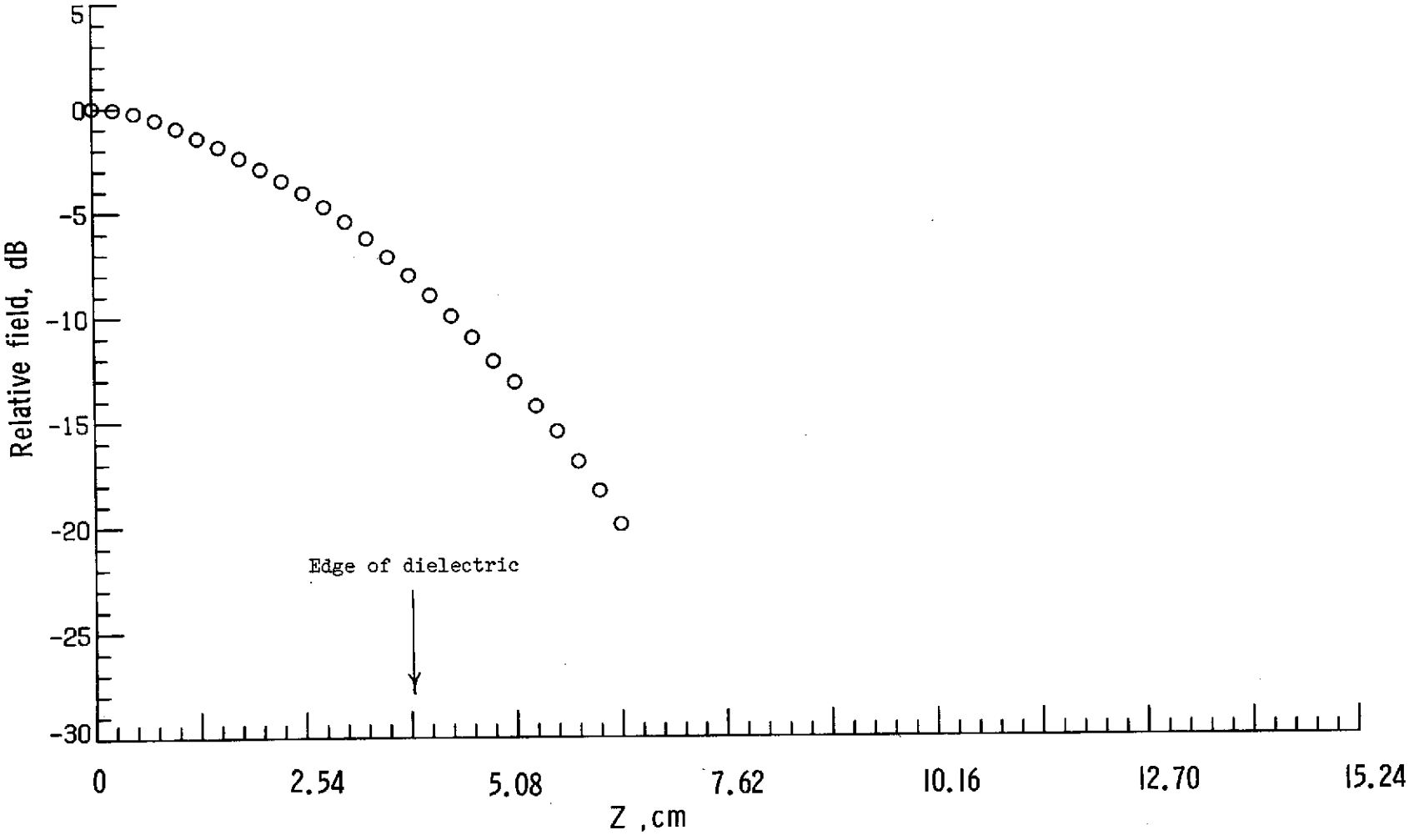

(b) H-plane at Y = 0.508 cm, X = 0.0 cm, and f = 6.0 GHz.

Figure 28.- Continued.

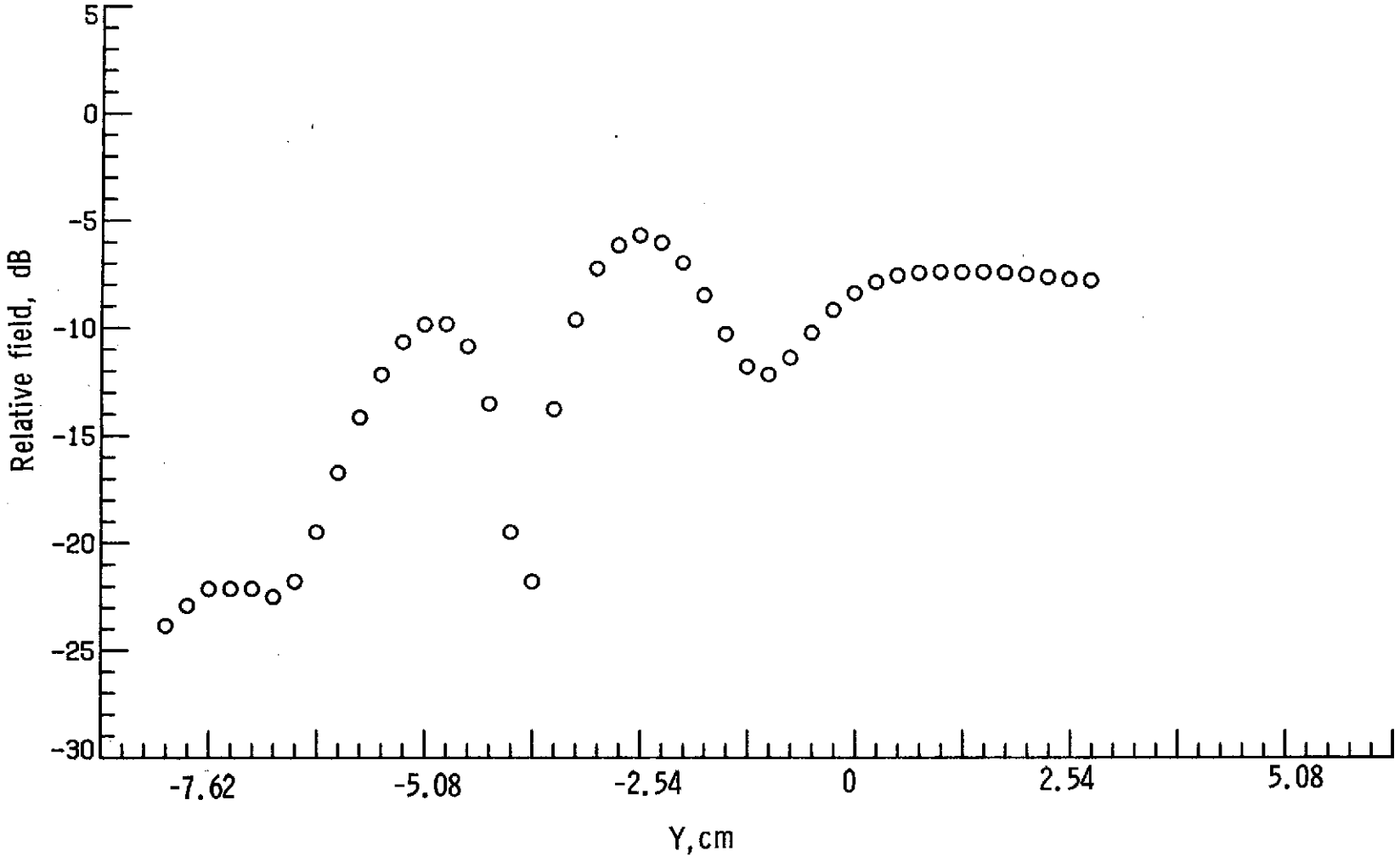

(c) Along the side at X = 4.318 cm, Z = 0.0 cm, and f = 6.0 GHz.

Figure 28.- Concluded.

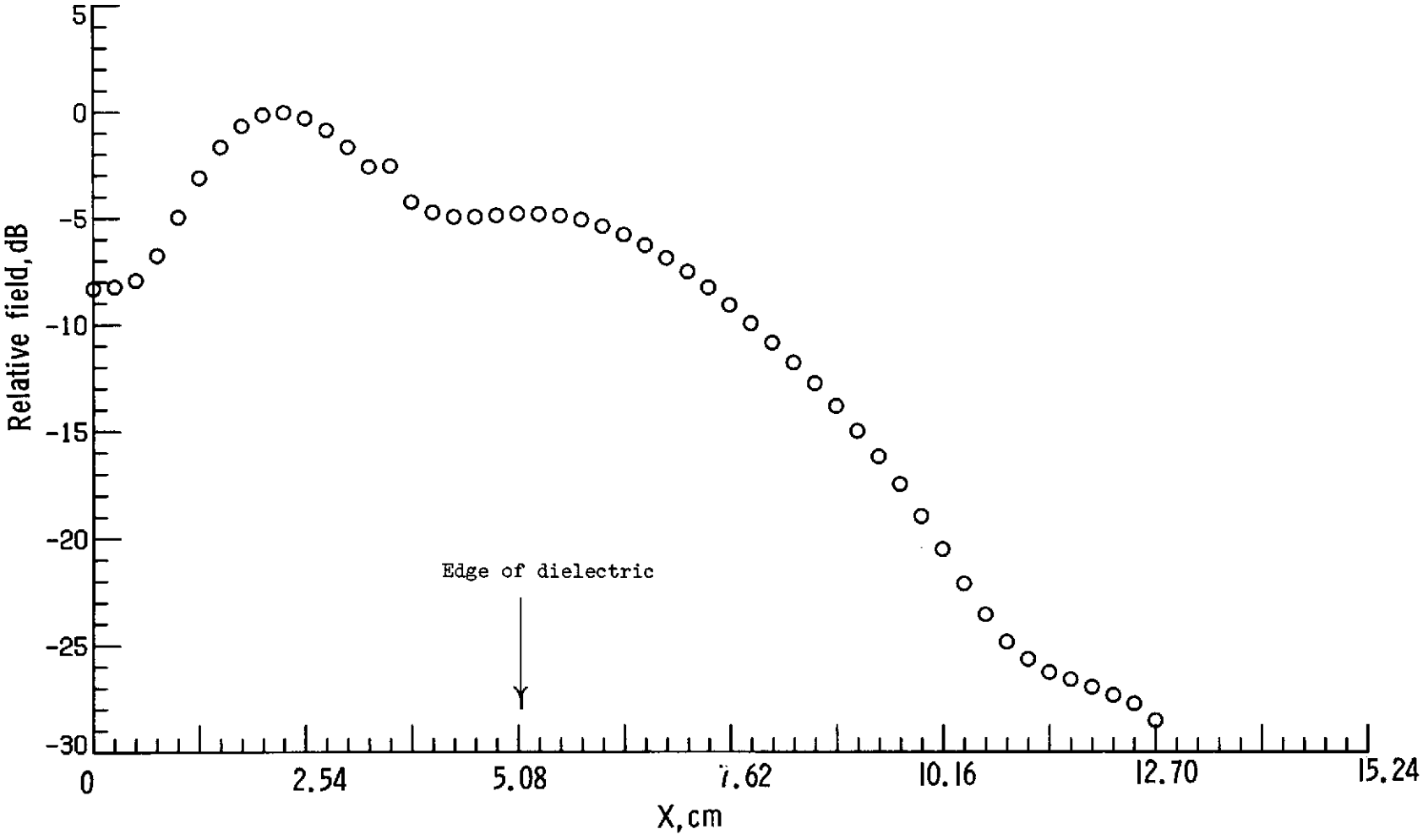

(a) E-plane at Y = 0.508 cm, Z = 0.0 cm, and f = 6.0 GHz.

Figure 29.- Near-field amplitude measurement of a circular waveguide feeding a 10.16-cm Plexiglas sphere.

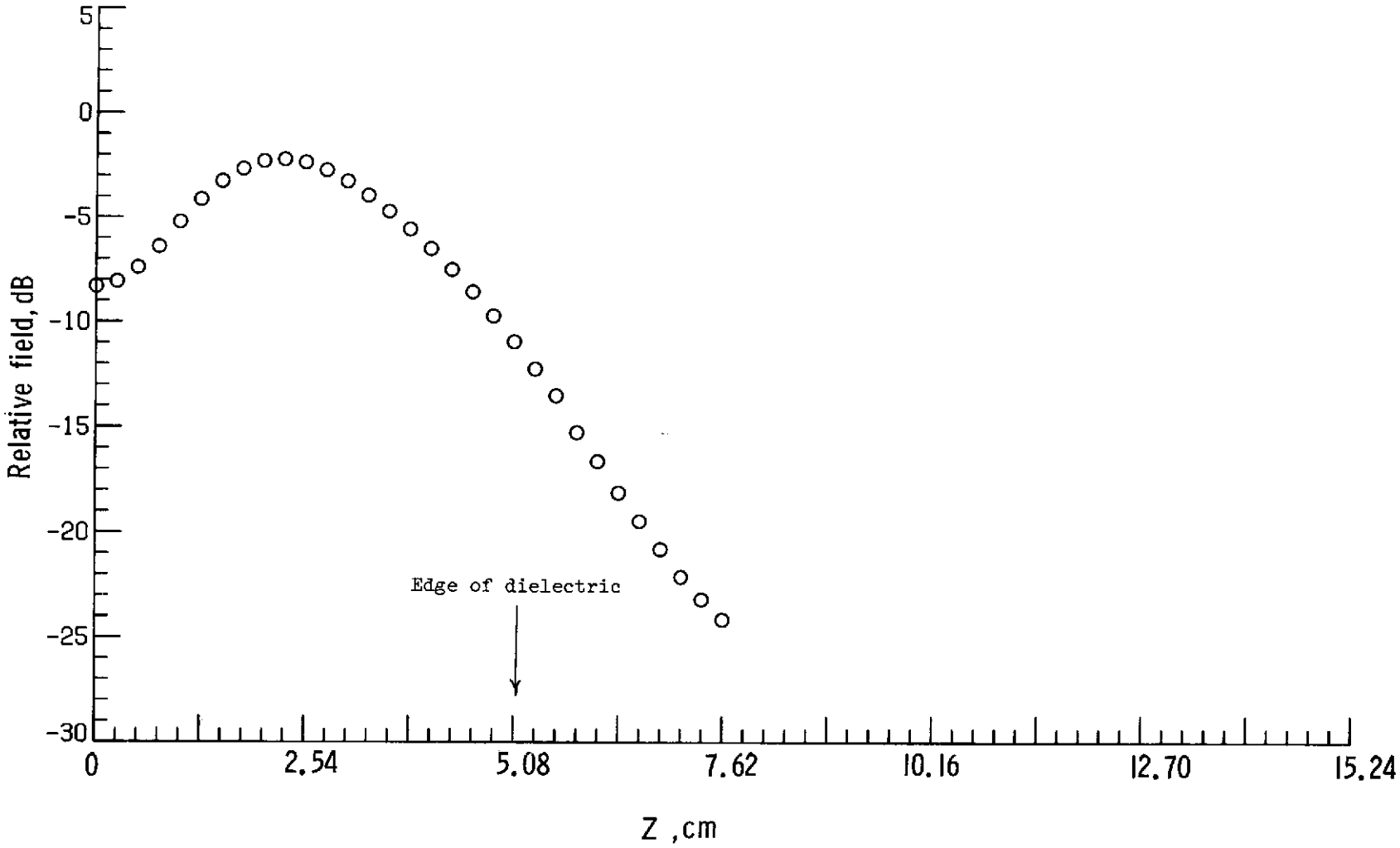

(b) H-plane at Y = 0.508 cm, X = 0.0 cm, and f = 6.0 GHz.

Figure 29.- Continued.

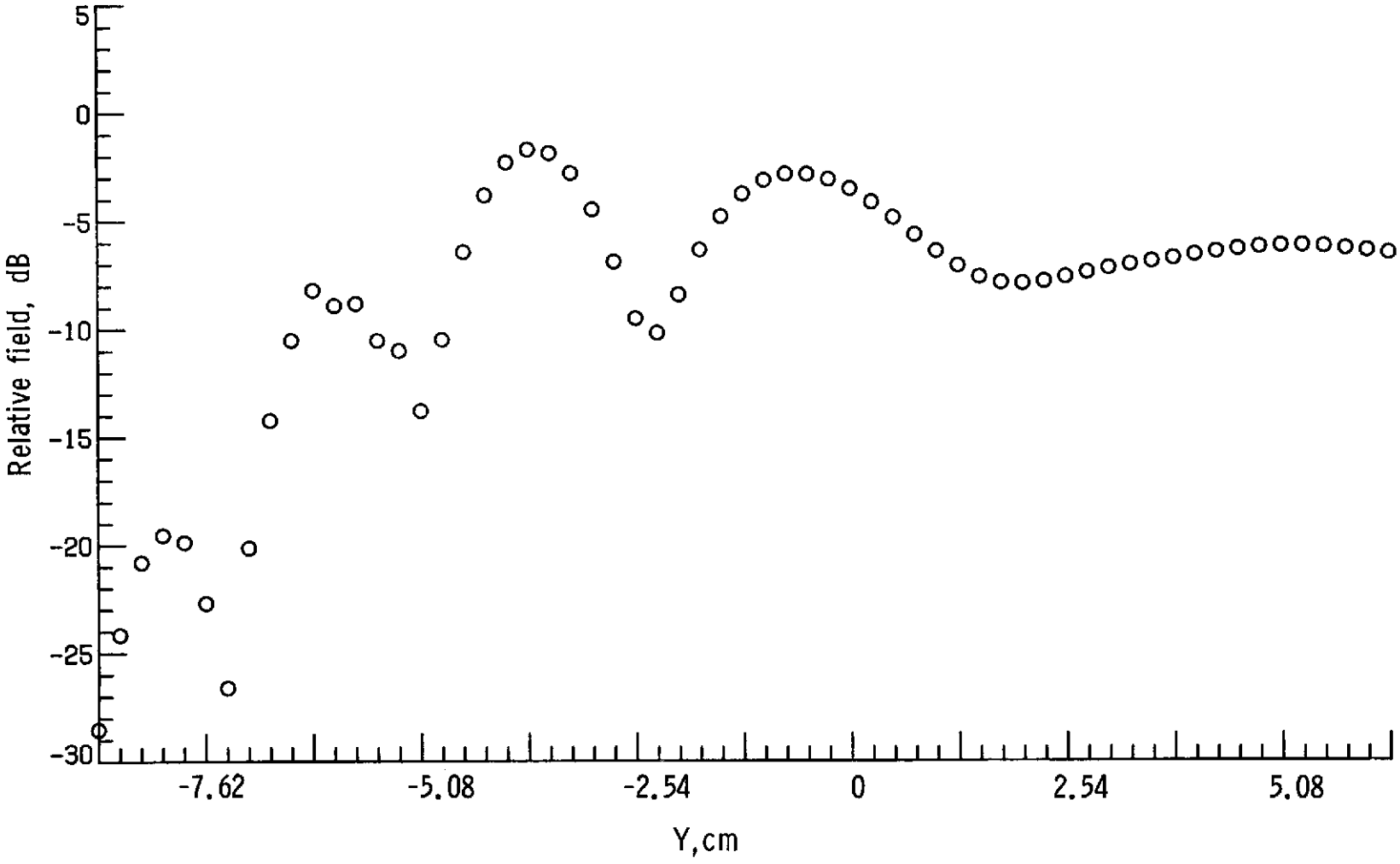

(c) Along the side at X = 5.588 cm, Z = 0.0 cm, and f = 6.0 GHz.

Figure 29.- Concluded.

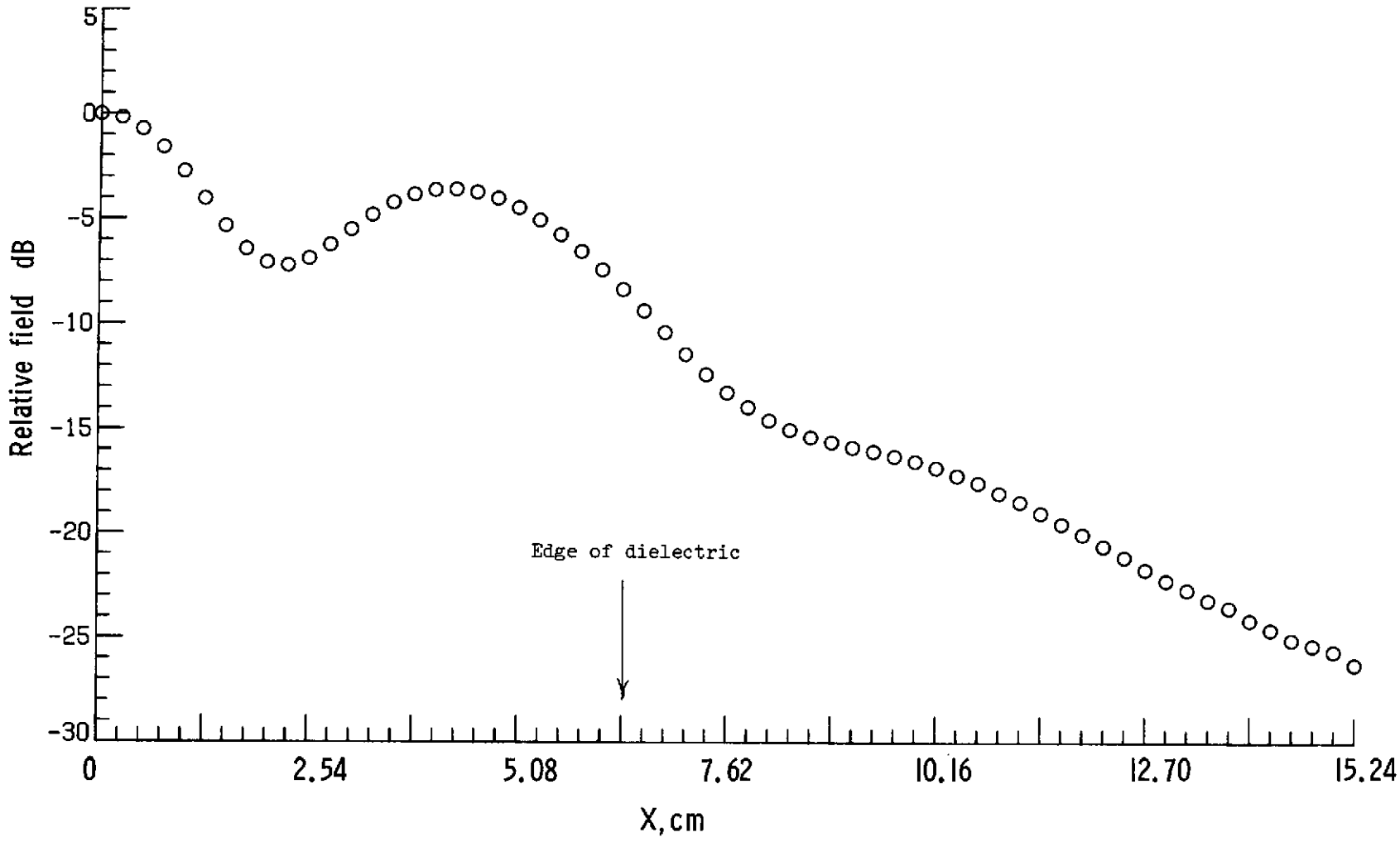

(a) E-plane at Y = 0.508 cm, Z = 0.0 cm, and f = 6.0 GHz.

Figure 30.- Near-field amplitude measurement of a circular waveguide feeding a 12.70-cm Plexiglas sphere.

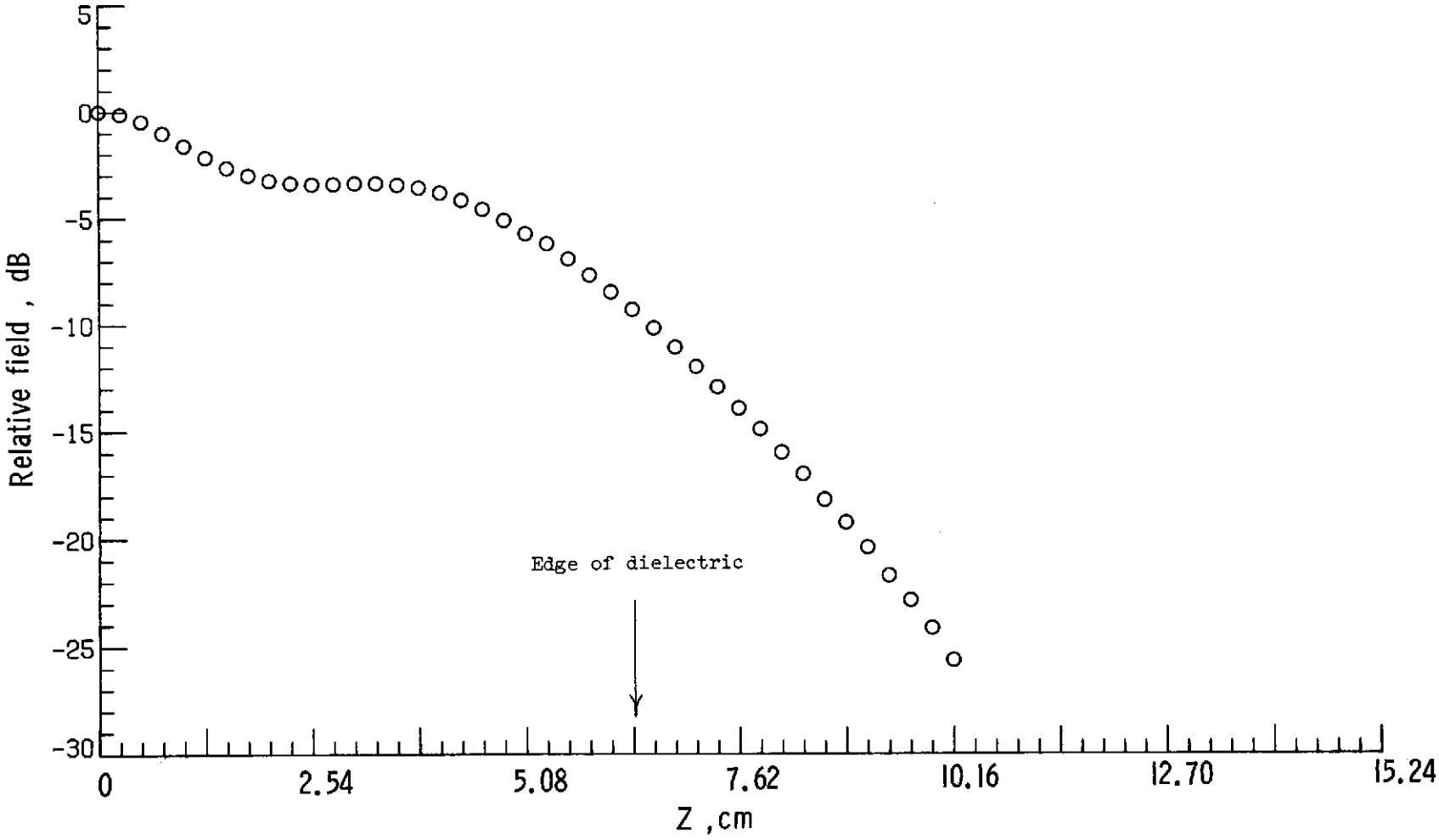

(b) H-plane at Y = 0.508 cm, X = 0.0 cm, and f = 6.0 GHz.

Figure 30.- Continued.

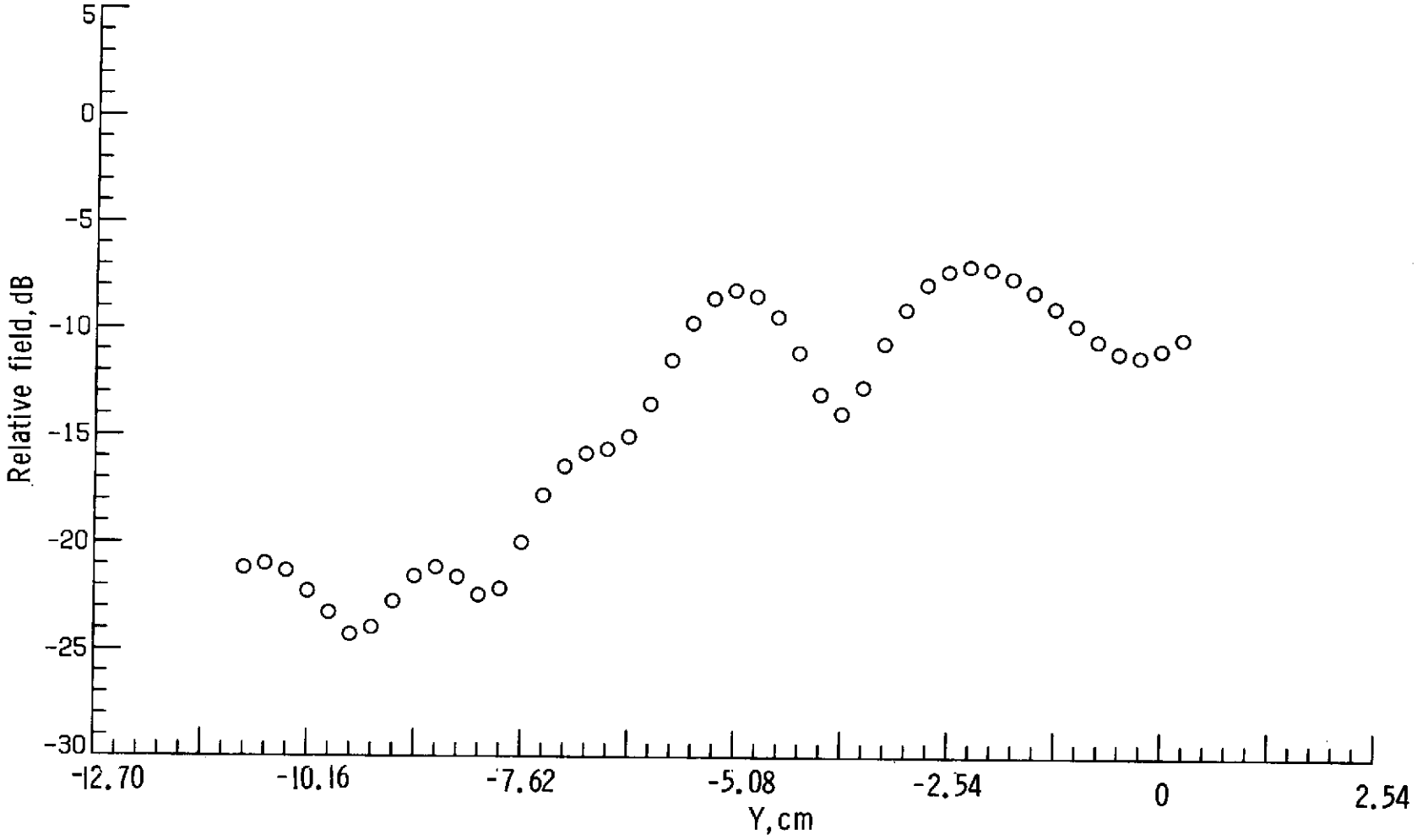

(c) Along the side at X = 6.858 cm, Z = 0.0 cm, and f = 6.0 GHz.

Figure 30.- Concluded.

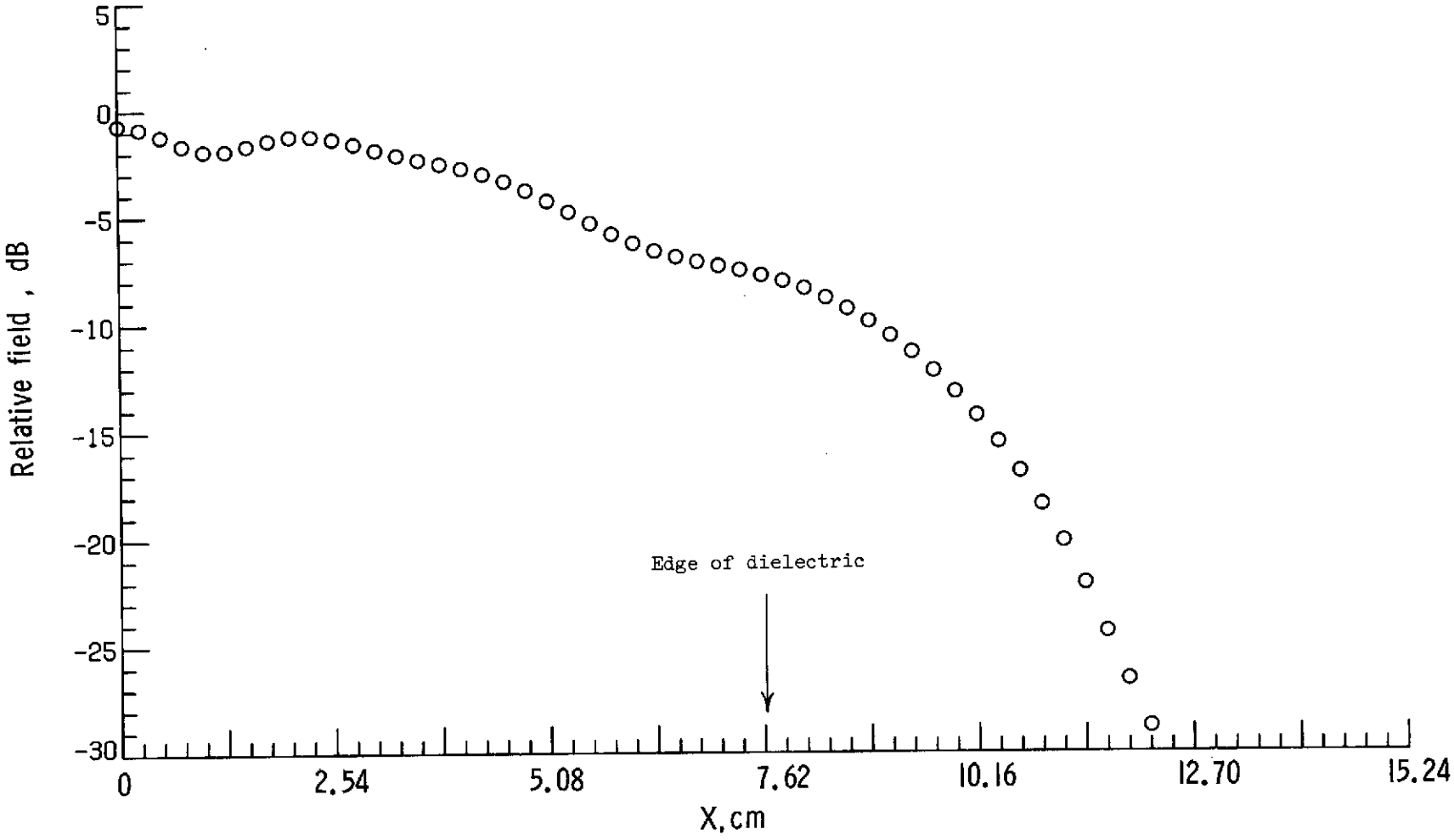

(a) E-plane at Y = 0.508 cm, Z = 0.0 cm, and f = 6.0 GHz.

Figure 31.- Near-field amplitude measurement of a circular waveguide feeding a 15.24-cm Plexiglas sphere.

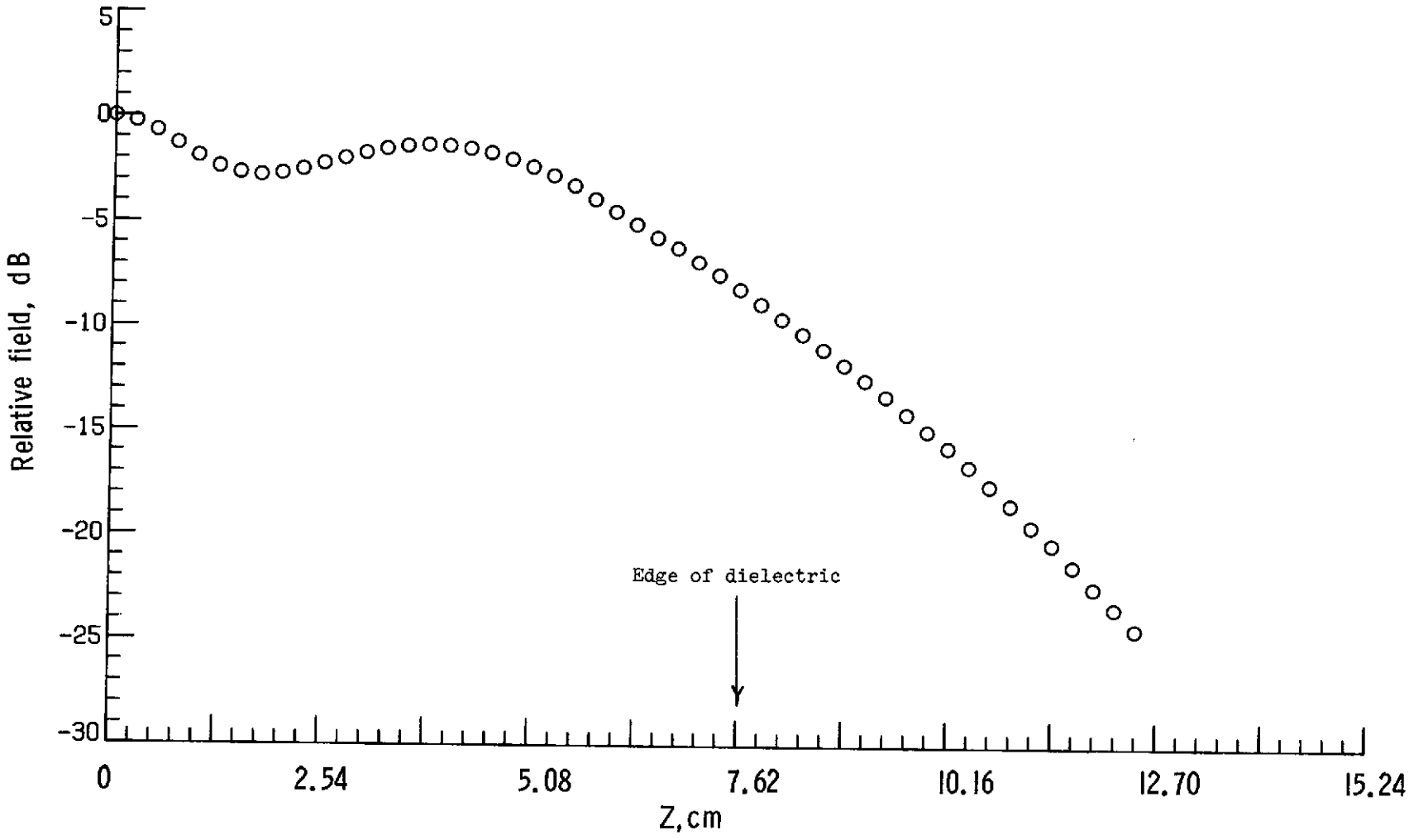

(b) H-plane at Y = 0.508 cm, X = 0.0 cm, and f = 6.0 GHz.

Figure 31.- Continued.

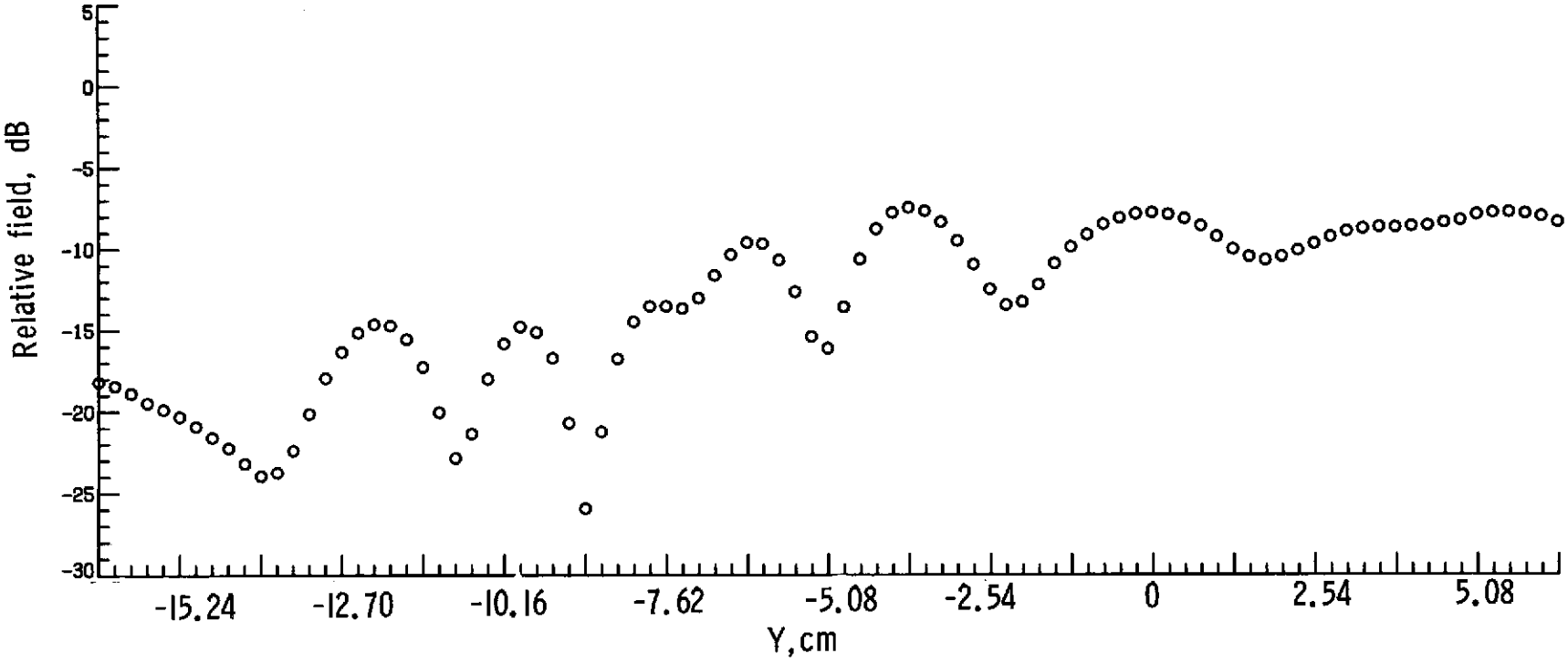

(c) Along the side at X = 8.128 cm, Z = 0.0 cm, and f = 6.0 GHz.

Figure 31.- Concluded.

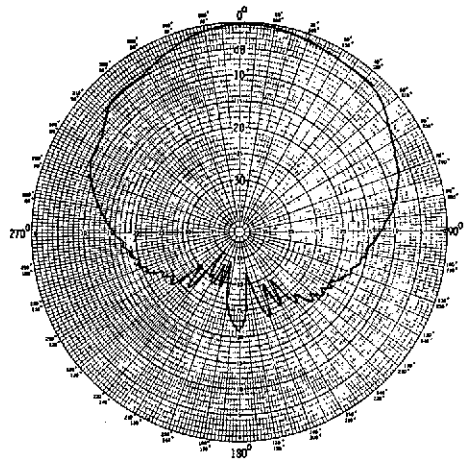

(a) E-plane; 0.95λ.

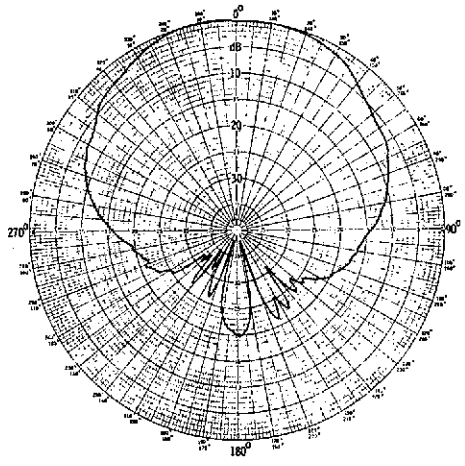

(b) E-plane; 2.22λ.

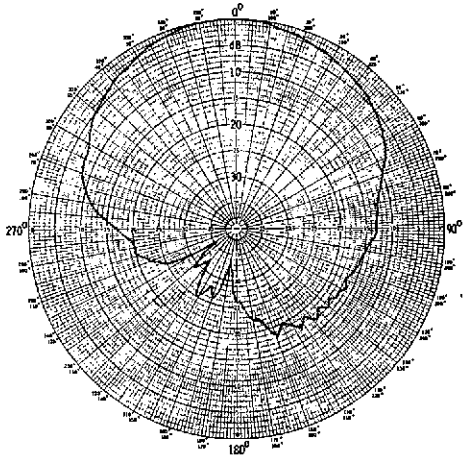

(c) E-plane; 6.03λ.

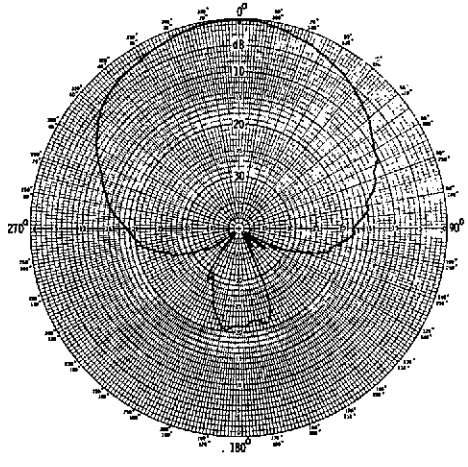

(d) H-plane; 0.95λ.

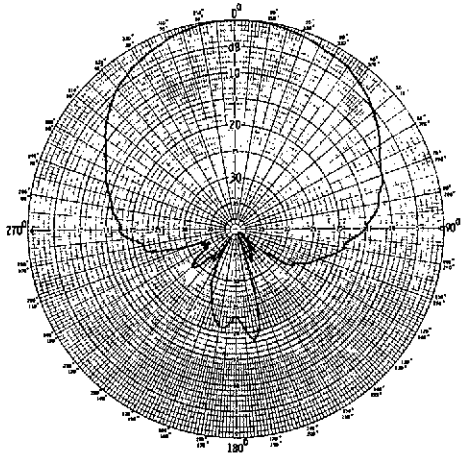

(e) H-plane; 2.22λ.

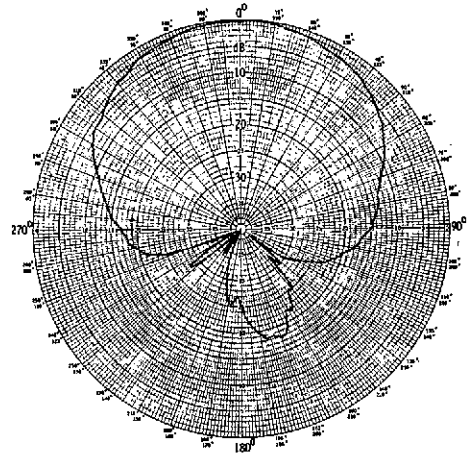

(f) H-plane; 6.03λ.

Figure 32.- Radiation pattern of a circular waveguide antenna radiating in the presence of an identical antenna, operating at a frequency of 5.0 GHz and at various center-to-center spacings. (The active antenna is on the 270° side of the pattern.)

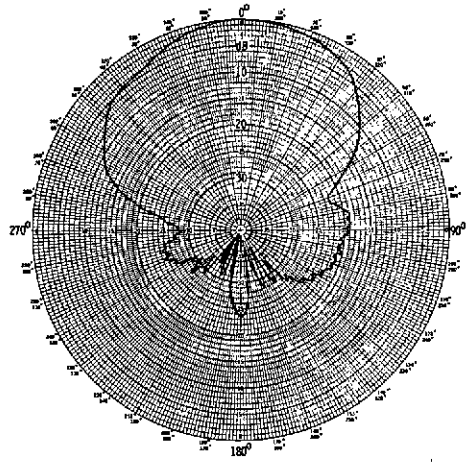

(a) E-plane; 0.95λ.

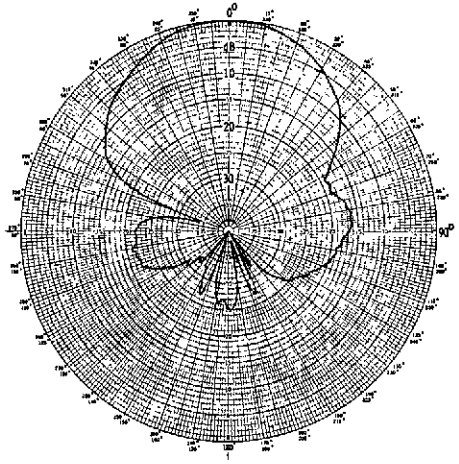

(b) E-plane; 2.22λ.

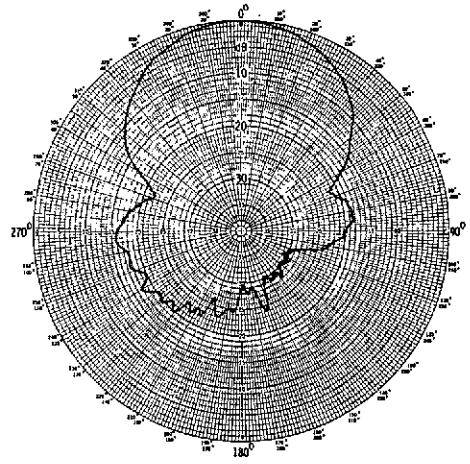

(c) E-plane; 6.03λ.

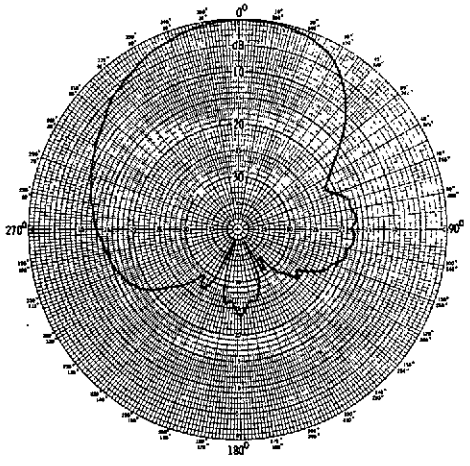

(d) H-plane; 0.95λ.

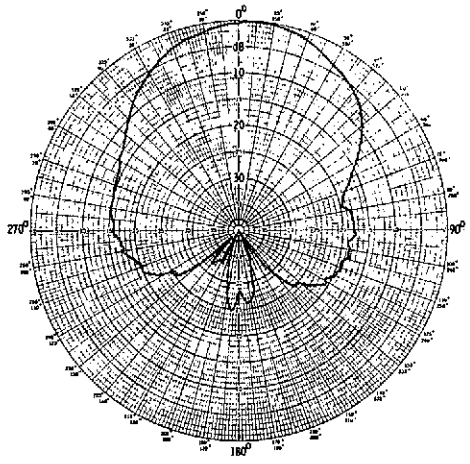

(e) H-plane; 2.22λ.

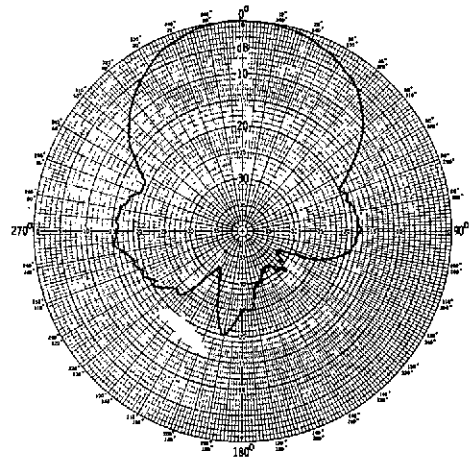

(f) H-plane; 6.03λ.

Figure 33.- Radiation pattern of a circular waveguide antenna loaded with a 5.08-cm Plexiglas sphere radiating in the presence of an identical loaded antenna, operating at f = 5.0 GHz, and at several center-to-center spacings. (The active antenna is on the 270° side for 0.95λ and 2.22λ and on the 90° side for 6.03λ.)

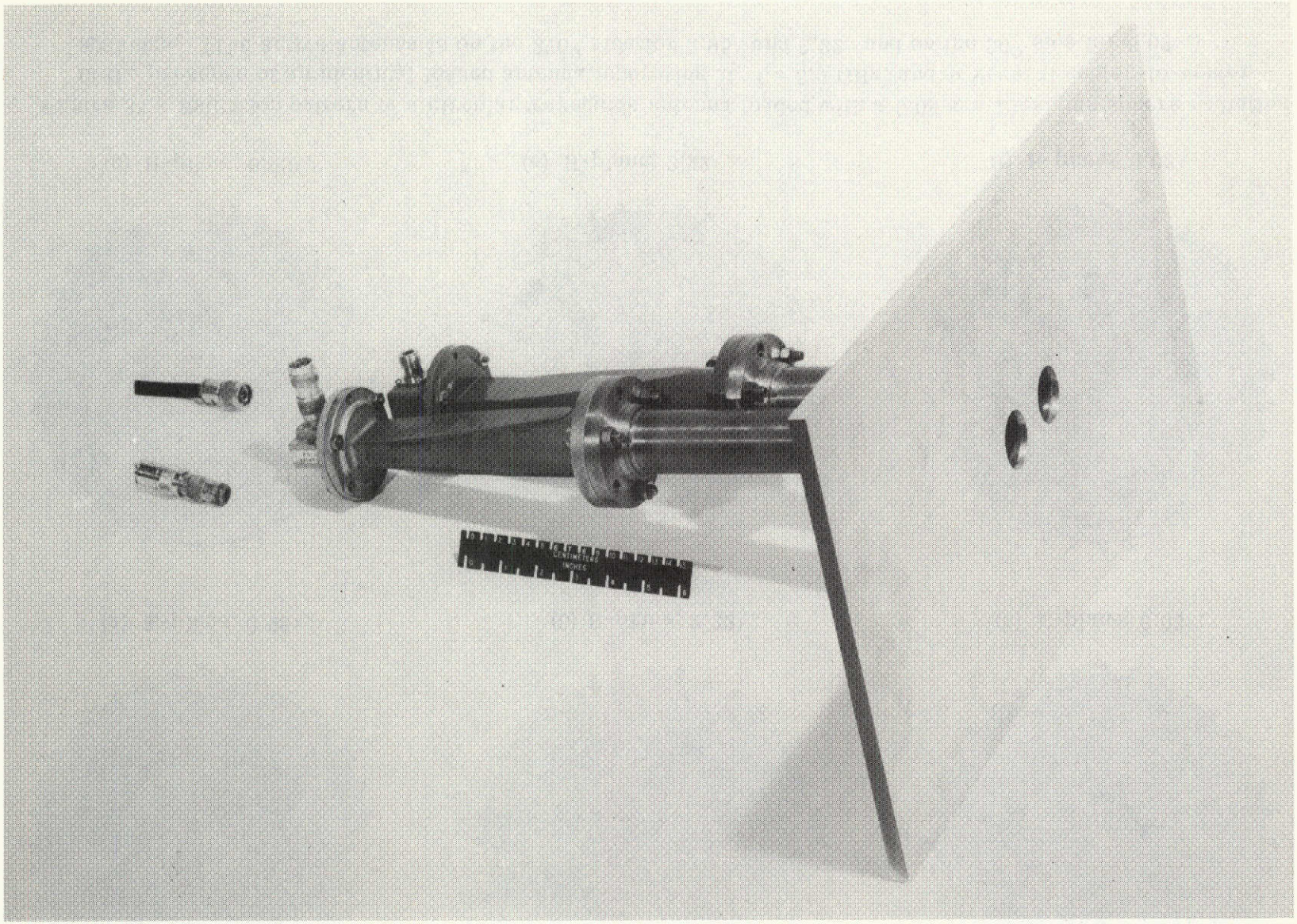

L-72-7617

Figure 34.- Photograph of a pair of circular waveguides located in a ground plane which were used for coupling measurements.

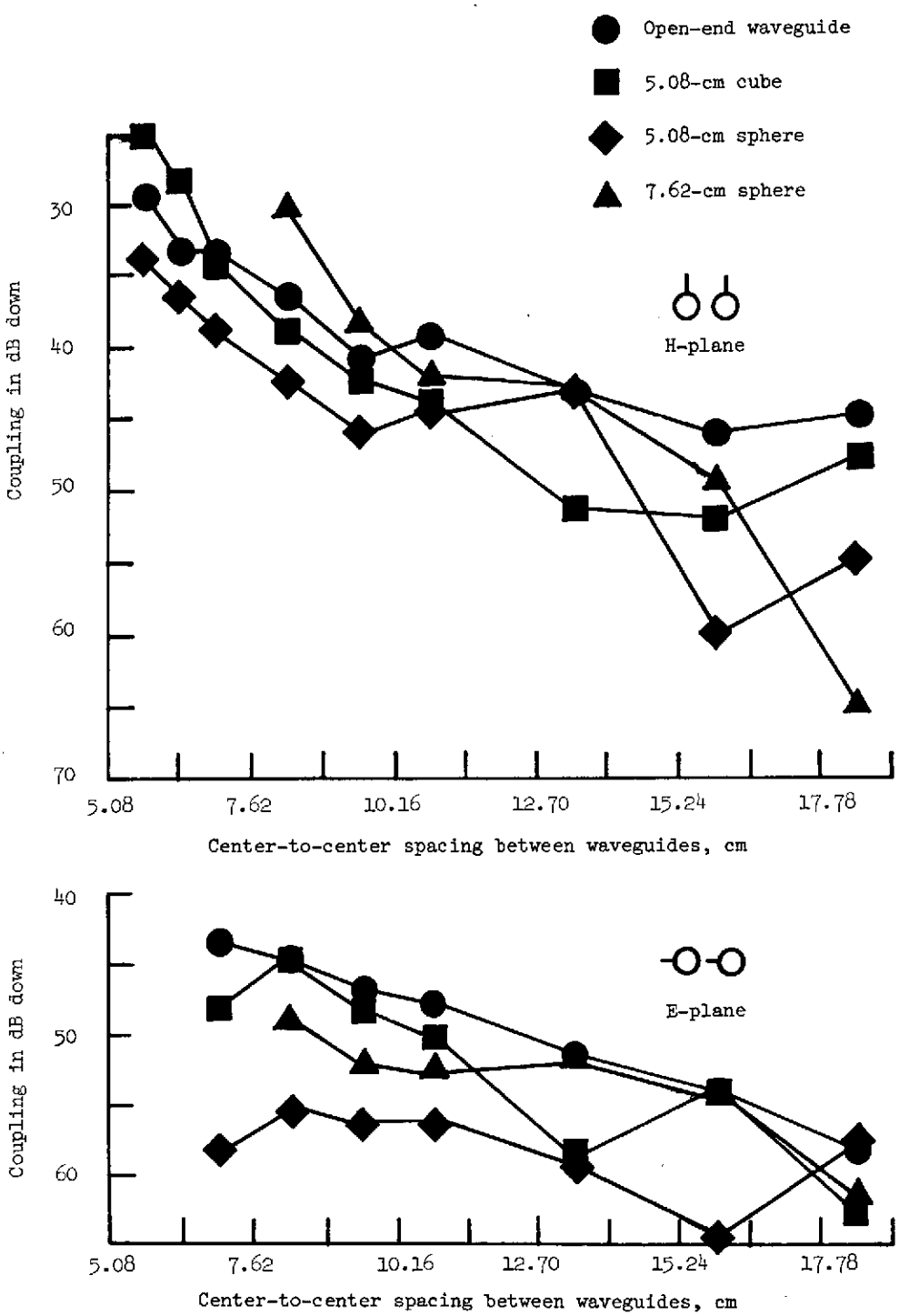

Figure 35.- Coupling between a pair of C-band circular waveguides loaded with dielectric objects for two alinements of the electric field; f = 5.8 GHz.

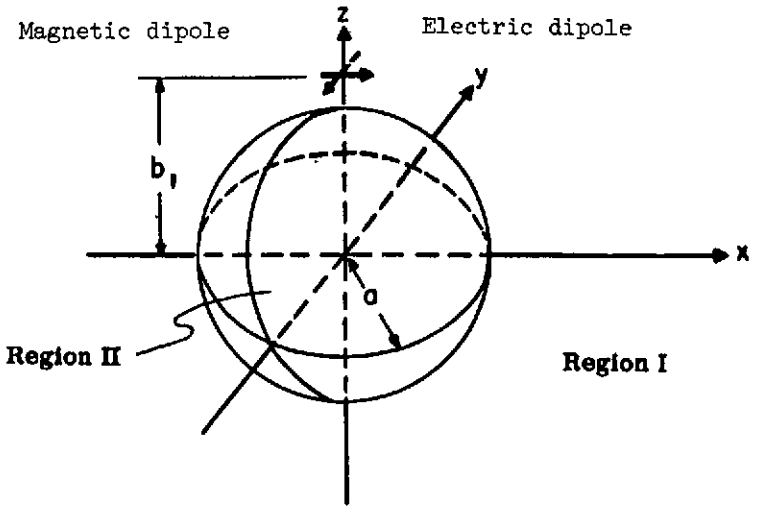

Figure 36.- Geometry for a Huygens' source in the presence of a dielectric sphere.

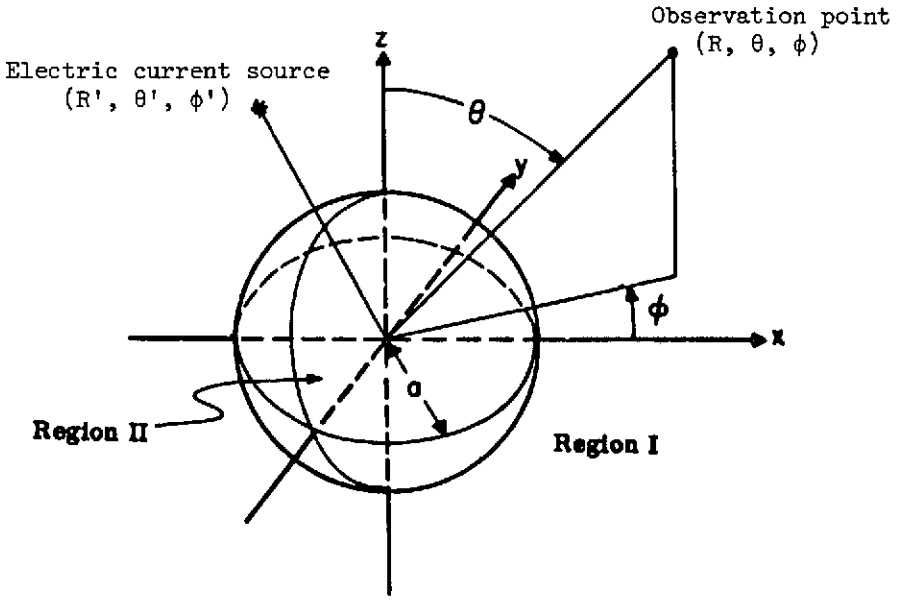

Figure 37.- Geometry for a current source in the presence of a dielectric sphere.

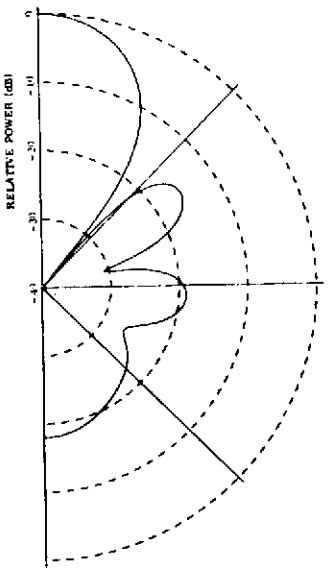

(a) 7.62-cm sphere at 5.0 GHz; E-plane; D = 1.27λ.

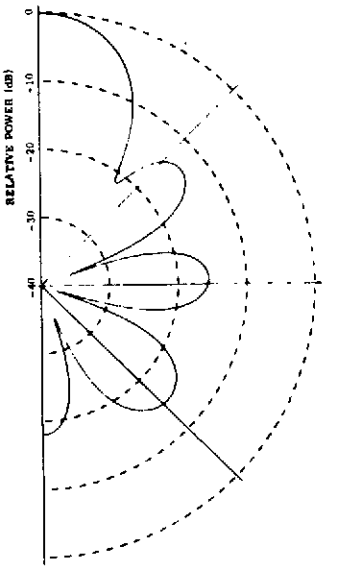

(b) 7.62-cm sphere at 5.0 GHz; H-plane; D = 1.27λ.

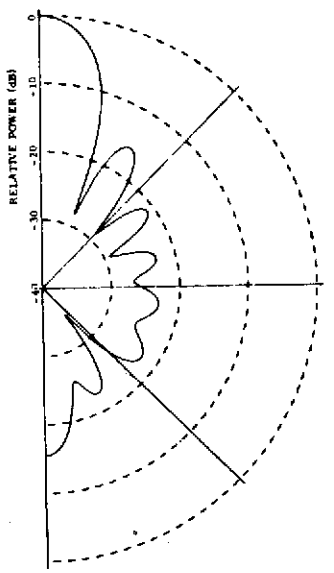

(c) 12.7-cm sphere at 5.0 GHz; E-plane; D = 2.12λ.

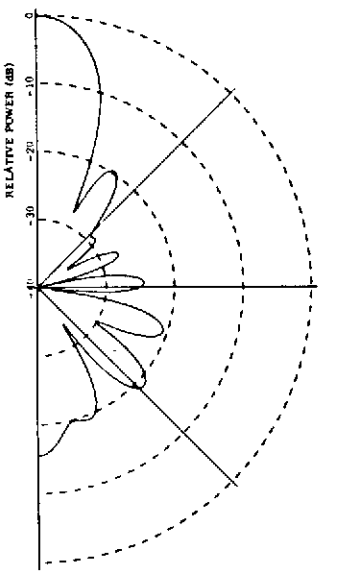

(d) 12.7-cm sphere at 5.0 GHz; H-plane; D = 2.12λ.

Figure 38.- Calculated radiation patterns using a Huygens' source on the surface of a Plexiglas sphere.

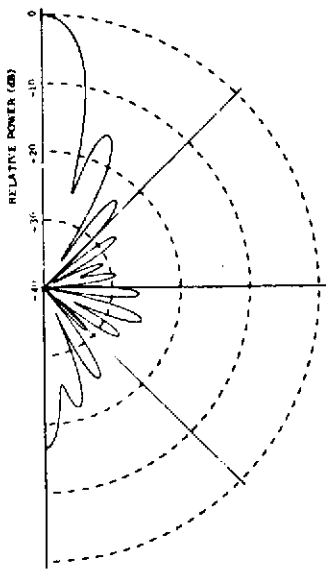

(e) 7.62-cm sphere at 8.0 GHz; E-plane; D = 3.39λ.

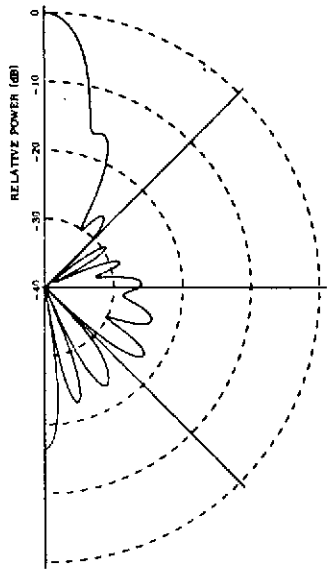

(f) 7.62-cm sphere at 8.0 GHz; H-plane; D = 3.39λ.

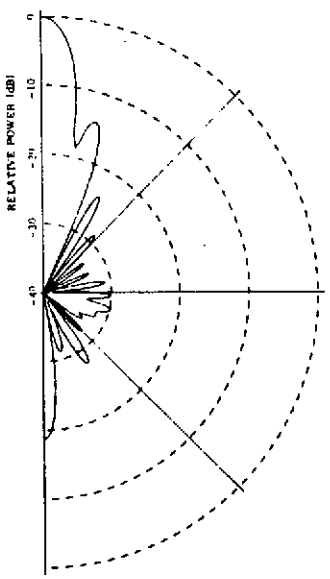

(g) 7.62-cm sphere at 10.0 GHz; E-plane; D = 4.23λ.

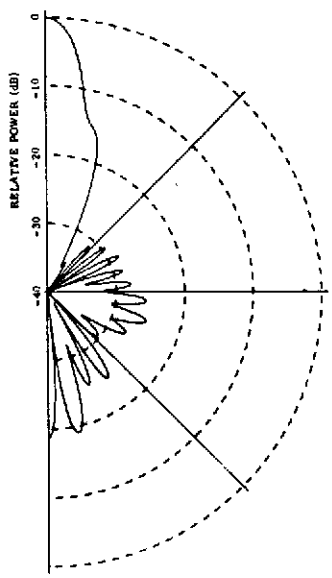

(h) 7.62-cm sphere at 10.0 GHz; H-plane; D = 4.23λ.

Figure 38.- Concluded.

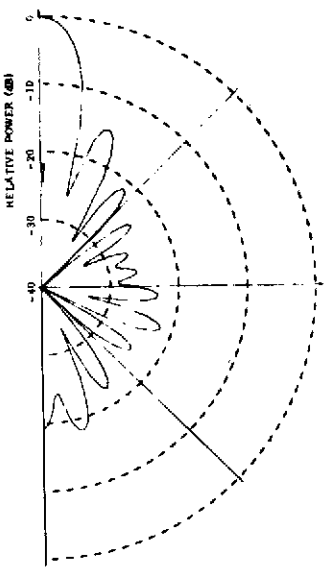

(a) E-plane; $b_1/a = 1.0$.

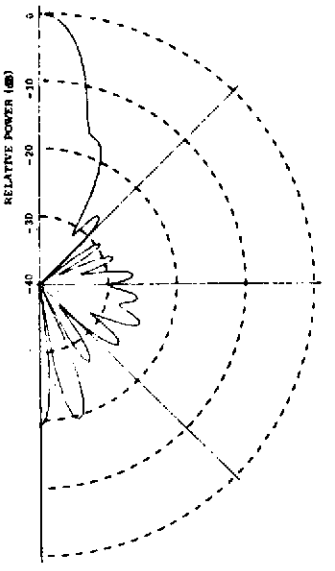

(b) H-plane; $b_1/a = 1.0$.

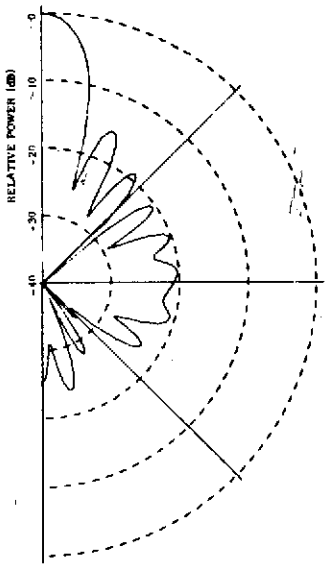

(c) E-plane; $b_1/a = 1.15$.

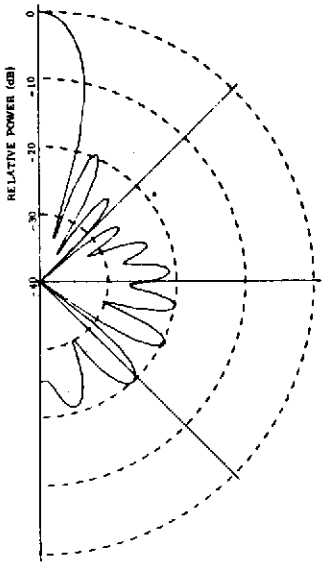

(d) H-plane; $b_1/a = 1.15$.

Figure 39.- Radiation patterns for a source located outside the sphere.
$D = 3.39\lambda$; $\epsilon_r = 2.57$; $\tan \delta = 0.0065$.

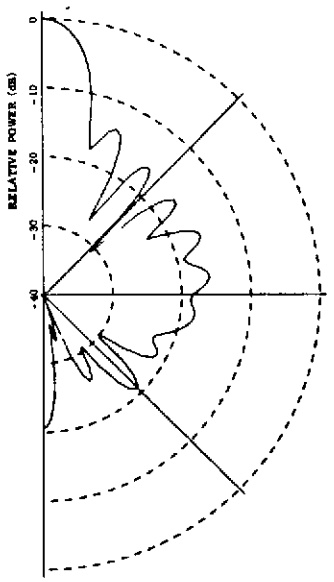

(e) E-plane; $b_1/a = 1.29$.

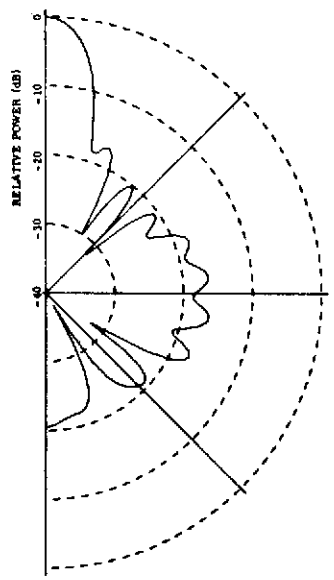

(f) H-plane; $b_1/a = 1.29$.

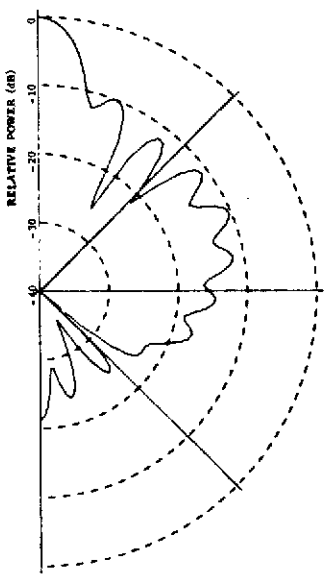

(g) E-plane; $b_1/a = 1.59$.

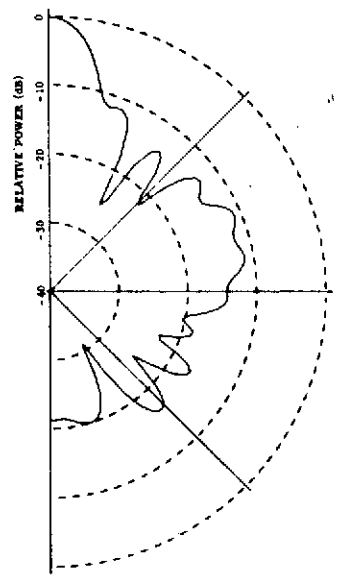

(h) H-plane; $b_1/a = 1.59$.

Figure 39.- Concluded.

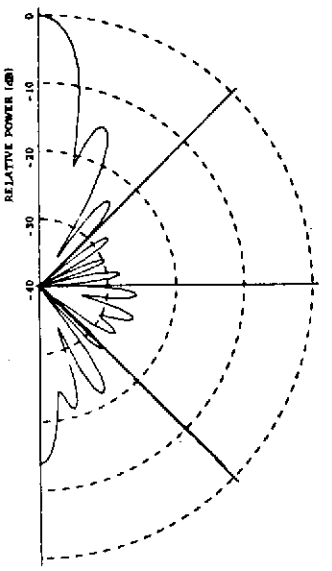

(a) E-plane; $b_1/a = 0.94$.

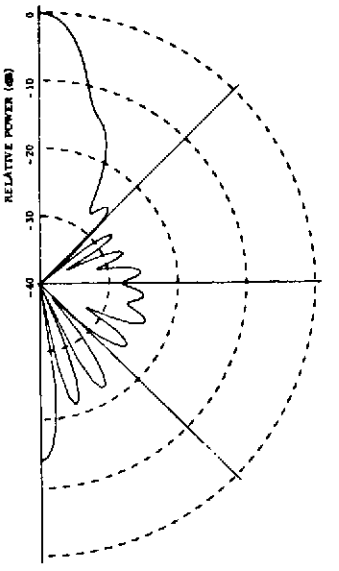

(b) H-plane; $b_1/a = 0.94$.

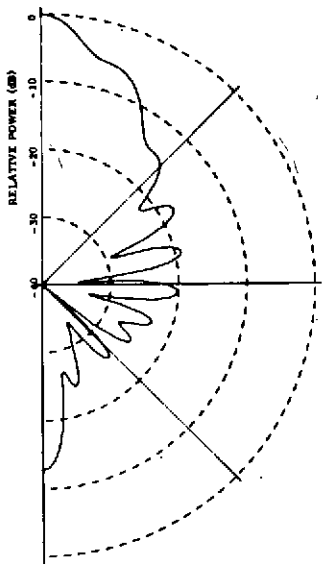

(c) E-plane; $b_1/a = 0.71$.

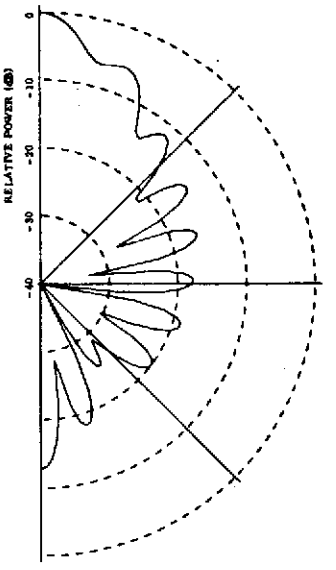

(d) H-plane; $b_1/a = 0.71$.

Figure 40.- Radiation patterns for a source located inside the sphere. $D = 3.39\lambda$; $\epsilon_r = 2.57$; $\tan \delta = 0.0065$.

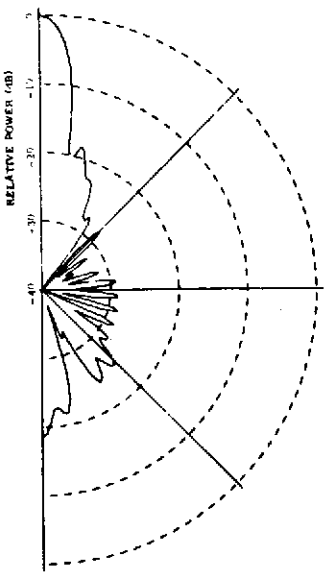

(a) E-plane; $\epsilon_r = 6.0$; $b_1/a = 0.60$.

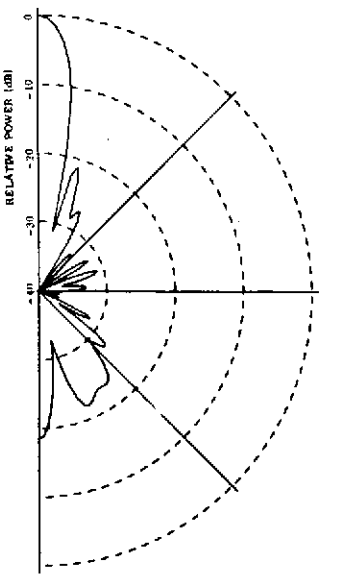

(b) H-plane; $\epsilon_r = 6.0$; $b_1/a = 0.60$.

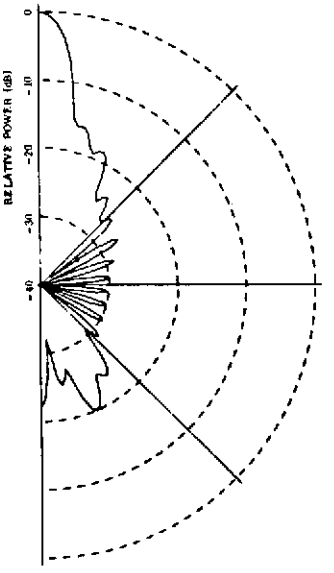

(c) E-plane; $\epsilon_r = 9.0$; $b_1/a = 0.40$.

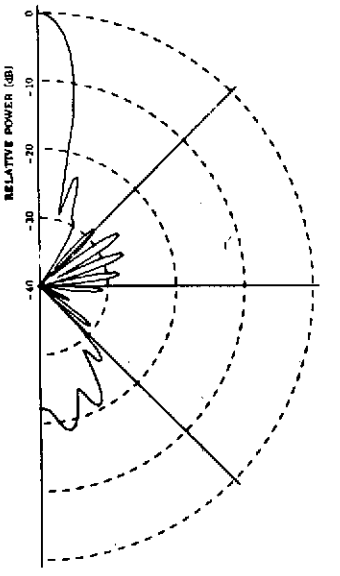

(d) H-plane; $\epsilon_r = 9.0$; $b_1/a = 0.40$.

Figure 41.- Radiation patterns for a Huygens' source located inside the sphere. $D = 4.46\lambda$; $\tan \delta = 0.0065$.

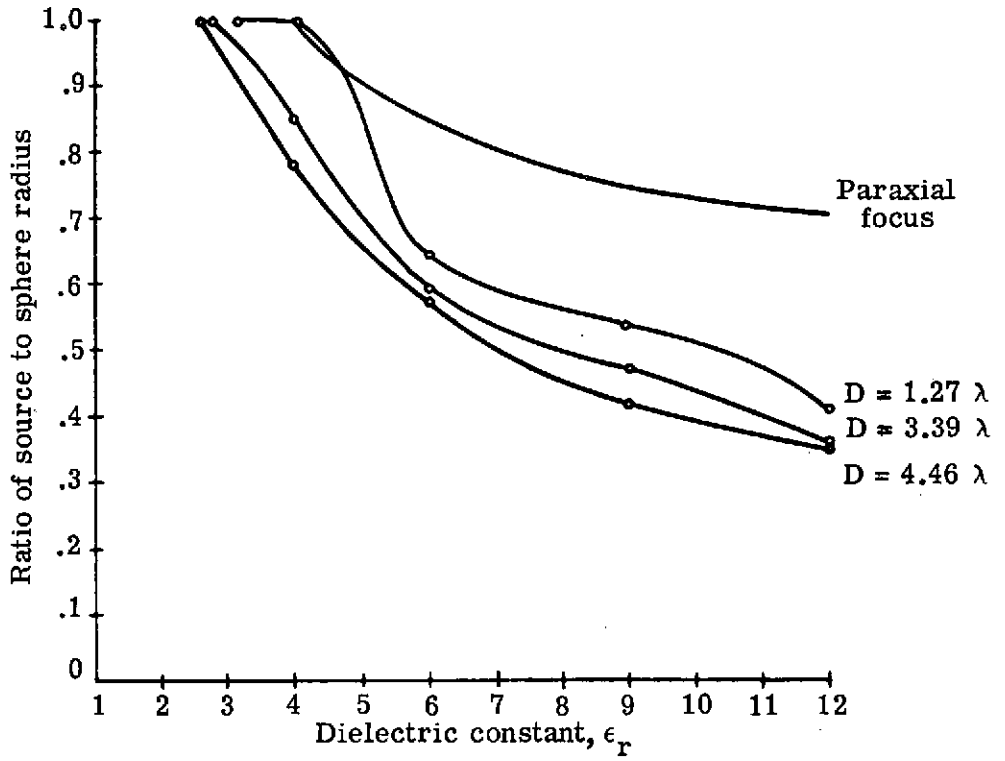

Figure 42.- Source location as a function of dielectric constant for optimum directivity.

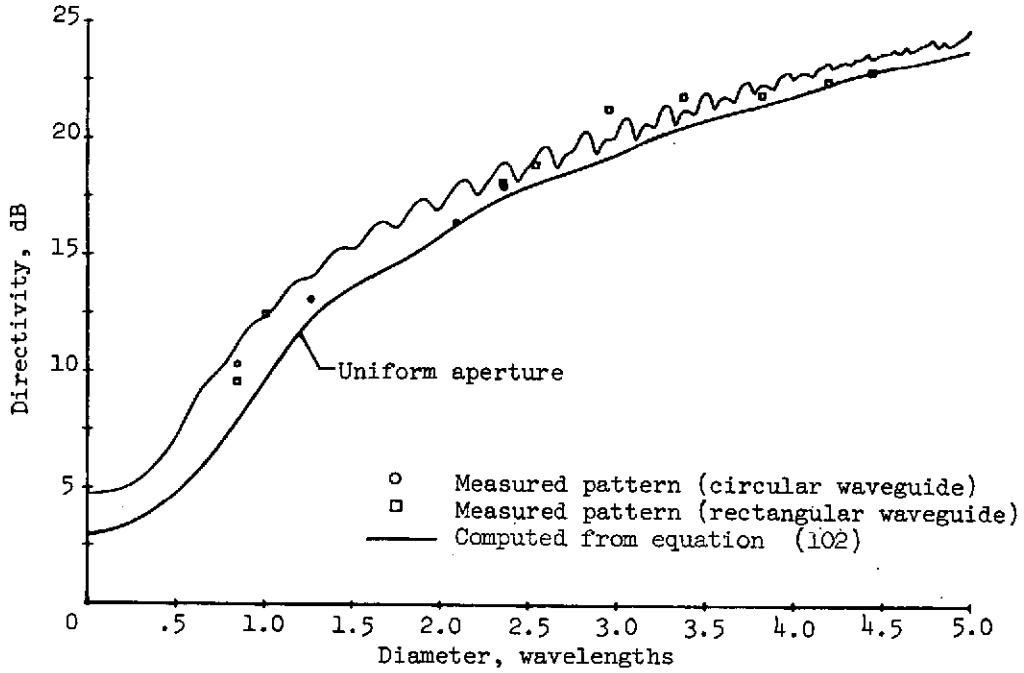

Figure 43.- Directivity of the Plexiglas sphere. $\epsilon_r = 2.57$; $\tan \delta = 0.0065$.

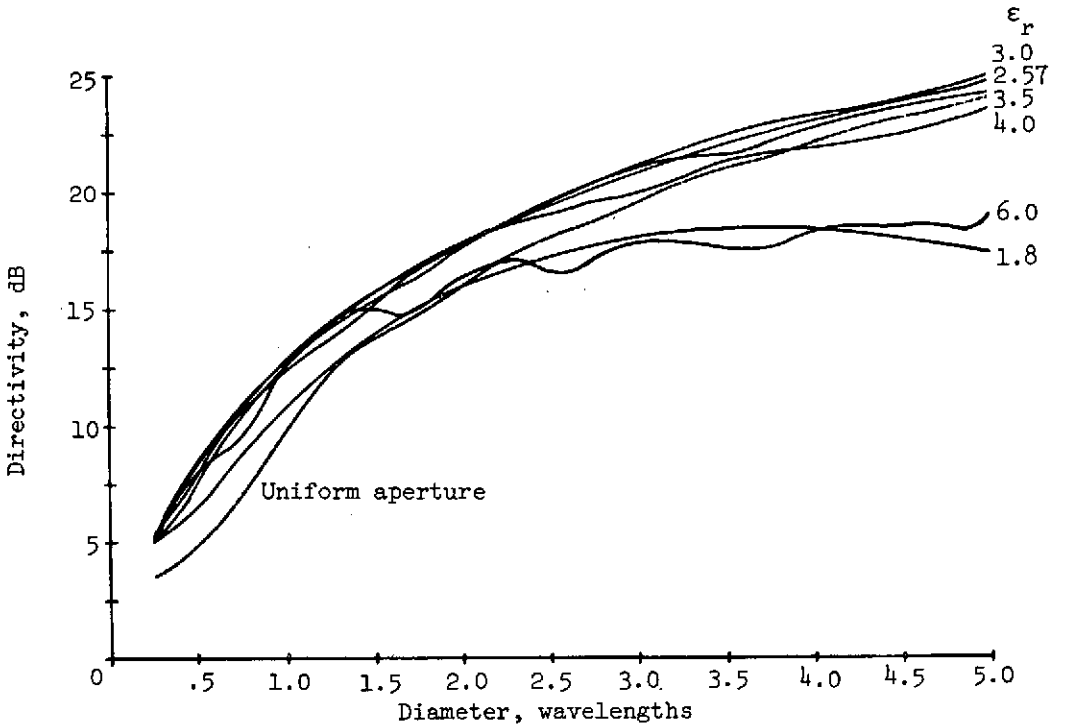

Figure 44.- Directivity of spheres with $\tan \delta = 0.0065$ for a range of dielectric constants.

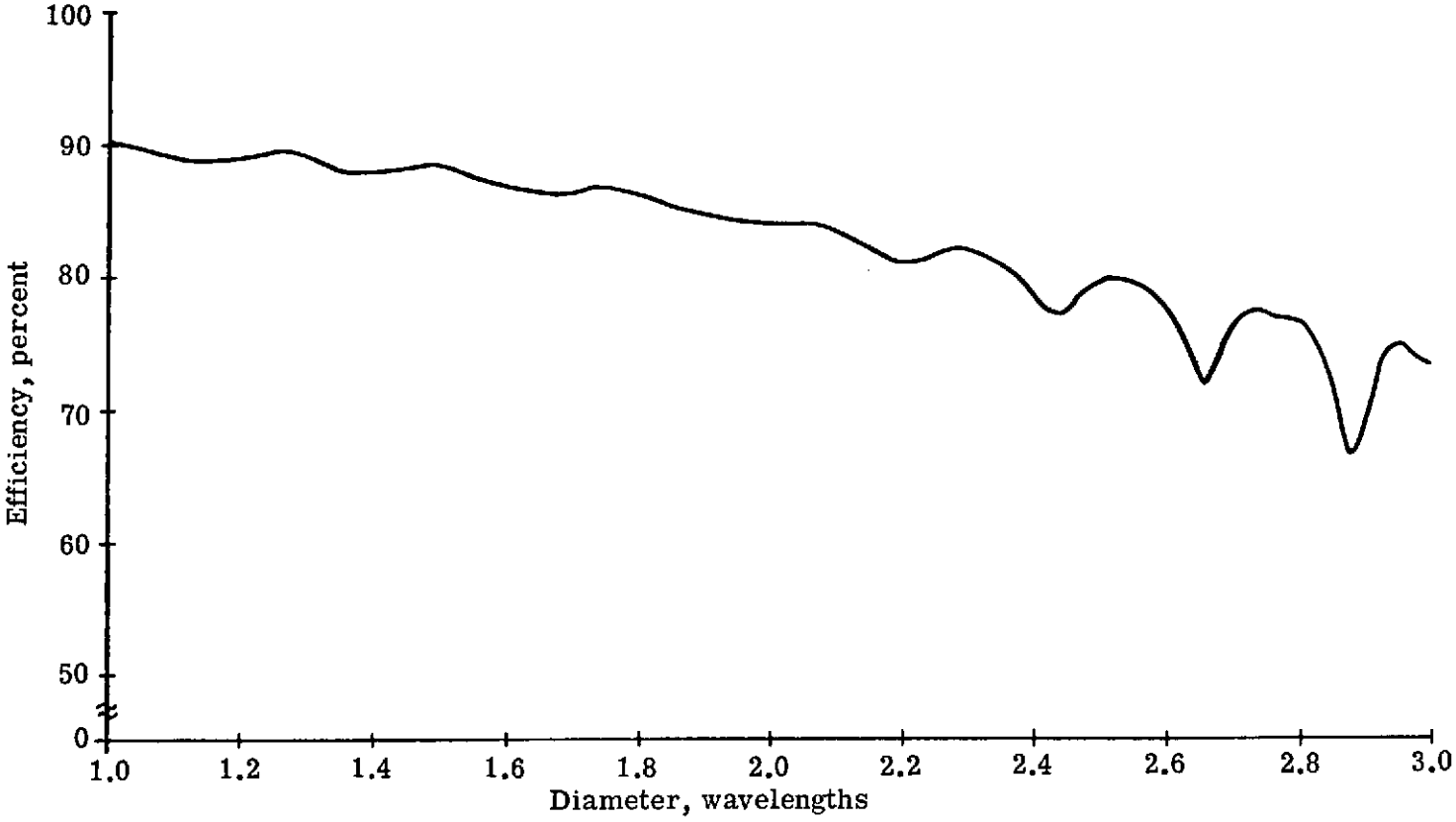

Figure 45.- Calculated antenna efficiency of the Huygens' source near a Plexiglas sphere. $\epsilon_r = 2.57$; $\tan \delta = 0.0065$.

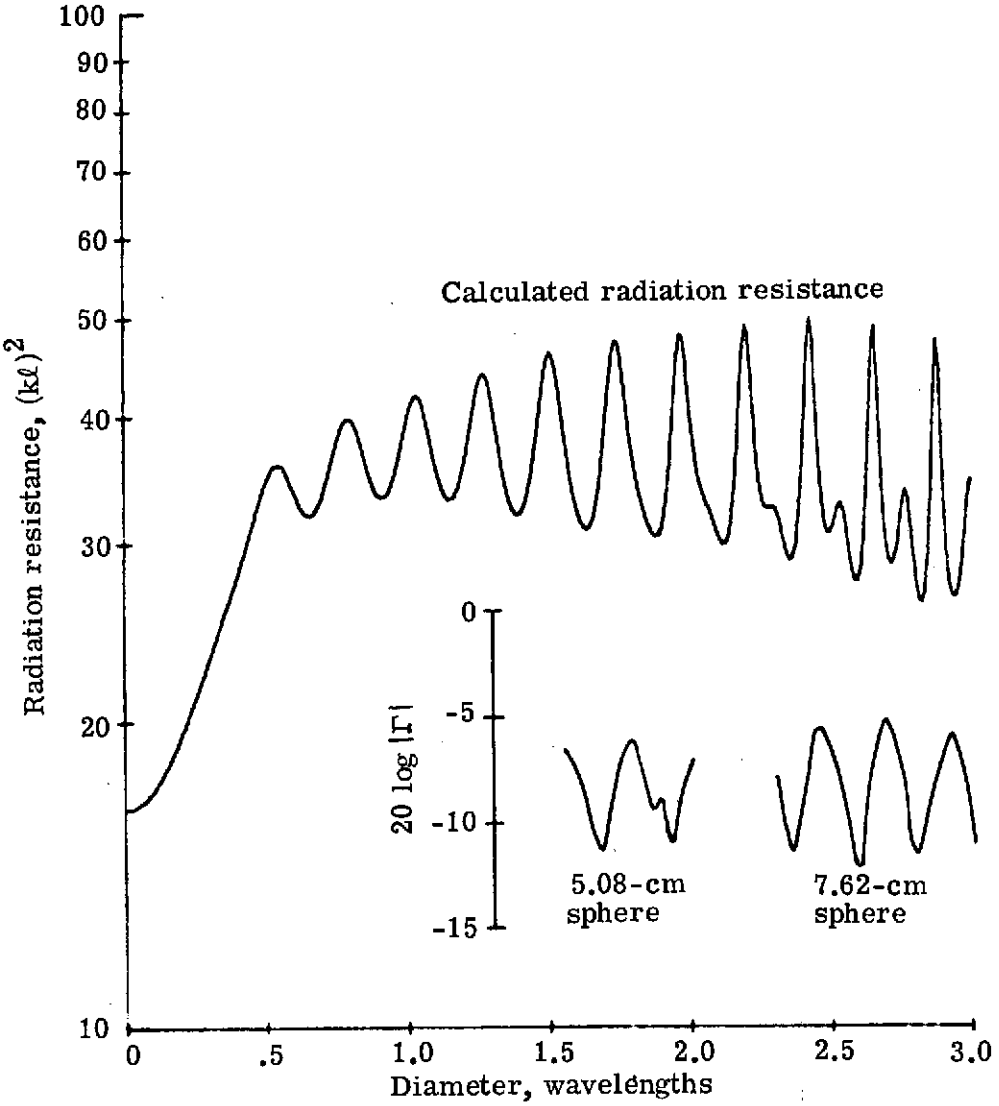

Figure 46.- Calculated radiation resistance and measured swept frequency reflection coefficients for Plexiglas spheres.

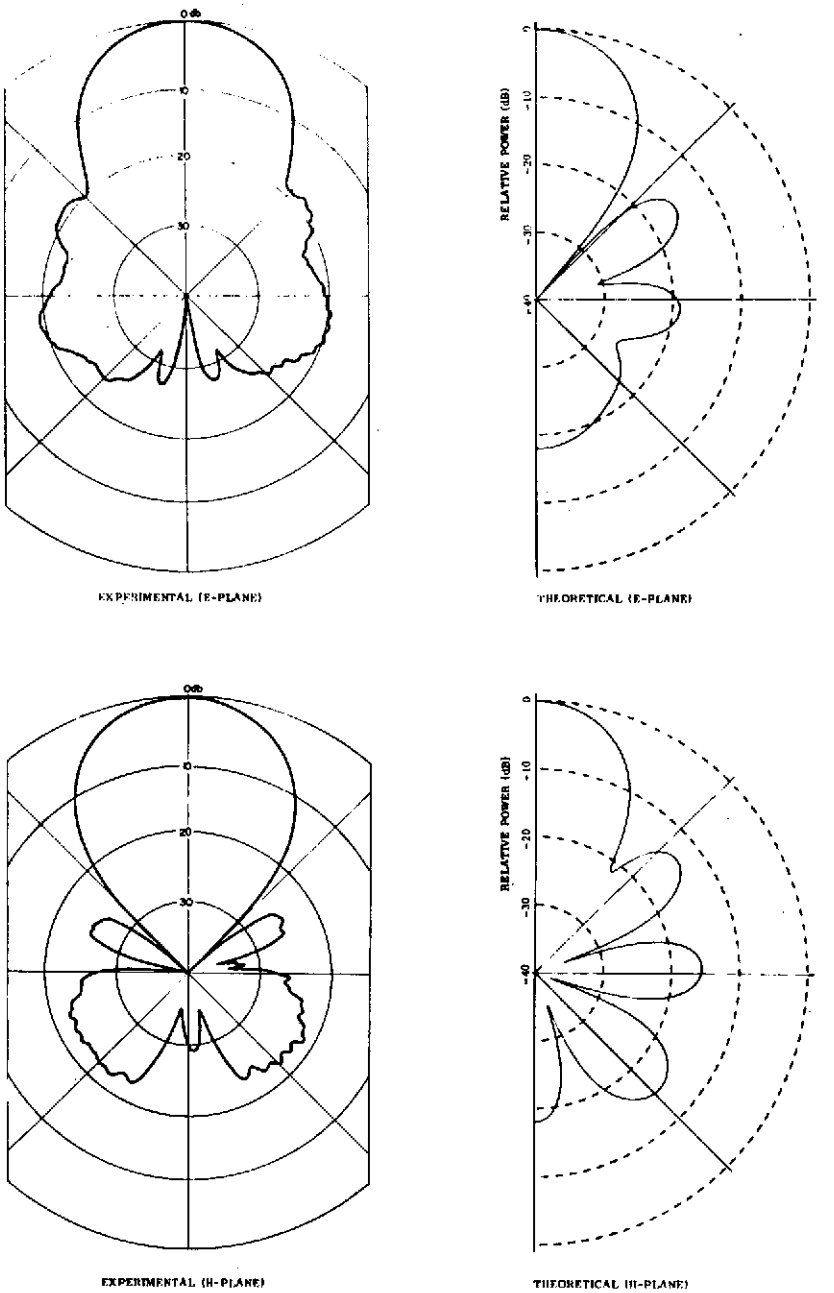

(a) D = 1.27λ.

Figure 47.- Comparison of calculated and measured radiation patterns for a circular waveguide antenna exciting a Plexiglas sphere of various diameters.

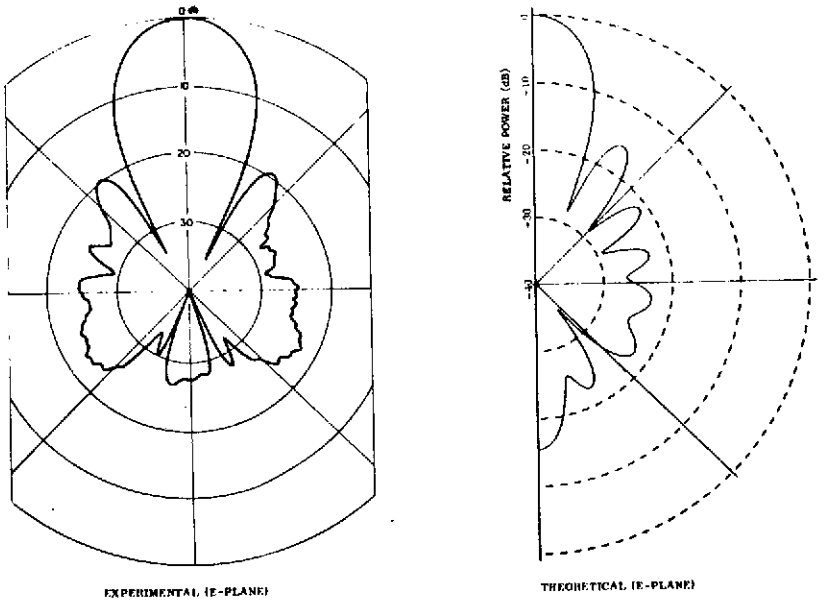

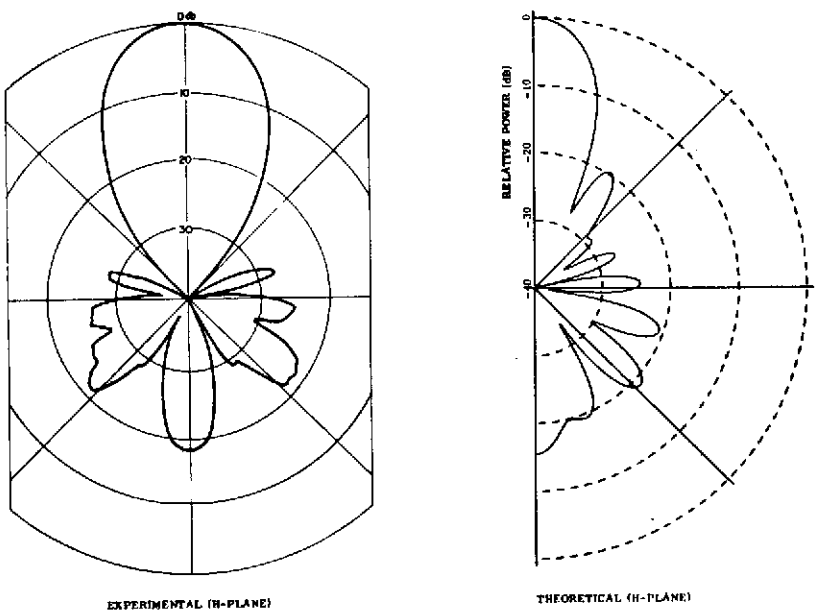

(b) $D = 2.12\lambda$.

Figure 47.- Continued.

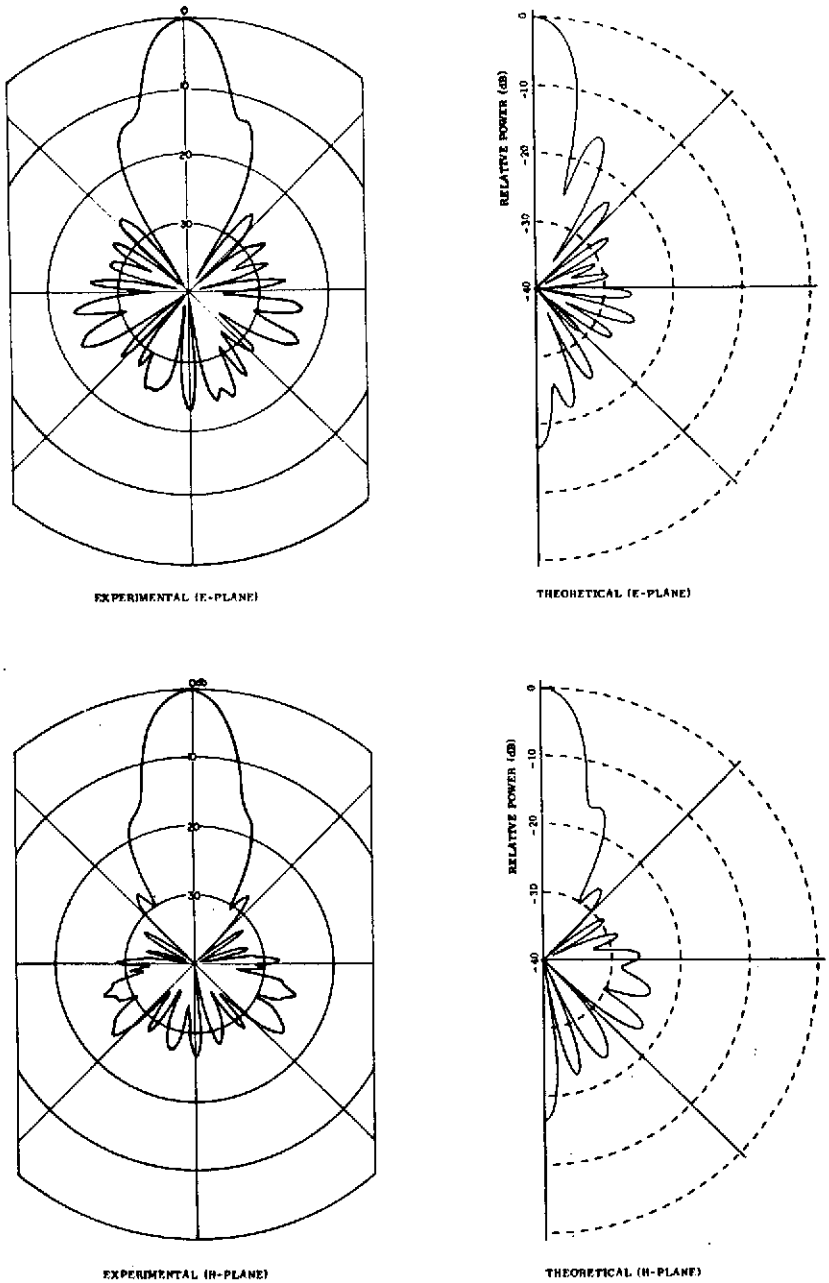

(c) D = 3.39λ.

Figure 47.- Continued.

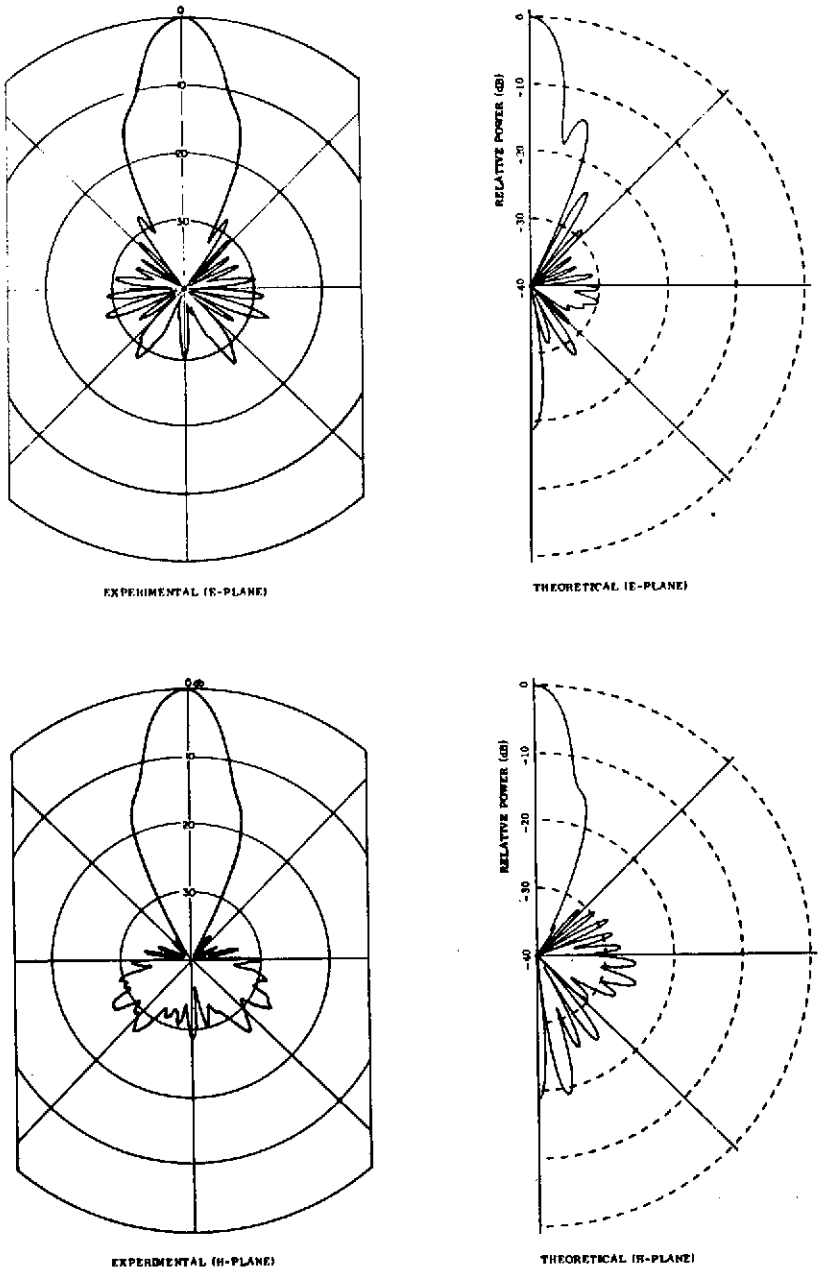

(d) D = 4.23λ.

Figure 47.- Concluded.

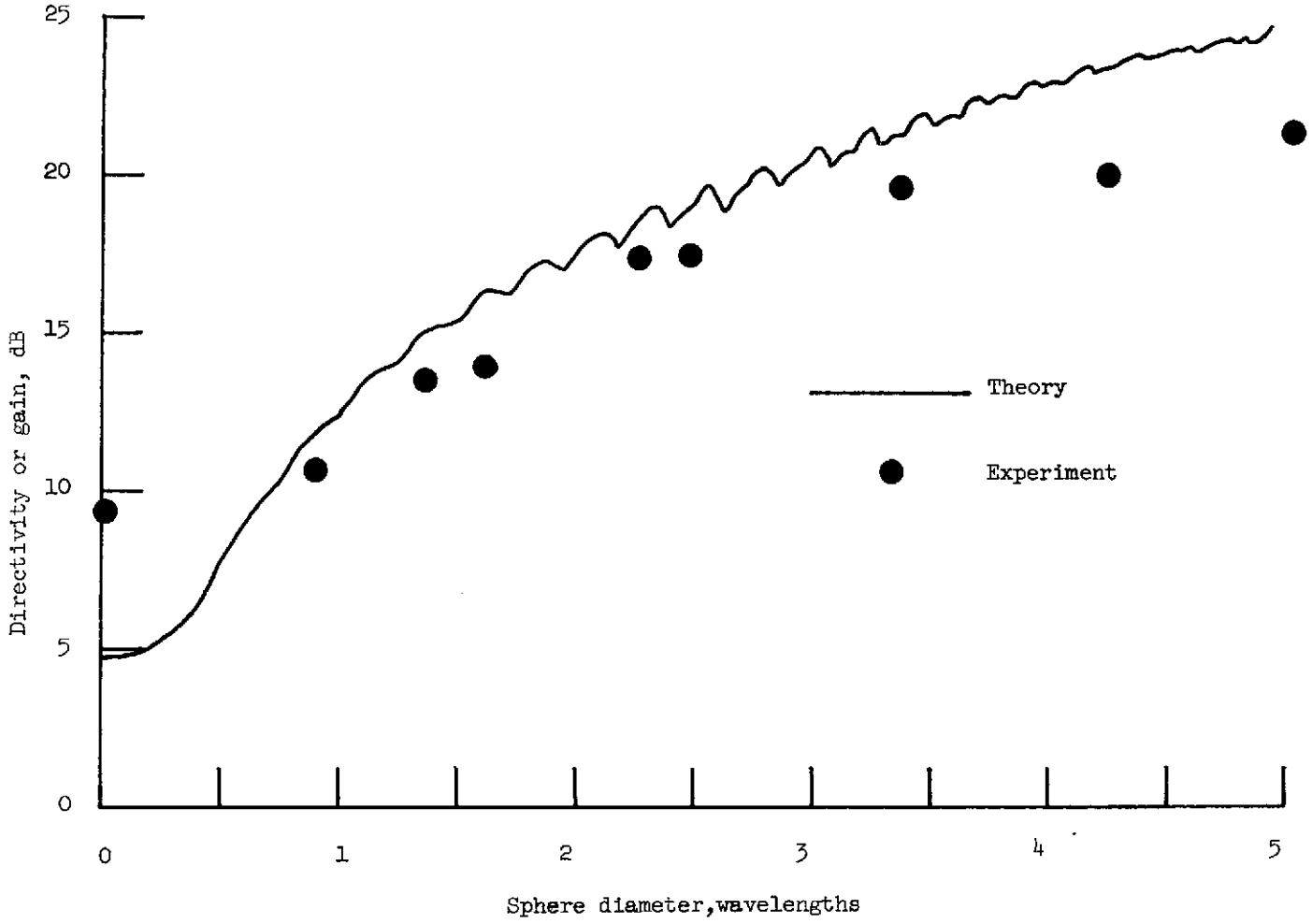

Figure 48.- Comparison of calculated directivity and measured gain of circular and square-horn waveguide antennas feeding various diameter Plexiglas spheres.

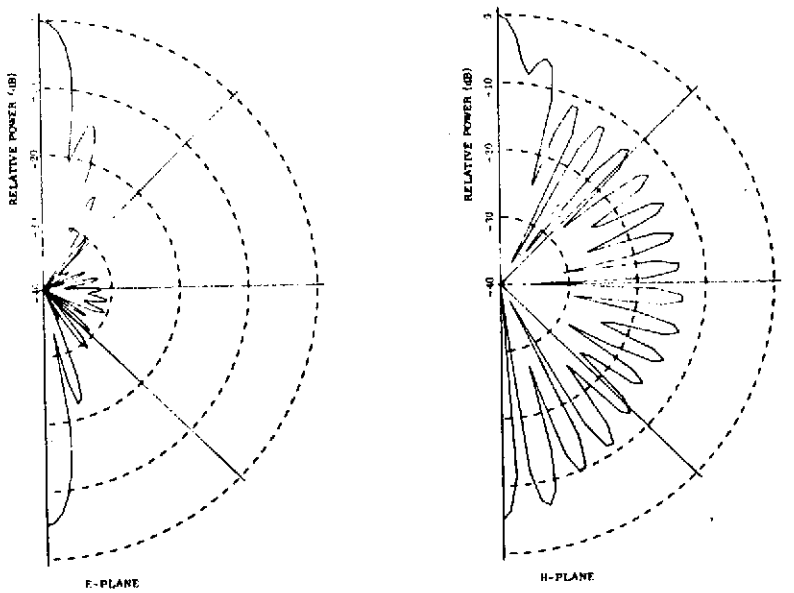

(a) $\tan \delta = 0.0$.

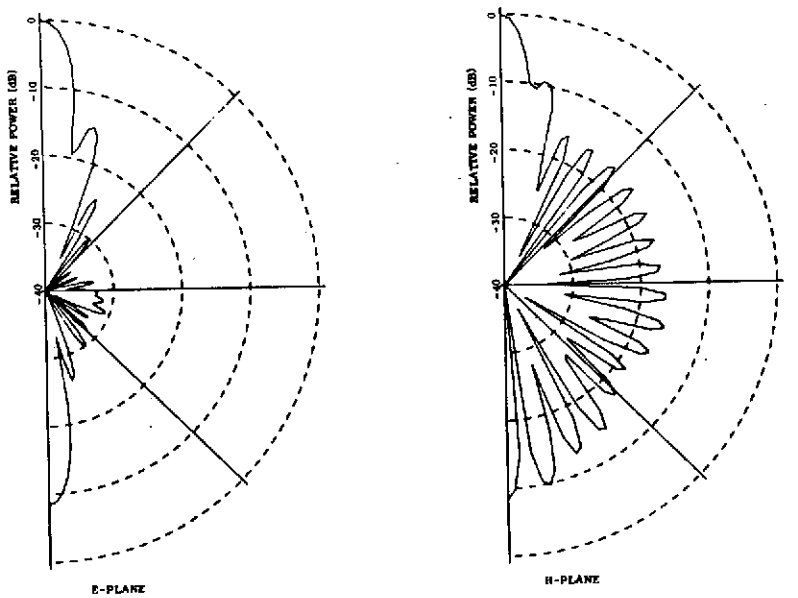

(b) $\tan \delta = 0.001$.

Figure 49.- Calculated radiation patterns for spheres with various loss tangents. $D = 4.21\lambda$; $\epsilon_r = 2.57$.

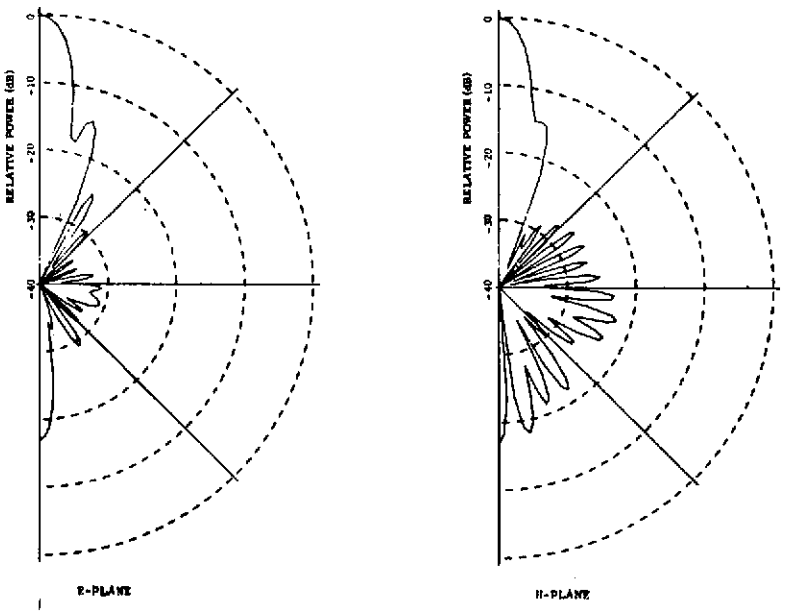

(c) $\tan \delta = 0.0065$.

Figure 49.- Concluded.

NASA-Langley, 1974 L-8920